QUANTUM LIQUIDS AND QUANTUM CRYSTALS

Thermomagnetic relaxation in two-phase solid ^{3}He–^{4}He mixtures at ultralow temperatures

N. P. Mikhin, N. F. Omelaenko, A. V. Polev, E. Ya. Rudavskii, and V. A. Shvarts

*B. Verkin Institute for Low Temperature Physics and Engineering, National Academy of Sciences of the Ukraine, 310164 Kharkov, Ukraine**

(Submitted July 10, 1998)
Fiz. Nizk. Temp. **24**, 1127–1135 (December 1998)

NMR investigations of restoration of longitudinal equilibrium magnetization in phase-separated solid ^{3}He–^{4}He mixtures are carried out in the temperature range 1–200 mK. It is found that below 100 mK, the results depend on the energy of tipping NMR pulses, while at the lowest temperatures the restoration of magnetization becomes nonmonotonic. The obtained results are explained on the basis of a proposed model in which both magnetic (spin-lattice) and thermal relaxation are assumed to take place between the Zeeman system and the lattice. © *1998 American Institute of Physics.* [S1063-777X(98)00112-1]

1. INTRODUCTION

The interest to experimental and theoretical investigations of isotopic phase separation in solid ^{3}He–^{4}He mixtures increased considerably in recent years.[1–5] This is due to the fact that the kinetics of such a phase transition is quite peculiar and is determined by quantum diffusion. Besides, phase separation results in new quantum-mechanical systems with interesting properties. For example, the initial hcp mixture can decompose under quite high pressure into a concentrated bcc phase in the form of small inclusions of almost pure ^{3}He and a dilute hcp phase, viz., the matrix in which these inclusions are distributed.

Spin-lattice relaxation in such a system was investigated by us earlier.[4] It was found that the concentrated bcc phase of the phase-separated solution as well as bulk pure ^{3}He contains a region in which the spin-lattice relaxation time T_1^c is independent of temperature and can be successfully explained by a relaxation mechanism associated with direct interaction between the Zeeman and exchange subsystems.[1)] In contrast to bulk ^{3}He, the ''exchange plateau'' region for the concentrated phase of the phase-separated mixture extended down to millikelvin temperatures.

As regards the dilute hcp phase, the spin-lattice relaxation time T_1^d in it increases with cooling due to a decrease in the ^{3}He concentration in it. Below 100 mK, the amount of ^{3}He in this phase under the experimental conditions[4] was so small that we did not expect any NMR signal from the hcp phase. However, an analysis of restoration of longitudinal magnetization of the sample revealed the presence of relaxation processes with a very large time constant along with T_1^c even at very low temperatures. This process could not be described by a single exponential, and its origin remained unclear. We can indicate at least two possible reasons behind this effect.

(1) A weakened coupling between the ''exchange bath'' and the lattice may lead under certain conditions to the second ''bottleneck'' effect; in this case the restoration of equilibrium magnetization of the sample can be described by at least two exponentials (see, for example, Ref. 6).

(2) Another possible reason can be the presence (along with the magnetic spin-lattice relaxation) of a thermal relaxation of power released under the action of rf field on the sample. The magnetization of thermally overheated sample decreases in this case, and then restored according to Curie's law, following the restoration of the equilibrium temperature of the sample. Such a situation was observed, for example, by Turrell *et al.*[7] in NMR measurements for metals.

Thus, the separation of the contributions from thermal and magnetic relaxation required special experiments in which pulses with different thermal power could be supplied to the sample. Such experiments are described in the present paper.

2. EXPERIMENTAL TECHNIQUE

A crystal with molar volume 20.3 cm^3/mole was grown in a cell (Fig. 1) by the capillary blocking technique from a gas mixture containing 3.18% ^{3}He and had a length of 20 mm and diameter 4 mm. The methods of sample preparation and cooling are described in detail in Ref. 1. The epoxy casing *1* of the cell with a capacitive pressure gage *2* was supplied with a centered silver heat exchanger *3* intended for cooling of sample *4*. Measurements were made by using a pulsed NMR spectrometer operating at a frequency of 250 kHz. A sectional cylindrical receiving coil[5] was mounted in the cell, while a saddle-shaped transmitting coil *6* was outside the cell. Thermal contact between the cell and the nuclear demagnetization stage was maintained through a silver brace *7*. The latter can be regarded as a large thermal bath with a temperature T_0 measured by the ^{3}He melting curve thermometer *8*.

 © 1998 American Institute of Physics

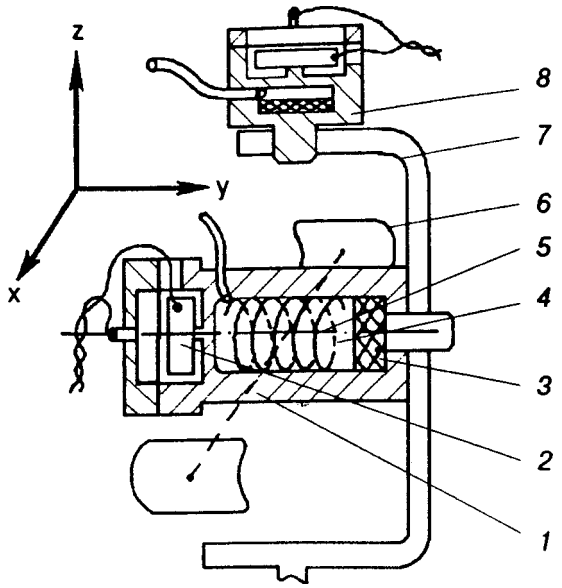

FIG. 1. Schematic diagram of measuring cell: casing (1), pressure gage (*2*), silver heat exchanger, sintered with a silver screw (*3*), sample (*4*), NMR detector coil (*5*), NMR transmitting coil (*6*), silver cold finger (*7*), and crystallization ^{3}He thermometer (*8*).

The time dependence of restoration of longitudinal magnetization of the sample was measured by the standard two-pulse technique. The parameters of pairs of pulses used in the experiments are given in Table I.

The duration t_p of pulses of the three types satisfied the ''adiabaticity condition''[8] $t_p \ll T_2^*$ since the effective spin-lattice relaxation time T_2^* in the concentrated phase of the phase-separated solution was $\sim$10 ms. Consequently, each such pulse produces the same effect on the sample from the point of view of the dynamics of the magnetization vector **M** of the sample, shifting **M** to the *xy* plane (see Fig. 1). The macroscopic magnetization of the sample vanishes in a time period of the order of $T_2^* \ll T_1$, and the coherence of processing spins as well as any information on the properties of an rf pulse is lost completely.

It should be noted that the amounts of energy Q_p liberated in the transmitting coil in each of the three cases satisfy the ratio 1:2:6 since $Q_p \sim V_p^2 t_p$, $t_p \sim 1/V_p$, and $t_{270} = 3t_{90}$. This must lead to different extents of sample overheating.

3. RESTORATION OF LONGITUDINAL MAGNETIZATION

Since both (concentrated and dilute) phases make contributions to the total magnetization $M(t)$ of the phase-separated sample, the restoration of longitudinal magnetization to its equilibrium value M_0 must obey the law

TABLE I. Parameters of NMR pulses used in experiments.

Pulse type	Sequence of pulses	Amplitude V_p, V	Pulse duration t_p, μs
1	90-t-90	25	240
2	90-t-90	50	120
3	270-t-270	50	360

$$M(t) = M_0^c\left[1 - \exp\left(-\frac{t}{T_1^c}\right)\right] + M_0^d\left[1 - \exp\left(-\frac{t}{T_1^d}\right)\right], \quad (1)$$

where T_1^c and T_1^d are the spin-lattice relaxation times in the concentrated and dilute phases respectively, and the total equilibrium magnetization of the sample is the sum of the magnetizations of the two phases:

$$M_0 = M_0^c + M_0^d. \quad (2)$$

In the experimental technique used by us, the first applied pulse rotated the longitudinal magnetization vector through 90 or 270°, and the amplitude U_0 of free induction decay (FID) after the passage of the pulse was proportional to equilibrium magnetization. In turn, the FID amplitude $U(t)$ after the passage of the second pulse was proportional to sample magnetization restored during the time t elapsed between the first and second pulses. Since $U(t)/U_0 = M(t)/M_0$, expression (1) combined with (2) can be written in the form

$$1 - \frac{U(t)}{U_0} = \frac{U_0^c}{U_0}\exp\left(-\frac{t}{T_1^c}\right) + \frac{U_0^d}{U_0}\exp\left(-\frac{t}{T_1^d}\right). \quad (3)$$

Typical dependences of the quantity $(1 - U(t)/U_0)$ on the time t elapsed between pulses of the first type (90°, 25 V) at various temperatures are shown in Fig. 2. It can be seen that the results of measurements for short t coincide for all temperatures, indicating the exponential restoration of longitudinal magnetization with the same characteristic time $\sim$0.2 s, which can be naturally attributed to spin-lattice relaxation in the concentrated phase with the characteristic time T_1^c (the first term in (3)), observed at higher temperatures also.[4]

For $t > 1$ s, the relaxation process is characterized by a relaxation time much larger than T_1^c. It was proved by us earlier[4] that at high temperatures, the relaxation process with a large time constant on the curves of restoration of longitudinal magnetization is the spin-lattice relaxation in the dilute hcp phase with the characteristic time T_1^d (the second term in (3)). It was mentioned above that the contribution of this term at temperatures below 100 mK is negligibly small since, according to the phase separation diagram,[9] the ^{3}He concentration in the dilute phase is so small that the NMR signal is difficult to single out against the background of the receiver noises under the given experimental conditions. This is visually confirmed by the results obtained at 80 and 100 mK (see Fig. 2): the relative contribution of a signal with a slow relaxation amounts to less than $\sim$0.01 of the signal from the concentrated phase. The large spread in experimental points indicates that the amplitude of the signal with the slow relaxation is comparable with the noise level under these conditions.

In this connection, we can indicate purely technological possibility of the origin of a long relaxation time. Under the conditions when the magnetization of the sample is restored almost completely, i.e., the actual signal amplitude $U(t)$ is close to the equilibrium value U_0, the measured value of the amplitude $U_i(t)$ may exceed U_0 as a result of radio noises or some other accidental reasons. In the course of computer processing, such a result can be omitted in view of indefi-

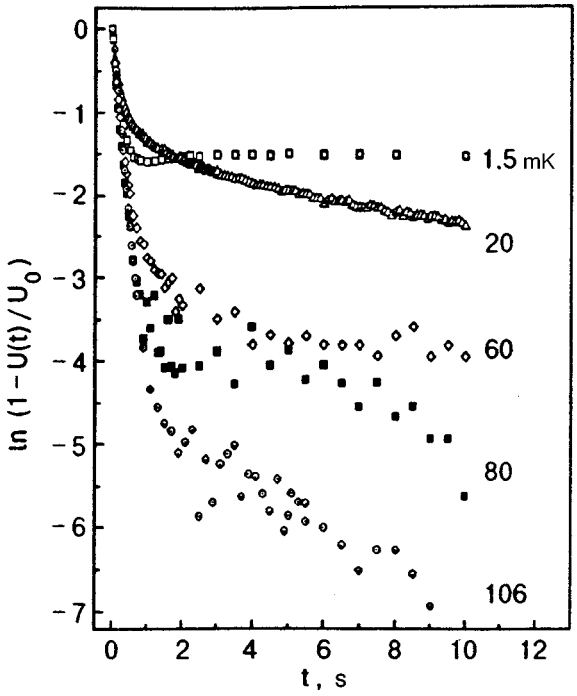

FIG. 2. Restoration of the longitudinal magnetization of a phase-separated mixture at various temperatures. Sequence of type 1 pulses was used (see Table I).

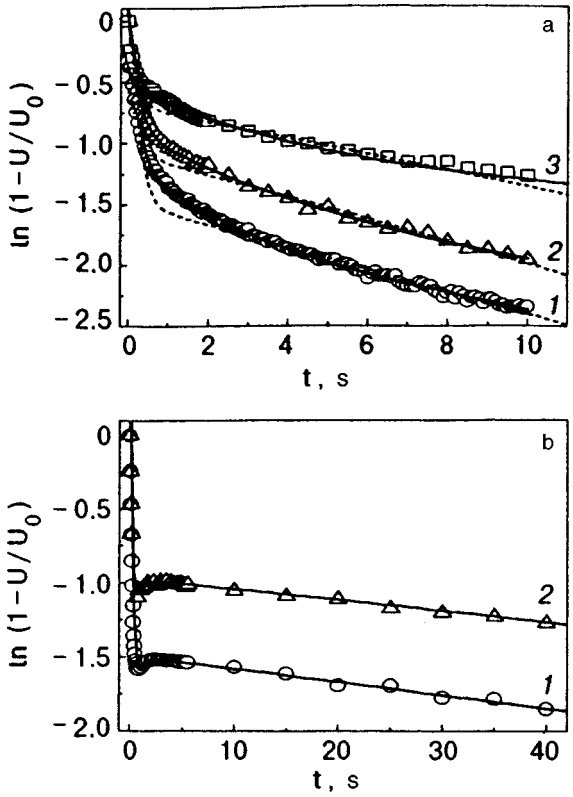

FIG. 3. Restoration of the longitudinal magnetization of a phase-separated mixture at 20 mK (a) and 1.5 mK (b). Curves *1, 2* and *3* were obtained by using pulses of types 1, 2, and 3 respectively (see Table I). Solid curves correspond to calculations based on formula (18), dashed curves are calculated by formula (7).

niteness of the expression $\ln[1-U_i(t)/U_0]$, or the argument of the logarithm should be treated as a modulus in order to avoid uncertainty. Thus, the specific contribution of the results of measurements with $U_i(t)<U_0$ increases due to omission of the results of measurements with $U_i(t)>U_0$, which leads to an effective decrease in the averaged amplitude of the measured signals, and hence to ''restoration'' of a NMR signal with a large time constant.

In order to verify the possibility of such an effect, we carried out a special computer simulation of such a situation by using a generator of random number as a noise imitator. Thus, we obtained a sequence of n values of $U_i(t)=U_i(1+\alpha)(1-\exp[-t/T_1])$ where $|\alpha|\ll 1$ is a random noise factor and T_1 the preset spin-lattice relaxation time. For $U_i(t)\approx U_i$, the behavior of the function $\ln[1-U_i(t)/U_i]$ demonstrated the emergence of a relaxation with a large time constant $\tau_R \gg T_1$, although such a relaxation was not defined by the initial formula. For this reason, we processed initial results obtained here with U_0 as a fitting parameter without taking logarithms in order to eliminate this type of effects. Semilogarithmic coordinates were chosen for better visualization of the experimental data presented below.

It can be seen that as the temperature decreases further, the ''relative contribution'' of the signal with a slow relaxation increases, and the spread in experimental data becomes smaller. Typical results of measurements obtained by using the three types of pulses (see Table I) at 20 mK are presented in Fig. 3a. In all the three cases, rapid restoration of magnetization ($T_1^c=0.2$ s) during the first 1–1.5 s changes into a slow relaxation described by at least two exponentials, and the effective contribution of the signal with slow relaxation increases with the energy of the pulses. Similar results were obtained at all temperatures of measurements (from 1.5 to 100 mK). As the temperature increases, the contribution from the signal with slow relaxation decreases as well as the dependence of this contribution from the type of measuring pulses. At ~100 mK, this contribution has the minimum value, and the effect of the energy of pulses is insignificant. At higher temperatures, this contribution cannot be distinguished against the background of the signal from the dilute phase. The results of measurements at 1.5 mK (Fig. 3b) deserve special attention. In this case, the slow relaxation region is characterized by especially long time intervals (tens of seconds), and the effect of pulse energy is the strongest. A broad but clearly manifested peak appearing near ~2 s is worth noting.

4. PHYSICAL MODELS AND EQUIVALENT DIAGRAMS OF THE SAMPLE

Second ''bottleneck'' model

In an analysis of magnetic and thermal relaxation in a complex system like solid ^{3}He–^{4}He mixtures, it is expedient to single out main subsystems coupled through certain resistances, which leads to different temperatures established in these subsystems. Radiofrequency pulses in NMR experiments affect directly the Zeeman subsystem characterized by the temperature T_Z and heat capacity

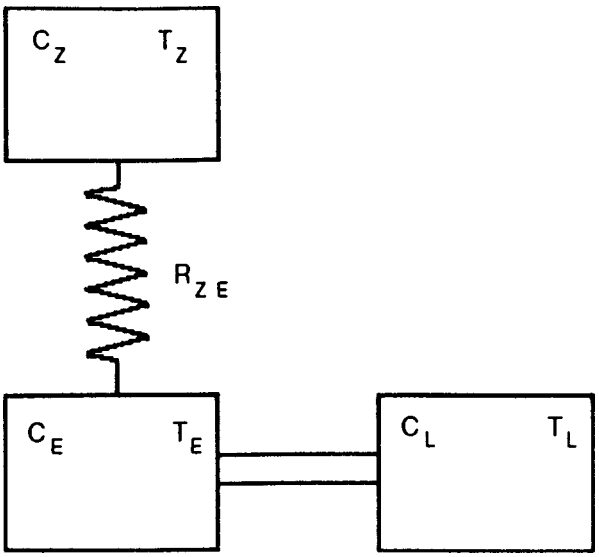

FIG. 4. Topology of magnetic energy relaxation from the Zeeman subsystem to the lattice in the concentrated phase of a phase-separated solid mixture. Indices *Z*, *E*, and *L* correspond to the Zeeman, exchange, and lattice subsystems respectively.

$$C_Z = \frac{\hbar^2 \omega^2}{4 k_B T^2} N, \tag{4}$$

where ω is the Larmor frequency, N the number of ^{3}He nuclei, and k_B Boltzmann's constant. It was proved in Ref. 4 that the energy is transferred from the Zeeman subsystem to the lattice for the concentrated phase of a phase-separated mixture in a wide temperature range through the exchange bath. In other words, energy is supplied to the exchange subsystem having the temperature T_E and the heat capacity

$$C_E = \frac{3 \hbar^2 z J^2}{8 k_B T^2} N \tag{5}$$

(J is the tunnel frequency of the ^{3}He–^{3}He exchange and z the number of nearest neighbors) and then to the phonon bath of the sample, having the heat capacity

$$C_{\mathrm{ph}} = \frac{12}{5} \pi^4 N k_B \left(\frac{T}{\Theta_D} \right)^3, \tag{6}$$

where Θ_D is the Debye temperature.

This mechanism operates as long as strong coupling exists between the exchange subsystem and the lattice, i.e., the value of T_E coincides with the lattice temperature. The topology of energy transfer for such a case is shown in Fig. 4, where the role of the ''bottleneck'' is played by the resistance between the Zeeman and the exchange subsystem. It was proved in Ref. 4 that in this case the spin-lattice relaxation time in the concentrated phase of the phase-separated mixture is independent of temperature virtually in the entire range of the existence of this phase.

As the temperature decreases, the heat capacity of the phonon subsystem of the concentrated phase decreases in accordance with formula (6) and becomes equal to the heat capacity of the exchange subsystem at a certain temperature ($\sim$100 mK), and the heat capacity of ^{3}He under further cooling is mainly determined by the heat capacity of the exchange subsystem.[10] This means that the characteristic time of relaxation between the two (exchange and phonon) subsystems can increase with C_E and become comparable with the time of relaxation between the Zeeman and exchange subsystems. In other words, the system acquires another ''bottleneck,'' and two relaxation processes with the corresponding time constants τ_{ZE} and τ_{EL} must be taken into consideration.

Such a situation in the general case was considered in Ref. 6; the solution of the problem on restoration of longitudinal magnetization $M_Z(t)$ of the Zeeman subsystem after the application of a NMR pulse can be written in the form

$$M_Z(t) = M_0 \left[1 - a \exp\left(-\frac{t}{\tau_{ZE}} \right) - b \exp\left(-\frac{t}{\tau_{EL}} \right) \right], \tag{7}$$

where the parameters a and b are functions of the heat capacity and resistance of individual subsystems; it follows from the initial conditions that $a + b = 1$.

Experimental data presented in Fig. 3a were compared with the results of calculations based on formula (7) with three fitting parameters (7) (a, τ_{ZE}, and τ_{EL}). The results are shown by dashed curves in Fig. 3a. With such an approach, good agreement with the experimental data cannot be reached by any fitting of parameters. This refers to all the available data, including the results corresponding to lower temperatures (Fig. 3b), for which the curves describing the restoration of longitudinal magnetization have peaks.

An analysis proved that the obtained experimental data (see Figs. 3a and 3b) can be described quantitatively by supplementing formula (7) with the third exponential term. However, this term could appear only in the presence of an additional thermal bath in the diagram in Fig. 4 and corresponding additional relaxation channel, which is hardly probable from the physical point of view. The strong effect of the type of NMR pulses on the relation between the parameters a and b in (7) cannot be explained either by this model.

Thermal relaxation model

Another possible reason behind anomalous restoration of longitudinal magnetization of the system at ultralow temperatures can be associated with the fact that the energy of NMR pulses supplied to the sample is not only transferred to the Zeeman bath of the ^{3}He nuclei, but also causes liberation of a certain amount of heat in the transmitting coil. In turn, this can give rise to heat flow from the casing of the experimental cell to the sample. Such an approach requires that amendments should be made in the equivalent circuit diagram of the system under investigation presented in Fig. 4. In order to analyze possible heat flows, it is convenient to single out one more subsystem associated with the casing of the cell having the temperature T_B and the heat capacity C_B. We also assume that the heat sink (nuclear stage) is an external bath and can be regarded as a perfect sink since it has an infinitely large heat capacity C_0 and temperature T_0. The corresponding equivalent circuit diagram is shown in Fig. 5.

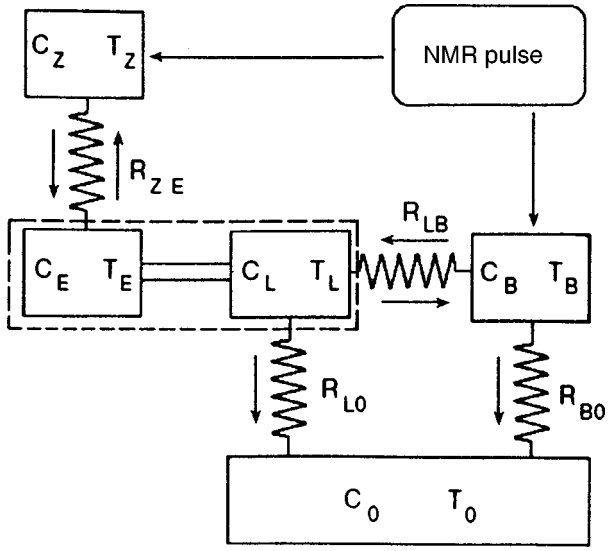

FIG. 5. Schematic diagram of thermal and magnetic relaxation in a phase-separated sample after the application of a NMR pulse. The subscripts B and 0 correspond to the casing of the cell and the nuclear stage of refrigerator. Arrows indicate the directions of energy fluxes.

Let us suppose that all the subsystems have their own equilibrium temperatures till NMR pulses are supplied. After the passage of a NMR pulse, the heat Q liberated in the casing of the cell heats it by δT as compared to the initial temperature T_{B0}: $(T_B = T_{B0} + \delta T)$. Neglecting the change in C_B upon such a small heating, we can write $Q = C_B \delta T = C_B(T_B - T_0)$. This causes the heat flux $\dot{Q} = C_B \dot{T}_B$ from the casing to the sample through the resistance R_{LB} having the meaning of the Kapitza boundary resistance as well as to the thermal bath C_0 through the corresponding Kapitza resistance R_{B0}. In this case, the equation describing the change in the temperature T_B after the passage of the pulse has the form

$$C_B \dot{T}_B = -\frac{1}{R_{LB}}(T_B - T_L) - \frac{1}{R_{B0}}(T_B - T_0). \tag{8}$$

After the passage of a NMR pulse, the lattice subsystem of the sample having the heat capacity C_L and temperature T_L receives a thermal flux from the cell casing through the resistance R_{LB} and is connected with the heat sink through the resistance R_{L0}.

It follows from Ref. 4 that the coupling between the lattice in the concentrated phase of a phase-separated mixture and the exchange bath having the heat capacity C_E is so strong that the exchange bath temperature T_E can be regarded as approximately equal to T_L; at any rate, the characteristic time of establishing equilibrium is much shorter than $T_1^c \approx 0.2$ s. In order to simplify the model, we assume the exchange subsystem and the lattice to be a single system having the same temperature $T_{EL} = T_E = T_L$ and the total heat capacity $C_{EL} = C_E = C_L$. Then the heat balance equation written for the EL system in analogy with (8) has the form

$$C_{EL}\dot{T}_{EL} = \frac{1}{R_{BL}}(T_B - T_{EL}) - \frac{1}{R_{L0}}(\dot{T}_{EL} - T_0) - \frac{1}{R_{ZE}}(T_{EL} - T_Z). \tag{9}$$

This equation (9) also takes into account the coupling between the exchange–lattice system and the Zeeman subsystem having the temperature T_Z through the thermal resistance R_{ZE}.

A similar equation for the Zeeman subsystem has the form

$$C_Z \dot{T}_Z = -\frac{1}{R_{ZE}}(T_Z - T_{EL}). \tag{10}$$

Equations (8)–(10) form a system of three linear nonhomogeneous first-order differential equations in the variables

TABLE II. Parameters obtained by fitting Eq. (18) to experimental results by the least square method; $\tau_K = R_K C_S$ is the rated thermal relaxation time (see text).

T_0, mK	Pulse type	$\Delta T/T_0$	$\Delta T_N/\Delta T_1$	B	τ_1, s	τ_2, s	τ_3, s	τ_K, s
1.5	1	0.29	1	0.08	92	0.4	0.46	-
1.5	2	0.57	1.97	0.08	90.4	0.42	0.45	-
7	1	0.26	1	2.11	70.5	5.7	<0.1	-
7	2	0.53	2.04	2.0	70	4.6	<0.1	-
7	3	1.5	5.77	1.67	62.2	7.2	<0.1	-
20	1	0.23	1	1.25	11.4	1.28	<0.1	62
20	2	0.44	1.91	1.16	11.6	1.25	<0.1	-
20	3	1.3	5.65	0.86	16.0	1.4	<0.1	-
60	1	0.034	1	1.4	11.7	2.4	<0.1	5.8
60	2	0.07	2.06	1.9	10	2	<0.1	-
60	3	0.2	5.88	1.7	11.5	0.6	<0.1	-
80	1	0.03	1	0.56	6.6	0.5	<0.1	4.5
80	2	0.058	1.93	1.35	7.58	0.04	<0.1	-
80	3	0.17	5.67	1.35	7.6	0.01	<0.1	-
106	1	0.007	1	1.0	6.0	1.5	<0.1	6.4
106	2	0.009	1.29	1.0	5.0	2.0	<0.1	-
106	3	0.015	2.14	1.0	5.0	2.0	<0.1	-

T_Z, T_{EL}, and T_B. Eliminating the remaining variables, we obtain a third-order differential equation in T_i:

$$a\dddot{T}_i + b\ddot{T}_i + c\dot{T}_i + (T_i - T_0)d = 0, \tag{11}$$

where the subscript $i = B, EL, Z,$ and the coefficients a, b, c, and d appearing in (11) can be expressed in terms of the heat capacities and thermal resistances of the subsystems. The general solution of Eqs. (11) has the form

$$T_i = T_0 + A_i \exp\left(-\frac{t}{\tau_1}\right) + B_i \exp\left(-\frac{t}{\tau_2}\right) + C_i \exp\left(-\frac{t}{\tau_3}\right), \tag{12}$$

where τ_1, τ_2, τ_3 are the characteristic relaxation times. The initial conditions for solutions have the form

$$A_B + B_B + C_B = \delta T, \tag{13}$$

$$A_{EL} + B_{EL} + C_{EL} = 0, \tag{14}$$

$$A_Z + B_Z + C_Z = 0 \tag{15}$$

and indicate that at the initial instant only the casing of the cell is overheated by δT, while the lattice as well as the exchange and the Zeeman subsystems have the equilibrium temperature T_0. It should be noted that Eqs. (14) and (15) imply that A_{EL}, B_{EL}, and C_{EL} as well as A_Z, B_Z, and C_Z cannot have the same sign. Since we can prove that the coefficients in (12) are proportional to δT, expression (12) for the temperature of the Zeeman subsystem with (15) can be written in the form

$$T_Z = T_0\left\{1 + \frac{\delta T}{T_0} A\left[\exp\left(-\frac{1}{\tau_1}\right) + B\exp\left(-\frac{t}{\tau_2}\right) - (1+B)\exp\left(-\frac{t}{\tau_3}\right)\right]\right\}, \tag{16}$$

i.e., is a function with a peak describing the overheating of the Zeeman system at a rate $\sim 1/\tau_3$ by a thermal pulse from the transmitting coil and subsequent thermal relaxation with two characteristic times τ_1 and τ_2.

Let us suppose that the amplitude of the NMR signal from the overheated ($T_Z > T_0$) Zeeman system is $U^*(t)$, while the amplitude of the signal from the non-overheated ($T_Z = T_0$) system is $U(t) = U_0[1 - \exp(-t/T_1^c)]$. In this case, in accordance with the Curie law (we assume that the Zeeman system is a paramagnet in the entire temperature range under investigation), we can write

$$\frac{U^*(t)}{U_0[1 - \exp(-t/T_1^c)]} = \frac{T_0}{T_Z} \tag{17}$$

or, taking into account (15) and (16),

$$U^* = \frac{U_0[1 - \exp(-t/T_1^c)]}{1 + \Delta T/T_0[\exp(-t/\tau_1) + B\exp(-t/\tau_2) - (1+B)\exp(-t/\tau_3)]}, \tag{18}$$

where $\Delta T/T_0 = A\,\delta T/T_0$ has the meaning of relative overheating of the Zeeman subsystem. Equation (18) describing experimental data has five free parameters (τ_1, τ_2, τ_3, $\Delta T/T_0$, and B). Thus, solid curves in Figs. 3a and 3b are the result of fitting of formula (18) to experimental data by the least square method. In can be seen that the results of calculations are in good agreement with the experimental data.

Figure 3b shows that dependence (18) also successfully describes the peaks appearing at the lowest temperature, and the given model explains the emergence of these peaks by the arrival of the thermal front from transmitting coils. It is interesting to note that qualitatively similar results were obtained by Turrell *et al.*[7] in NMR experiments for metals at ultralow temperatures.

The results of processing of all the experimental data by using formula (18) are presented in Table II. It should be noted above all that the ratio of the parameters $\Delta T/T_0$ obtained by using the three types of pulses mentioned above at each temperature are close to 1:2:6, which coincides with the ratio of the energies liberated by a pulse of each type. This is a direct evidence that the ratio of overheating of the Zeeman system taking into account the assumptions made in the construction of the model is also the same. This also means that the thermal energy liberated in the transmitting coils is responsible for the observed effects. The only exception are the results obtained at 106 mK, when overheating is so small that its effect can hardly be distinguished against the background of noises.

As regards the characteristic relaxation times τ_1, τ_2, and τ_3, their dependence on the type of applied pulses is weak, confirming our initial assumption on the negligibly small change in all heat capacities and thermal resistances under overheating. It should be notes that the complex dependence of the fitting parameters appearing in formula (18) on heat capacities and thermal resistances complicates the derivation of explicit expressions for these quantities. Nevertheless, the increase in the parameter $\Delta T/T_0$ during cooling can be qualitatively associated with a decrease in the values of C_B and C_L, while the increase in τ_1 and τ_3 under these conditions is clearly caused by an increase in thermal resistances appearing in the model (Fig. 5), whose components are the conventional thermal conductivity as well as ''Kapitza jumps'' at the interfaces between the media. The real cell containing phase-separated solid mixture is a system with distributed parameters, while the schematic diagram in Fig. 5 illustrates a system with concentrated parameters. This difference also complicates the comparison of the obtained results with the available data from the literature concerning

heat capacity and thermal conductivity. However, if we assume that the slow relaxation time is mainly determined by the heat capacity C_S of a solid helium sample with the Kapitza thermal resistance R_K at the interface between solid helium and the centered heat exchanger *3* (see Fig. 1), we can estimate the expected values of the relaxation time associated with Kapitza resistance,[11] i.e., $\tau_K = R_K C_S$ using the values of $R_K(T) = 3 \cdot T^{-3}$ (K/W) measured earlier in the same cell[11] and extrapolating the data on heat capacity of the phase-separated solid mixtures at temperatures 20–106 mK under the given experimental conditions.[12] The values of τ_K obtained in this way for some temperatures are presented in Table II. As expected, the values of τ_K coincide with the maximum characteristic time τ_1 only in the order of magnitude, although a certain correlation can be noted in the temperature dependences of τ_K and τ_1.

Thus, NMR experiments in phase-separated solid ^{3}He–^{4}He mixtures proved that the energy exchange between the Zeeman subsystem and the lattice at ultralow temperatures can occur not only through conventional spin-lattice relaxation, but also through thermal relaxation in the case when one of the subsystems is overheated by NMR pulses. This leads to anomalous restoration of equilibrium longitudinal magnetization which can be nonmonotonic.

The authors are grateful to V. N. Grigor'ev, T. N. Antsygina and K. A. Chishko for fruitful discussions.

*E-mail: mikhin@ilt.kharkov.ua

[1)]Following the traditionally adopted terminology (see, for example, the review by R. A. Guyer, R. C. Richardson, L. I. Zane, Rev. Mod. Phys. **43**, 532 (1971) and the monograph by A. Abragam and M. Goldman, *Nuclear Magnetism: Order and Disorder*, Clarendon Press, Oxford (1984)), we assume that the Zeeman and exchange subsystems (baths) are the contributions of the Zeeman and exchange spin interactions respectively to heat capacity, and the coupling between the baths is the energy exchange between them.

[1] V. A. Shvarts, N. P. Mikhin, E. Ya. Rudavskii *et al.*, Fiz. Nizk. Temp. **21**, 717 (1995) [Low Temp. Phys. **21**, 556 (1995)].
[2] T. N. Antsygina, V. A. Slyusarev, and K. A. Chishko, Fiz. Tverd. Tela (St. Petersburg) **38**, 1906 (1996) [Phys. Solid State **38**, 1054 (1996)].
[3] R. Schrenk, R. Konig, and F. Pobell, Phys. Rev. Lett. **76**, 2945 (1996).
[4] N. P. Mikhin, A. V. Polev, E. Ya. Rudavskii, and V. A. Shvarts, Fiz. Nizk. Temp. **23**, 607 (1997) [Low Temp. Phys. **23**, 455 (1997)].
[5] R. R. Haley and E. D. Adams, Fiz. Nizk. Temp. **23**, 615 (1997) [Low Temp. Phys. **23**, 462 (1997)].
[6] A. Abragam and B. Bleaney, *Electron Paramagnetic Resonance of Transition Ions*, Clarendon Press, Oxford (UK) (1970).
[7] B. G. Turrell, G. Eska, N. Masuhara, and E. Schuberth, J. Low Temp. Phys. **70**, 151 (1988).
[8] E. L. Hahn, Phys. Rev. **80**, 580 (1950).
[9] V. A. Shvarts, N. P. Mikhin, E. Ya. Rudavskii *et al.*, Fiz. Nizk. Temp. **20**, 645 (1994) [Low Temp. Phys. **20**, 505 (1994)].
[10] D. S. Greywall, in *Quantum Fluids and Solids* (ed. by S. B. Trickey, E. D. Adams, and J. W. Dufty), Plenum Press, New York-London (1977).
[11] V. A. Shvarts, Ph.D. thesis, B. Verkin Inst. for Low-Temp. Phys. and Engineering, Kharkov (1995).
[12] R. Schrenk, O. Friz, Y. Fujii *et al.*, J. Low Temp. Phys. **84**, 133 (1991).

Translated by R. S. Wadhwa

LOW-TEMPERATURE MAGNETISM

Metastable states, spin–reorientation transitions, and domain structures in planar hexagonal antiferromagnets

A. N. Bogdanov and I. E. Dragunov

*A. Galkin Physicotechnical Institute, National Academy of Sciences of the Ukraine, 340114 Donetsk, Ukraine**

(Submitted July 13, 1998)
Fiz. Nizk. Temp. **24**, 1136–1143 (December 1998)

Equilibrium states are calculated for a planar hexagonal antiferromagnet in a magnetic field oriented in the basal plane. As the field is rotated in the basal plane, a number of first-order phase transitions accompanied by magnetization jumps are observed in the range of metastable states in the system. The range and equilibrium parameters of the thermodynamically stable domain structure formed in the vicinity of such transitions are determined. Magnetization curves in $RbMnCl_3$ are analyzed. © *1998 American Institute of Physics.* [S1063-777X(98)00212-6]

INTRODUCTION

Hexagonal antiferromagnets, including halides of the type ABX_3 as well as several other magnets,[1–3] form a fairly large group of compounds among magnetically ordered crystals. The magnetic ordering in such crystals is of quasi-one-dimensional type: antiferromagnetic ordering along the hexagonal axis is several orders of magnitude higher than the exchange interactions in the basal plane. The comparative weakness of relativistic interactions in chains and exchange and relativistic interactions between chains results in a diversity of magnetic structures in this type of magnets. For example, ferromagnetic exchange interaction between chains dominates in the plane antiferromagnet $CsNiF_3$, and hence a collinear plane structure is realized in this case. The antiferromagnetic exchange interaction taking place in the basal plane of $CsNiCl_3$ leads to the formation of trigonal antiferromagnetic lattices. In turn, structures with a uniaxial (e.g., in $CsNiBr_3$, $CsMnI_3$, $CsVCl_3$, $KNiCl_3$) or planar type anisotropy ($CsMnBr_3$, $RbFeBr_3$, etc.)[4] are realized in trigonal lattices. Finally, modulated magnetic structures are observed in $CsCuCl_3$ and $RbMnBr_3$.[5]

A magnetic field applied to the basal plane causes various spin-reorientational phase transitions in the systems under consideration.[2–4,6,7] In particular, such transitions have been studied intensively in recent years in frustrated trigonal structures (see the literature cited in Ref. 6). Numerous experimental studies demonstrate the dominating role of hexagonal anisotropy in the formation of equilibrium states in the magnetic systems being considered here. In this connection, it is especially important to study collinear plane antiferromagnets. Materials of this type, whose static as well as rf properties have been studied most intensively include $CsNiF_3$ (Néel temperature $T_N = 2.65$ K), $CsMnF_3$ ($T_N = 53.5$ K) and $RbMnCl_3$ ($T_N = 94.6$ K).[2,3,7,8] On account of a relatively weak hexagonal anisotropy, even weak applied fields cause a significant rearrangement of the magnetic structure and induce a number of spin-reorientational phase transitions.[2,3] However, the available theoretical results on the equilibrium structures of hexagonal plane antiferromagnets in a magnetic field applied to the basal plane pertain only to selected symmetry directions.[8,9]

In this work, we study the effect of hexagonal anisotropy and magnetic field on equilibrium spin configurations of plane systems. It is shown that in a certain range of the planar magnetic field **H**, a magnet undergoes several first-order phase transitions accompanied by magnetization jumps. Phase diagrams are constructed and phase transition curves calculated, while the equilibrium states in competing phases are also calculated.

We also calculated the equilibrium parameters and the boundaries of thermodynamically stable domain structure formed in the vicinity of the orientational phase transitions. The obtained results are used for analyzing the experimental results of the static magnetic properties of $RbMnCl_3$.[7,8]

1. ENERGY AND EQUILIBRIUM STATES

In the framework of the phenomenological theory, the standard expression for the free energy density of a hexagonal two-sublattice antiferromagnet without Dzyaloshinskii interaction and placed in an external magnetic field has the form

$$E = \lambda \mathbf{M}_1 \cdot \mathbf{M}_2 - \mathbf{H} \cdot (\mathbf{M}_1 + \mathbf{M}_2) + E_A , \qquad (1)$$

where $\mathbf{M}_i$ is the magnetization of the ith sublattice, λ the constant of exchange interaction between sublattices, and E_A the magnetic anisotropy energy density (for the magnets under consideration, $E_A \ll \lambda M_0^2$, i.e the anisotropy is weak). We shall also assume that the temperature is much lower than the ordering temperature so that paraprocesses can be

 © 1998 American Institute of Physics

disregarded, i.e., the condition $|\mathbf{M}_i| = M_0$ is preserved in the magnetic field, M_0 being the saturation magnetization.

In the analysis of the energy (1), it is convenient to go over to the total magnetization vector **m** and the antiferromagnetism vector **l**:

$$\mathbf{M}_{1,2} = M_0(\mathbf{m} \pm \mathbf{l}).$$

Since $|\mathbf{M}_1| = |\mathbf{M}_2| = M_0$, we have $\mathbf{m}\cdot\mathbf{l} = 0$, $\mathbf{m}^2 + \mathbf{l}^2 = 1$.

In the region of weak fields for which $H \ll \lambda M_0$, the total magnetization $|\mathbf{m}| \ll 1$. Hence terms with components **m** can be disregarded in the expression for the anisotropy energy density E_A.

The potential of the investigated system (1) in components **m** and **l** can be written in the form

$$E = 2M_0(\lambda M_0 \mathbf{m}^2 - \mathbf{H}\cdot\mathbf{m}) + E_A. \tag{2}$$

The anisotropy energy of a hexagonal crystal can be written by taking sixth-order terms into consideration:

$$E_A = K_1 l_z^2 + K_2(l_x^2 + l_y^2)^2 + \frac{K_3}{2}[(l_x + il_y)^6 + (l_x - il_y)^6]. \tag{3}$$

If the second-order anisotropy coefficient $K_1 > 0$, the antiferromagnet is an easy-plane antiferromagnet with *xy* as the easy plane. The last term in Eq. (3) describes the anisotropy of magnetic properties in the basal plane of the crystal.

Minimizing the potential (2) in **m** under the condition $\mathbf{m}\cdot\mathbf{l} = 0$, we arrive at the following expression for equilibrium magnetization:

$$\mathbf{m} = \frac{1}{2\lambda M_0^2}[\mathbf{H} - (\mathbf{H}\cdot\boldsymbol{\alpha})\cdot\boldsymbol{\alpha}]. \tag{4}$$

Here we have introduced the unit vector $\boldsymbol{\alpha} = \mathbf{l}/|\mathbf{l}|$, which is collinear with **l**.

Substitution of (4) into (2) gives

$$E = -\frac{1}{2\lambda}[\mathbf{H}^2 - (\mathbf{H}\cdot\boldsymbol{\alpha})^2] + E_A. \tag{5}$$

In a magnetic field **H** lying in the basal plane, the antiferromagnetism vector in the equilibrium state also lies in the same plane. Introducing φ between $\boldsymbol{\alpha}$ and the *x*-axis, and the angle ψ between **H** and the *x*-axis, we can present the energy density (5) in the form

$$\Phi = \frac{E}{\lambda|B|M_0^2} = h^2\cos(2\varphi - 2\psi) + \frac{\mathrm{sgn}(B)}{6}\cos 6\varphi,$$

$$h = \frac{H}{2\lambda\sqrt{|B|}M_0}, \quad B = \frac{6K_3}{\lambda M_0^2}. \tag{6}$$

The equilibrium states of the system are defined as functions of the angle φ by minimizing the potential (6). For any values of the field, the states with φ and $\varphi + \pi$ have the same values of the energy (6) corresponding to them. This is due to the energy equivalence of magnetic configurations with antiparallel antiferromagnetism vectors **l**.

The hexagonal anisotropy (3) defines in the basal plane the direction of preferred orientation of the antiferromagnetism vector (easy axes):

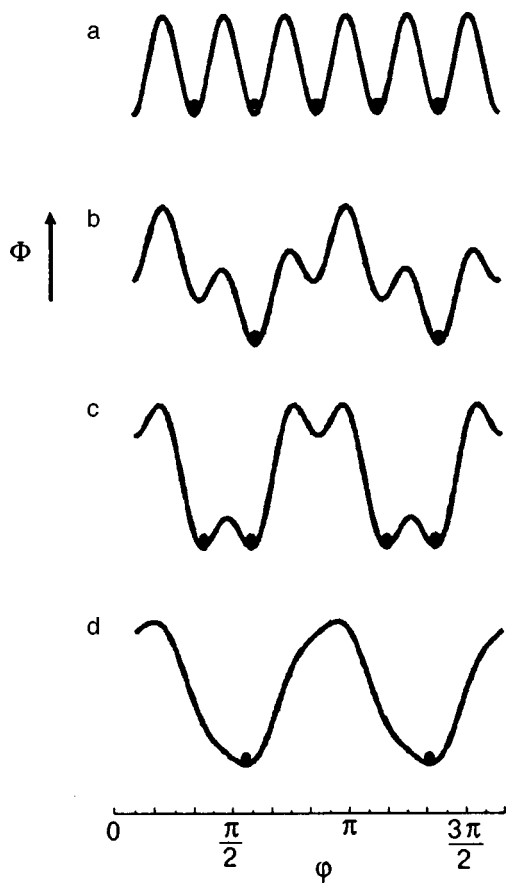

FIG. 1. Functional dependence of energy $\Phi(\varphi)$ (6) for some values of magnetic field: $h = 0$ (a), in the region of metastable states (b), in the field of PT1 (c), and outside the region of metastable states (d).

$$\varphi = \pi/6 + \pi k/3 (B > 0), \quad \varphi = \pi k/3 (B < 0). \tag{7}$$

In the field $h = 0$, the minimum of the potential (6) corresponds to collinear phases ($\mathbf{m} = 0$) with φ from (7) (see Fig. 1a). On the other hand, the application of a very strong magnetic field in the basal plane suppresses the effect of the anisotropy (3). Thus, spin configurations characteristic of an isotropic antiferromagnet, i.e., states in which the antiferromagnetism vector **l** is perpendicular to the applied field, must be realized in high magnetic fields. Since degenerate states (7) cannot vanish instantaneously, we come to the conclusion that a region of metastable states must exist on the $h_x h_y$-phase diagram of the magnet under consideration. The boundary of this region is determined by the standard technique from the system of equations $d\Phi/d\varphi = 0$, $d^2\Phi/d\varphi^2 = 0$. Eliminating φ from this system of equations, we arrive at the following expression for the lability curve:

$$[h^6\cos 6\psi + \mathrm{sgn}(B)9(4h^4 - 3)/16] \times \sqrt{h^4 - 1/4} + h^6 \sin 6\psi\sqrt{9/4 - h^4} = 0. \tag{8}$$

Depending on the sign of *B*, the closed curves (8) are rotated relative to one another through an angle $\pi/6$ (see Fig. 2). The lability fields attain their maximum values at the sharp tips of the curves (8) ($h_1 = \sqrt{3/2}$, the angles ψ are de-

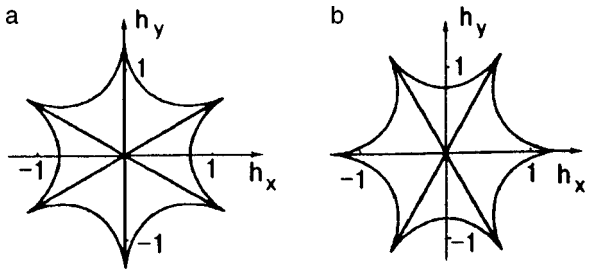

FIG. 2. Phase diagrams $h_x h_y$ of a planar hexagonal antiferromagnet for $B>0$ (a) and $B<0$ (b).

fined by formulas (7)), and the minimum field values $h_2=\sqrt{1/2}$ are attained along the directions rotated through an angle of 30° to (7).

In order to study the evolution of the system, we consider the variation of the potential (6) upon an increase in the magnetic field for different fixed values of the angle ψ. The application of a magnetic field to the basal plane violates the collinearity of magnetic structures and removes the degeneracy: the spin configurations in which the magnetization vector forms the smallest angle with the applied field vector define the absolute energy minimum, while the remaining solutions of (7) are transformed into local minima (metastable states) (Fig. 1b). Finally, local minima merge with local maxima and vanish from the lability curve (8). Outside the range of metastable states, the energy (6) has the form shown in Fig. 1d. The situation in which the magnetic field is directed parallel to one of the antiferromagnetism vectors corresponding to the ground state in zero field (see (7)) deserves special attention. On the $h_x h_y$ phase diagrams (Fig. 2), these symmetry directions have the corresponding segments of straight lines

$$|h|\leqslant h_1, \quad \psi=\pi/6+\pi k/3 (B>0),$$
$$|h|\leqslant h_1, \quad \psi=\pi k/3 (B<0), \tag{9}$$

connecting the origin of coordinates to the sharp tips of the lability curves (8). The degeneracy of the ground states of the system is partially preserved upon a variation of the magnetic field along the straight lines (9) (Fig. 1c). As the field increases, the potential barrier separating the ground states of the system decreases, and both minima merge at the sharp tips into a single extremum corresponding to spin configurations with the antiferromagnetism vector **l** perpendicular to the magnetic field. Upon a further increase in the field along the direction (9), i.e., for $h>h_1$, the vector **l** remains perpendicular to the field, and the evolution of the system takes place as a result of the rotation of sublattice magnetizations towards the direction of the field.

Let us discuss in detail the degeneracy of states on curves (9). An analysis shows that these states have opposite values of the magnetization components perpendicular to the applied field. Thus, the departure of the magnetic field from the directions defined by (9) leads to a violation of the phase equilibrium states shown in Fig. 1c. The energy of one of the states decreases while that of the other increases. Such a situation is typical of field-induced first-order phase transitions (PT1). In other words, it can be stated that curves (9)

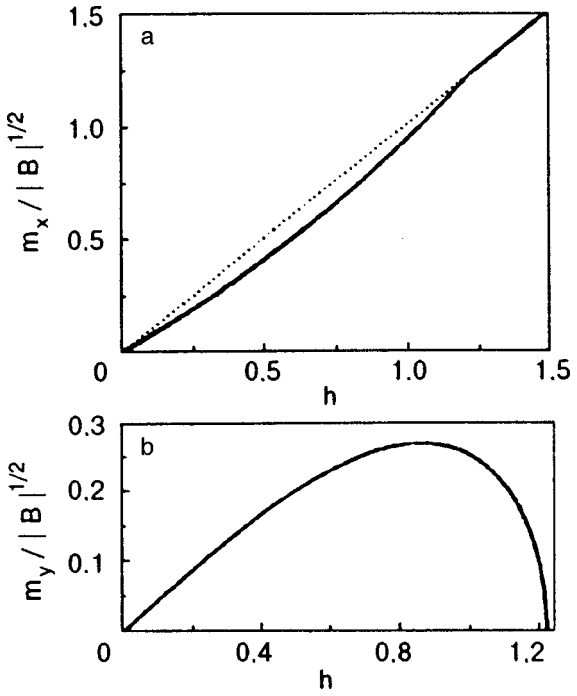

FIG. 3. Components of equilibrium magnetization at the PT1 curve $|h|\leqslant h_1$, $\psi=0$ ($B<0$): m_x (a) and m_y (b).

are PT1 curves induced by the components of the magnetic field perpendicular to the directions (9). For example, phases with

$$\varphi_1=\frac{1}{4}\left[2\pi-\arccos\left(h^2-\frac{1}{2}\right)\right],$$
$$\varphi_2=\frac{1}{4}\left[2\pi+\arccos\left(h^2-\frac{1}{2}\right)\right], \tag{10}$$

are realized on the curve $|h|\leqslant h_1$, $\psi=0$ (9) for $B<0$.

Let us determine the value of magnetization along this curve. For the magnetization components, we obtain from (4)

$$m_x=h_x\sqrt{|B|}(1-\alpha_x^2), \quad m_y=-h_x\sqrt{|B|}\alpha_x\alpha_y.$$

Substituting the equilibrium values of α_x and α_y, we arrive at the field dependences for magnetization (Fig. 3):

$$m_x^{(1)}=m_x^{(2)}=\frac{1}{4}h\sqrt{|B|}(2+\sqrt{1+2h^2}),$$
$$m_y^{(1)}=-m_y^{(2)}=\frac{1}{4}h\sqrt{|B|}\sqrt{3-2h^2}. \tag{11}$$

It follows from the above digression that the magnetic field component h_y induces in this case a PT1 between the phases (11). This transition is accompanied by a magnetization jump (of the component m_y (11)). In this case, the sharp tip $h=h_1$, $\psi=0$ corresponds to the termination of PT1. (Here, $\varphi_{1,2}=\pi/2$.) Similar phase transitions are also observed on other curves (9).

Equilibrium and metastable states for the potential (6) were studied earlier for two symmetric directions of the field in the basal plane, i.e., along the easy magnetization axes, as

well as along directions forming an angle of 30° with the easy axes.[9] The results obtained by us for these directions coincide with those obtained by Bar'yakhtar and Sobolev,[9] who analyzed the evolution of magnetic states in a field parallel to the easy axis and concluded that a second-order phase transition occurs for $h=h_1$ from the symmetric phase $\mathbf{l}\perp\mathbf{h}$ ($h>h_1$) to a low-symmetry phase with the antiferromagnetism vector directed at an angle to the field ($h<h_1$) (see, for example, Ref. 10). The component of $\mathbf{l}$ parallel to the field plays the role of the order parameter. We have shown in this work that the ''nonsymmetric phase'' regions on the $h_x h_y$ phase diagram (curves *9*) are PT1 curves, while the values of the field $h=h_1$ are points of termination of the corresponding PT1. Formally, these critical points can be treated as isolated second-order phase transition points. However, since any deviation of the field from the easy axis lowers the symmetry of the phase $\mathbf{l}\perp\mathbf{h}$ (''blurs'' the transition), such a transition cannot be observed physically. The question of limited applicability of the second-order phase transition concepts to spin-reorientational phase transitions in magnets has been discussed in general by Bar'yakhtar *et al.*[11]

It is also worth noting that the critical curves (8) have a shape characteristic of lability lines in magnets with a spontaneous magnetization (e.g., the *Stoner–Wohlfarth astroid* for a uniaxial ferromagnet[12,13]) as well as in easy-plane tetragonal antiferromagnets.[14]

In the framework of the theory of Whitney's smooth mapping singularities, the lability curves are singular lines describing the *bifurcational* variations in the systems and displaying two possible types of mapping singularities, viz. folds, i.e., curves of type (8), and gathers, i.e., sharp tips.[15] Numerous examples of mathematical problems describing such critical processes in physics, engineering, biology and other areas can be found in Refs. 15 and 16.

2. DOMAIN STRUCTURES

It is well known that in multisublattice magnets of finite size, demagnetizing fields stabilize the domain structure (DS) comprising of competing phase domains in the region of the field induced PT1.[10,11] Such multidomain structures are analogous to the domains of a demagnetized ferromagnet.

In the thermodynamic approximation,[17] the equilibrium states for a two-phase DS are defined by the equation

$$\mathbf{H}^{(e)}=\mathbf{H}_t+4\pi M_0\hat{\mathbf{N}}\cdot[\mathbf{m}^{(1)}\xi_1+\mathbf{m}^{(2)}\xi_2], \tag{12}$$

where $\mathbf{H}_t$ is the field corresponding to PT1; ξ_1 and $\xi_2=(1-\xi_1)$ are phase fractions of the two-phase DS, and $\hat{\mathbf{N}}$ is the tensor of demagnetizing coefficients. Substituting into (12) the expressions for $\mathbf{H}_t$, $\mathbf{m}^{(1)}$ and $\mathbf{m}^{(2)}$, we obtain the dependence of the equilibrium values of ξ, φ_1, and φ_2 on the external field $\mathbf{H}^{(e)}$. For $\xi_{1(2)}=0$ and $\xi_{2(1)}=1$, formula (12) defines the walls of the DS. Figure 4 shows the $h_x^{(e)}h_y^{(e)}$ diagram for a spherical sample with $B<0$ ($N=1/3$). The hatched area corresponds to the region in which DS is observed.

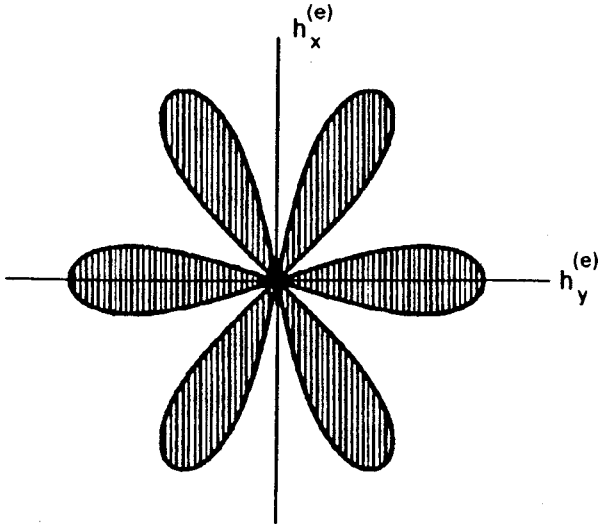

FIG. 4. Regions of existence of domains in a spherical sample.

We shall also study the domain walls (DW) for the DS under consideration. For the sake of definiteness, we shall consider the PT1 curve for $B<0$, $\psi=0$, $|h|\leqslant\sqrt{3/2}$. In this case, the domain wall separates the domains in which the equilibrium states φ_1 and φ_2 are defined by formula (8). In particular, the angle φ of rotation in such a DW is 60° for $h=0$ (see Fig. 1a) and decreases monotonically with increasing field, vanishing at the point $|h|=\sqrt{3/2}$ of termination of PT1. Since $m\ll 1$ in the entire range of PT1, it can be assumed that the DW energy is defined only by the quantity $\mathbf{l}$. Let us find the energy density E_G and the distribution $\varphi(x)$ in the domain wall under consideration. The energy density in a DW and the distribution $\varphi(x)$ are defined by the standard relations:[18]

$$E_G=\int_{\varphi_1^0}^{\varphi_2^0}\sqrt{\alpha[\Phi(\varphi)-\Phi_0]}\,d\varphi, \tag{13}$$

$$x=\int_0^{\varphi}\left[\frac{\alpha}{\Phi(\varphi)-\Phi_0}\right]^{1/2}d\varphi, \tag{14}$$

where φ_1^0 and φ_2^0 are the equilibrium values of the angle φ in adjacent domains, which are defined by formulas (8), α the nonuniform exchange interaction constant, and $\Phi_0=\Phi(\varphi_1^0)=\Phi(\varphi_2^0)$ Substituting the expression for $\Phi(\varphi)$ into (13), we obtain

$$E_G=\sqrt{\frac{2\alpha}{3}}\int_{\varphi_1^0}^{\varphi_2^0}(\cos 2\varphi+\sqrt{b})\sqrt{-\cos 2\varphi+2\sqrt{b}}\,d\varphi, \tag{15}$$

where $b=h^2+1/2$.

Figure 5 shows the results of numerical integration of the DW energy $E_W=E_G/\sqrt{\alpha}$ as a function of the external field. Similarly, for the distribution $\varphi(x)$, we obtain

$$x=\int_0^{\varphi}\left(\frac{3\alpha}{2(\cos 2\varphi+\sqrt{b})\sqrt{-\cos 2\varphi+2\sqrt{b}}}\right)^{1/2}d\varphi. \tag{16}$$

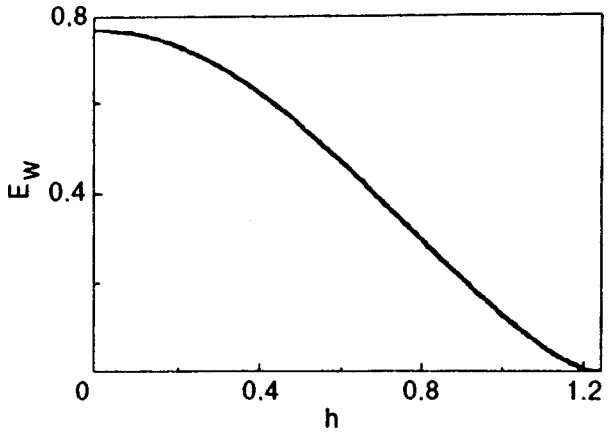

FIG. 5. Energy of a domain wall at the PT1 curve.

The dependences $\varphi(\xi)=\varphi(x/\sqrt{\alpha})$ for some values of the external field h are presented in Fig. 6.

3. EVOLUTION OF MAGNETIC STATES

So far, detailed investigations of the magnetic properties of easy-plane hexagonal crystals have been carried out only in $RbMnCl_3$ single crystals at $T=4.2$ K.[7,8] It was mentioned in these works that the investigated samples of $RbMnCl_3$ contain regions with different orientations of antiferromagnetism vectors (antiferromagnetic domains). Such domains are created in antiferromagnets during the formation of an ordered state upon a transition from the paramagnetic phase.[19] On account of the degeneracy of the ground state (see (7)), hexagonal easy-plane antiferromagnets have three types of domains with different orientations of the antiferromagnetism vector (the states with $\mathbf{l}$ and $-\mathbf{l}$ are physically equivalent). It was also found that magnetostriction leads to rhombic distortions in domains.[8] Thus, the samples studied in Refs. 7 and 8 consist of three types of orthorhombic domains whose axes are rotated through 60° relative to one another. Such a multidomain structure hampers the formation of thermodynamically stable states, and the field dependences of magnetization are mainly determined by complex irreversible processes in which elastic and magnetoelastic interactions as well as microinhomogeneities of the crystal play an important role. For example, sharp jumps in magnetization observed by Bazhan *et al.*[7] for certain directions of the planar field are probably due to the stability loss of metastable states formed in a part of the domains, and not to the orientational phase transitions in the bulk of the magnet.

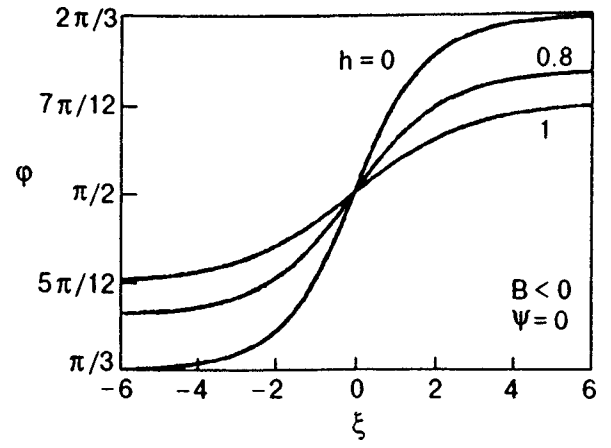

FIG. 6. Structure of domain walls for some values of magnetic field at the PT1 curve.

However, some results on the investigation of magnetization curves are in accord with our conclusions on phase transitions induced by a planar field and the related transitions of stable domain structures. Thus, in a magnetic field parallel to one of the easy axes, the field dependence of the longitudinal magnetization in weak fields displays a characteristic nonlinear region (like the one shown in Fig. 3a), while the magnetization curve becomes linear in stronger fields ($H>15$ kOe at $T=4.2$ K).

If the magnetic field intersects the region of existence of domains along directions not coinciding with curves (7), the fractions of phases in DS are not equal, the magnetization component normal to the field is nonzero, and its field dependence is close to that shown in Fig. 3b. These conclusions are also in good accord with the results obtained by Bazhan *et al.*[7]

It follows from what has been stated above that the effect of magnetic field on equilibrium states must be studied in monodomain samples. In this connection, it should be recalled that the formation of antiferromagnetic domains is not advantageous from the energy point of view since the increase in the system energy due to the formation of domain walls is not compensated by a decrease in any of energy contributions. This distinguishes such domain structures from regular magnetic domains in which the energy increase due to magnetic inhomogeneities is compensated by a gain in the energy of demagnetizing fields. Equilibrium geometrical parameters of regular domain structures are determined by a competition between these opposing factors in the overall energy balance of the system and can vary easily under the effect of external parameters (magnetic field and temperature). Conversely, the antiferromagnetic domains owe their origin to the kinetics of formation of the ordered state upon cooling of the sample below Néel temperature. They are distributed randomly over the bulk of the magnet and their shape changes only slightly under the effect of external agencies.[19]

According to the results obtained in Refs. 7 and 8, a strong magnetic field (exceeding the lability field (8)) violates metastable states, and a phase with $\mathbf{l}\perp\mathbf{h}$ is realized in all antiferromagnetic domains. It can be expected that such spin states are preserved in domains even upon a decrease in the field. This method was earlier used for suppressing metastable states in cubic helimagnets.[20,21] Another method of formation of monodomain states is associated with cooling of the sample in a magnetic field. This method was used by Andrienko and Prozorova.[8] However, it was found that cooling from room temperature to helium temperatures in a field

$H \approx 10$ kOe does not affect significantly the resonance properties of the investigated samples of $RbMnCl_3$.

CONCLUSIONS

We have calculated the equilibrium states of a hexagonal planar collinear antiferromagnet in a planar magnetic field. On the $h_x h_y$ phase diagram of the antiferromagnet under investigation, the region of metastable states is bounded by curve (8). The rotation of the magnetic field in this region leads to spin-reorientational phase transitions accompanied by magnetization jumps. Thermodynamically stable domain structures consisting of domains of competing phases are formed in the region of these phase transitions. The boundaries of such a domain structure are determined and the structure and equilibrium parameters of plane domain walls are calculated. The results of calculations were used to construct the phase diagrams of the investigated magnets in components of fields applied to the basal plane.

Until recently, the equilibrium states were not studied experimentally in hexagonal easy-plane antiferromagnets. However, some results[7,8] obtained for multidomain samples of $RbMnCl_3$ are in accord with the results of our investigations.

The main results obtained in this work remain valid even if the magnetic field deviates from basal plane towards the hexagonal axis. In hexagonal uniaxial antiferromagnets in a magnetic field higher than the reversal field, the antiferromagnetism vector lies in the basal plane. In this case, the hexagonal anisotropy leads to a degeneracy of the ground state (cf. (7)). For deviations of the magnetic field from the easy axis, this would lead to phase transitions similar to those described above.

The authors are obliged to Alexander von Humboldt Foundation for providing the computers. We are also indebted to V. G. Bar'yakhtar for a discussion of several problems considered in this work, and to A. A. Shestakov for his help in numerical computations.

*E-mail: bogdanov@host.dipt.donetsk.ua

[1] A. Oles, F. Kajzar, M. Kucab, and W. Sikora, *Magnetic Structures Determined by Neutron Diffraction*, Warsaw (1976).
[2] K. S. Aleksandrov, A. T. Anistratov, B. V. Beznosikov, and N. V. Fedoseeva, *Phase Transitions in* ABX_3 *Halide Crystals* [in Russian], Nauka, Novosibirsk (1981).
[3] K. S. Aleksandrov, N. V. Fedoseeva, and I. P. Spivakova *Magnetic Phase Transitions in Halide Crystals* [in Russian], Nauka, Novosibirsk (1983).
[4] T. Asano, Y. Ajiro, M. Mekata *et al.*, Physica B **201**, 75 (1994).
[5] I. M. Vitebskii, O. A. Petrenko, S. V. Petrov, and L. A. Prozorova, Zh. Éksp. Teor. Fiz. **103**, 326 (1993) [JETP **76**, 178 (1993)].
[6] M. E. Zhitomirskii, O. A. Petrenko, and L. A. Prozorova, Phys. Rev. B **52**, 3511 (1995).
[7] F. N. Bazhan, N. V. Fedoseeva, S. V. Petrov, and B. V. Beznosikov, Zh. Éksp. Teor. Fiz. **74**, 1698 (1978) [Sov. Phys. JETP **47**, 886 (1978)].
[8] A. V. Andrienko and L. A. Prozorova, Zh. Éksp. Teor. Fiz. **74**, 1527 (1978) [Sov. Phys. JETP **47**, 798 (1978)].
[9] V. G. Bar'yakhtar and V. L. Sobolev, Fiz. Nizk. Temp. **3**, 1329 (1977) [Sov. J. Low Temp. Phys. **3**, 642 (1977)].
[10] A. F. G. Wyatt, J. Phys. C **1**, 684 (1968).
[11] V. G. Bar'yakhtar, A. E. Borovik, and V. A. Popov, Pis'ma Zh. Éksp. Teor. Fiz. **9**, 634 (1969) [JETP Lett. **9**, 391 (1969)].
[12] E. Stoner and E. Wohlfarth, Philos. Trans. R. Soc. London, Ser. A **A240**, 559 (1948).
[13] L. D. Landau and E. M. Lifshitz, *Electrodynamics of Continuous Media* [in Russian], Nauka, Moscow (1982).
[14] A. N. Bogdanov, Fiz. Tverd. Tela (Leningrad) **32**, 1749 (1990) [Sov. Phys. Solid State **32**, 1018 (1990)].
[15] R. Gilmore, *Catastrophe Theory for Scientists and Engineers*, Wiley, New York (1981).
[16] T. Poston and I. Stewart, *Catastrophe Theory and Its Applications*, Pitman, London (1978).
[17] V. G. Bar'yakhtar, A. N. Bogdanov, and D. A. Yablonskii, Usp. Fiz. Nauk **156**, 47 (1988) [Sov. Phys. Usp. **31**, 810 (1988)].
[18] A. Hubert, *Theorie der Domanenwande in geordneten Medien*, Springer, Heidelberg (1974).
[19] V. V. Eremenko, N. F. Kharchenko, Yu. G. Litvinenko, and V. M. Naumenko, *Magnetooptics and Spectroscopy of Antiferromagnets* [in Russian], Naukova Dumka, Kiev (1989).
[20] J. Beille, J. Voiron, F. Towfiq *et al.*, J. Phys. F **11**, 2153 (1981).
[21] B. Lebech, J. Bernhard, T. Freltoft, J. Phys.: Condens. Matter **1**, 6105 (1989).

Translated by R. S. Wadhwa

ELECTRONIC PROPERTIES OF METALS AND ALLOYS

Screening of electrostatic potential in a composite fermion system

D. V. Fil

*Institute of Single Crystals, National Academy of Sciences, 310001 Kharkov, Ukraine**
(Submitted June 29, 1998)
Fiz. Nizk. Temp. **24**, 1144–1150 (December 1998)

Screening of the electric field of a test charge by monolayer and double-layer composite fermion systems is considered taking into account the influence of the sample boundary. It is shown that the test charge field is partly screened in the system at distances much larger than the magnetic length. The value of screening as a function of distance depends considerably on the filling factor. The effect of variation of the value of screening in a double-layer system upon a transition to a state described by the Halperin wave function is determined. © *1998 American Institute of Physics.* [S1063-777X(98)00312-0]

The model of composite fermions was proposed by Jain[1] to describe the systematically fractional filling factors observed in experiments on fractional quantum Hall effect. It was shown in Ref. 1 that the Laughlin wave function has a topological structure equivalent to that of a system of composite quasiparticles carrying the statistical charge and the statistical gauge field flux. In the mean field approximation, the interaction of composite quasiparticles with the gauge field is reduced to the action of a self-consistent field which partially screens the external magnetic field. Consequently, the fractional quantum Hall effect in the electron system emerges as an integer quantum Hall effect in a system of composite fermions.

Lopez and Fradkin[2] and Halperin, Lee, and Read[3] developed the Chern–Simons formalism for describing a system of composite fermions. The starting point for such a formalism is the Lagrangian of fermions interacting with the Chern–Simons gauge field. In this formalism, the mean field approximation corresponds to the stationary configuration of the effective Lagrangian of the gauge field obtained as a result of functional integration with respect to fermion fields in the expression for the partition function of the system. The formalism allows us to introduce systematically the corrections to the mean-field solution by expanding the effective Lagrangian in small deviations of the gauge field from the mean-field configuration.

The approach developed in Refs. 2 and 3 was generalized by Lopez and Fradkin[4] to the case of a double-layer system. A specific feature of such a system is the possibility of formation of generalized Laughlin states whose multiparticle wave function is characterized by an additional set of zeros for coinciding x,y coordinates of electrons in the opposite layers (here and below, the z-axis is chosen normal to the two-dimensional electron layer). The wave function for such generalized states was proposed by Halperin.[5] Although the original analysis presented in Ref. 5 concerns a monolayer system of unpolarized electrons, the wave function proposed by Halperin can be easily generalized to the case of a two-layered system if the pseudospin, which corresponds to the layer number, is introduced. The emergence of generalized states of the type 5 results in the appearance of new (different from monolayer) filling factors corresponding to the Hall plateau. In particular, the quantum Hall effect emerges for a filling factor $\nu=1/2$, which is indeed observed in experiments.[6,7] Moreover, for certain fixed values of the filling factor in two-layered systems, a phase transition between different generalized Laughlin states becomes possible upon a change in the separation between the layers.[8]

Thus, a two-dimensional electron gas in the fractional quantum Hall effect regime is characterized by a complex system of classification of ground states, the transition between different states occurring upon a variation of the external magnetic field or of the separation between the layers (in double-layer systems).

In this work, we study the effect of screening of the external electrostatic potential by a system of composite fermions as a function of its ground state structure. We consider the screening of the field of a test charge located at the boundary of a semi-infinite medium with permittivity ε, having at a certain distance from the boundary a two-dimensional electron layer (or a double layer system) in the fractional quantum Hall effect regime. Since the electron system in this case is incompressible, there is no screening at a large distance from the test charge, although the electric field may deviate considerably from unscreened field of the test charge at finite distances. The specific form of the dependence $E(r)$ is defined by the type of the state in which the system is located. Thus, the effect considered in this work may be used for identifying the topological order prevailing in the system as a function of external parameters.

1. MONOLAYER SYSTEM IN AN INFINITE MEDIUM

To begin with, let us consider the problem of screening in an infinite medium containing a two-dimensional electron layer in the fractional quantum Hall effect regime. In order to

 © 1998 American Institute of Physics

describe the system, we consider the model of spinless fermions Ψ (it is assumed that electrons are completely polarized in spin) interacting with the two-dimensional Chern–Simons gauge field a_μ and the electromagnetic field A_μ. The action of the system has the form

$$S=S_{CF}+S_{\rm em}, \tag{1}$$

where

$$S_{CF}=\int dt\, d^2r\Bigg[\Psi^*(\mathbf{r})\Bigg(i\partial_t+\mu-a_0-eA_0 - \frac{1}{2m}\left(i\nabla_2+\mathbf{a}+\frac{e}{c}\,\mathbf{A}^{\rm pl}\right)^2\Bigg)\Psi(\mathbf{r})+\frac{1}{2\pi\varphi}\,a_0 b\Bigg], \tag{2}$$

$$S_{\rm em}=\frac{1}{8\pi}\int dt\, d^3r(\varepsilon\mathbf{E}^2-\mathbf{B}^2). \tag{3}$$

In Eq. (2), m is the mass of composite fermions, μ the chemical potential, $b=\partial_x a_y-\partial_y a_x$ the ''magnetic'' component of the gauge field, $\mathbf{A}^{\rm pl}=\mathbf{i}_x A_x+\mathbf{i}_y A_y$; $\nabla_2=\mathbf{i}_x\partial_x+\mathbf{i}_y\partial_y$, and φ the number of gauge field flux quanta transported by a composite quasiparticle (φ is even). It is assumed that the distribution of composite fermions along the z-axis is described by a δ-function. Transverse gauge is used for the field $a(\partial_i a_i=0)$. For the electromagnetic field also, we used transverse gauge in the plane $(\partial_x A_x+\partial_y A_y=0)$.

Functional integration with respect to Ψ in the expression for the partition function of the system

$$Z=\int D\Psi^* D\Psi Da_\mu\,\exp(iS) \tag{4}$$

gives the following effective action for a system of interacting gauge and electromagnetic fields:

$$S_{\rm eff}(a,A)=-i\ {\rm Tr}\ \ln\Bigg[i\partial_t+\mu-a_0-eA_0-\frac{1}{2m}\times\left(i\nabla_2+\mathbf{a}+\frac{e}{c}\,\mathbf{A}^{\rm pl}\right)^2\Bigg]+\int dt\, d^2r\times\frac{1}{2\pi\varphi}\,a_0 b+S_{\rm em}. \tag{5}$$

The condition of stationary configuration of the action (5) upon variation of the field a_μ defines the value of the self-consistent effective field acting on composite fermions:

$$B_{\rm eff}=B-\frac{2\pi c\varphi}{|e|}\,n_0, \tag{6}$$

where n_0 is the average electron concentration. The fractional quantum Hall effect is observed for an integral number N of filled Landau levels in a field $B_{\rm eff}$, which corresponds to the filling factor $\nu=N/[\varphi N+{\rm sgn}(B_{\rm eff})]$.

We shall confine the subsequent analysis to a consideration of the part of the effective action (5) that is quadratic in fluctuations of the fields a_μ and A_μ. In order to solve the problem considered here, we take only time-independent fluctuations into account. Expansion of the action (5) in the vicinity of the stationary configuration gives

$$S^{(2)}_{\rm eff}(a,A)=\frac{1}{2}\int dt\, d^2q[(a^*_\mu(\mathbf{q})+\tilde{A}^*_\mu(\mathbf{q}))\Pi^{\Psi}_{\mu\nu}(q)(a_\nu(\mathbf{q})+\tilde{A}_\nu(\mathbf{q}))+a^*_\mu(\mathbf{q})\Pi^{CS}_{\mu\nu}(q)a_\nu(\mathbf{q})]+\frac{1}{2}\times\int dt\, d^2q\, dq_z A^*_\mu(\mathbf{q},q_z)\Pi^{\rm em}_{\mu\nu}(q,q_z)A_\nu(\mathbf{q},q_z), \tag{7}$$

where the subscripts μ and ν assume the values 0 and 1 corresponding respectively to zeroth and transverse components of the fields a_μ and A_μ in the (x,y) plane (in Eq. (7), we disregard the contribution of the component A_z which can be put equal to zero without any loss of generality in the time-independent problem under consideration), and q is the wave vector component parallel to the (x,y) plane. In Eq. (7), $\tilde{A}_0(\mathbf{q})=eA_0(\mathbf{q},z=0)$, $\tilde{A}_1(\mathbf{q})=(e/c)A_1(\mathbf{q},z=0)$,

$$\Pi^{\Psi}_{\mu\nu}(q)=-\frac{1}{2\pi\omega_c}\begin{pmatrix} q^2\Sigma_0 & iq\omega_c\Sigma_1 \\ -iq\omega_c\Sigma_1 & \omega_c^2(\Sigma_2+N)\end{pmatrix}, \tag{8}$$

$$\Pi^{CS}_{\mu\nu}(q)=\frac{1}{2\pi\varphi}\begin{pmatrix} 0 & iq \\ -iq & 0\end{pmatrix}, \tag{9}$$

$$\Pi^{\rm em}_{\mu\nu}(q,q_z)=\frac{1}{4\pi}\begin{pmatrix} \varepsilon(q^2+q_z^2) & 0 \\ 0 & -(q^2+q_z^2)\end{pmatrix}. \tag{10}$$

In Eq. (8), we have introduced the notation

$$\Sigma_j(q)=-[{\rm sgn}(B_{\rm eff})]^j{\rm e}^{-x}\sum_{n=0}^{N-1}\sum_{m=N}^{\infty}\times\frac{n!}{m!}\,\frac{x^{m-n-1}}{(m-n)}\,[L_n^{m-n}(x)]^{2-j}\times\left((m-n-x)L_n^{m-n}(x)+2x\,\frac{dL_n^{m-n}(x)}{dx}\right)^j, \tag{11}$$

where $x=(ql_{\rm eff})^2/2$, $l_{\rm eff}=(N/2\pi n_0)^{1/2}$ is the effective magnetic length, $\omega_c=2\pi n_0/(mN)$ is the effective cyclotron frequency, and $L_n^{m-n}(x)$ is the generalized Laguerre polynomial. The quantities (11) are computed through Green's current–current functions for the fermion system in a field $B_{\rm eff}$ (the temperature is assumed to be equal to zero). Expressions of the type (11) were first derived in the theory of anyons.[9]

Integration over fluctuations of the field a leads to the following expression for the action of the electromagnetic field:

$$S(A)=\frac{1}{4\pi}\int dt\, dq_z dq_z' d^2q A^*_\mu(\mathbf{q},q_z)\Lambda_{\mu\nu}(q)A_\nu(\mathbf{q},q_z')+\frac{1}{2}\int dt\, dq_z d^2q A^*_\mu(\mathbf{q},q_z)\Pi^{\rm em}_{\mu\nu}(q,q_z)A_\nu(\mathbf{q},q_z), \tag{12}$$

where

$$\Lambda_{\mu\nu}(q)=-\frac{e^2}{2\pi\omega_c\Delta_2}\times\begin{pmatrix} q^2\Sigma_0 & iqc^{-1}\omega_c(\Sigma_1+\varphi\Delta_1)\\ -iqc^{-1}\omega_c(\Sigma_1+\varphi\Delta_1) & c^{-2}\omega_c^2(\Sigma_2+N)\end{pmatrix}, \tag{13}$$

with

$$\Delta_1=\Sigma_0(\Sigma_2+N)-\Sigma_1^2, \tag{14}$$

$$\Delta_2=(1-\varphi\Sigma_1)^2-\varphi^2\Sigma_0(\Sigma_2+N). \tag{15}$$

Here and below, we omit the arguments of the functions Σ_j and Δ_j to keep the expressions simple.

Action (12) leads to the following expression for the electromagnetic field potential in a system with a test charge $e_{\rm ext}$ placed at the origin:

$$\frac{1}{2\pi}\int dq_z'\Lambda_{\mu\nu}(q)A_\nu(\mathbf{q},q_z')+\Pi^{\rm em}_{\mu\nu}(q,q_z)A_\nu(\mathbf{q},q_z)=\delta_{\mu 0}j_0, \tag{16}$$

where $j_0=e_{\rm ext}/(2\pi)^{3/2}$. The solution of Eq. (16) is sought in the form

$$A_\mu(\mathbf{q},q_z)=\frac{C_\mu(q)}{q^2+q_z^2}. \tag{17}$$

Consequently, we obtain the following expression for the quantity $A_0(\mathbf{q},q_z)$:

$$A_0(\mathbf{q},q_z)=\frac{4\pi j_0}{q^2+q_z^2}\left(\varepsilon-\frac{qe^4c^{-2}\omega_c\Delta_1+q^2e^2\Sigma_0}{e^2c^{-2}\omega_c^2(\Sigma_2+N)+q\omega_c\Delta_2}\right)^{-1}. \tag{18}$$

In the electrostatic limit ($c\to\infty$), formula (18) is reduced to the form

$$A_0(\mathbf{q},q_z)=\frac{4\pi j_0}{\varepsilon}\frac{1}{q^2+q_z^2}\left(1+\frac{f_q\Sigma_0}{\Delta_2-f_q\Sigma_0}\right), \tag{19}$$

where $f_q=e^2q/\varepsilon\omega_c$. Formula (19) differs from (18) significantly only for

$$q<\frac{e^2\omega_c}{c^2}. \tag{20}$$

The values of q satisfying this inequality (20) are several orders of magnitude lower than the characteristic scale of wave vectors of the problem $\sim l_{\rm eff}^{-1}$. A consideration of the difference between Eqs. (18) and (19) in the region (20) leads to a very weak screening of the electric field of the test charge at large distances. Here and below, we shall not analyze this very weak effect, but confine to the approximate expression (19). Note that this approximation corresponds to negligible nondiagonal components of the tensor Λ in Eq. (16), which will be taken into consideration in the following sections.

The expression for the component of the screened electric field of a test charge parallel to the plane, calculated from (19) for $z=0$, has the form

$$E_{\rm pl}(r)=-\frac{e_{\rm ext}}{\varepsilon r^2}(1+F(r)), \tag{21}$$

where r is the distance up to the test charge, and

$$F(r)=r^2\int dq\,J_1(qr)\frac{qf_q\Sigma_0}{\Delta_2-f_q\Sigma_0} \tag{22}$$

($J_i(x)$ is the Bessel function).

To complete the picture, we also present the expression for the z-component of the magnetic field (for $z=0$) induced by the test charge:

$$\delta B_z(r)=-\frac{e_{\rm ext}e^2}{c\varepsilon}\int dq\,qJ_0(qr)\frac{\Sigma_1+\varphi\Delta_1}{\Delta_2-f_q\Sigma_0}. \tag{23}$$

In this expression (23) also, we have omitted the correction emerging in the region (20). For characteristic values of the parameters and for $e_{\rm ext}=e$, the numerical estimate for δB_z is found to be smaller than 1 Oe for all r, i.e., the effect is of theoretical interest only. From the experimental point of view, the most important effect is associated with the deviation of $F(r)$ from zero in formula (21), which may be of the order of unity for finite values of r, while the specific form of the dependence $F(r)$ is determined to a considerable extent by the ground state of the quantum Hall system and is modified significantly upon a transition to another Hall step. The following two sections are devoted just to an analysis of this effect in a semi-infinite medium.

2. MONOLAYER SYSTEM IN A SEMI-INFINITE MEDIUM

Let us now consider the geometry which appears to be most appropriate for observing the screening effect. We shall assume that the test charge is located at the surface of a semi-infinite medium with permittivity ε. At a distance a from the surface, the medium contains a two-dimensional electron layer in the fractional quantum Hall effect regime. We shall seek an expression for the screened field of a test charge at the interface.

Disregarding the nondiagonal components of the tensor Λ, we can present Eq. (16) in the geometry under consideration as follows:

$$\frac{1}{2\pi}\int dq_z'\left(e^{i(q_z-q_z')a}\Lambda_{00}(q)+\varepsilon_{q_z-q_z'}\frac{q^2+q_zq_z'}{2}\right)A_0(\mathbf{q},q_z')=j_0, \tag{24}$$

where

$$\varepsilon_{q_z}=\frac{\varepsilon+1}{2}\delta(q_z)+i\frac{\varepsilon-1}{2\pi}P\left(\frac{1}{q_z}\right). \tag{25}$$

The solution of Eq. (24) is sought in the form

$$A_0(\mathbf{q},q_z)=\frac{C_1(q)+C_2(q)e^{iq_za}}{q^2+q_z^2}. \tag{26}$$

As a result, we arrive at the following expression for the electrostatic field in the plane (x,y) at the interface:

$$E_{\rm pl}(r)=-\frac{e_{\rm ext}}{\varepsilon' r^2}(1+F_1(r)), \tag{27}$$

where

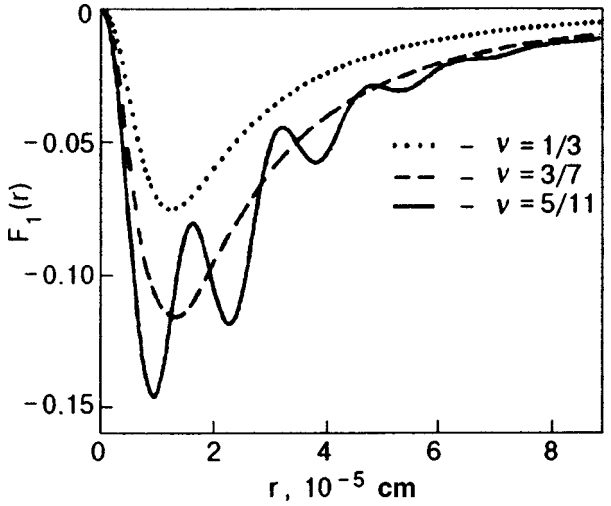

FIG. 1. Relative screening of the test charge field by a monolayer system.

$$F_1(r)=\frac{\varepsilon}{\varepsilon'}\,r^2\int dq\,J_1(qr)\times\frac{qf_q\Sigma_0 e^{-2qa}}{\Delta_2-f_q\Sigma_0(1+(\varepsilon-1)(\varepsilon+1)^{-1}e^{-2qa})} \quad (28)$$

with $\varepsilon'=(\varepsilon+1)/2$.

The dependence $F_1(r)$ is shown in Fig. 1 for filling factors $\nu=1/3, 3/7, 5/11$. Calculations were made by using the following values of the parameters: $n_0=10^{11}\,\mathrm{cm}^{-2}$, $m=0.25m_e$, $\varepsilon=12.6$, $a=500$ Å. It can be seen from the figure that the system has a significant screening of the electric field of the test charge at distances considerably larger than the magnetic length. As the filling factor ν approaches the value 1/2, the dependence $F_1(r)$ becomes oscillatory. Note that an increase in the value of a weakens the effect. A decrease in this parameter leads not only to an increase in the amplitude of the effect, but also to a wider range of filling factors for which F_1 oscillates as a function of the distance. In particular, numerical computations for the geometry considered in Sec. 1 lead to an oscillatory dependence $F(r)$ for all filling factors corresponding to the fractional quantum Hall effect. In order to observe these oscillations, we must measure the electric field inside the dielectric medium. For the case considered in this section, oscillations emerge when the effective magnetic length becomes of the order of 2a.

3. DOUBLE-LAYER SYSTEM IN A SEMI-INFINITE MEDIUM

Let us now consider the screening of the field of a test charge by a double-layer electron system. We shall consider a system in which the states described by Halperin's wave function[5] are realized. Such a system can be described by introducing two types of Chern–Simons fields corresponding to statistical charges belonging to composite quasiparticles in opposite layers, and to an additional term in the Lagrangian of the system, which is nondiagonal in gauge fields. The action of the system has the form

$$S_{CF}=\int dt\,d^2r\sum_{k=1}^{2}\left\{\Psi_k^*(r)\left[i\partial_t+\mu-a_{k0}-eA_{k0}-\frac{1}{2m}\times\left(i\nabla_2+\mathbf{a}_k+\frac{e}{c}\,\mathbf{A}_k^{\mathrm{pl}}\right)^2\right]\Psi_k(r)+\sum_{k,k'=1}^{2}\Theta_{kk'}a_{k0}b_{k'}\right\}, \quad (29)$$

where A_{k0} and $\mathbf{A}_k^{\mathrm{pl}}$ are the scalar and vector components of the electromagnetic field potential in the layer k, and

$$\Theta_{kk'}=\frac{1}{2\pi(\varphi^2-s^2)}\begin{pmatrix}\varphi & -s\\ -s & \varphi\end{pmatrix}. \quad (30)$$

In this equation, (30) φ and s are the numbers of gauge field flux quanta carried by a composite quasiparticle, which correspond to the statistical charges of quasiparticles in the same layer and in the adjoining layer respectively. (φ is even while s is an arbitrary integer). For the sake of simplicity, we confine the analysis to two equivalent layers. Fractional quantum Hall effect in the system (29) is realized for filling factors $\nu=2N/[(\varphi+s)N\pm1]$ ($\nu=2\nu_i$, where ν_i is the filling factor per layer). Carrying out a procedure analogous to the one in Sec. 1, we arrive at the following expression for the action of the electromagnetic field of the system (29):

$$S(A)=\frac{1}{2}\int dt\,d^2q A_{k\mu}^*(\mathbf{q})\Lambda_{kk'\mu\nu}(q)A_{k'\nu}(\mathbf{q})+S_{\mathrm{em}}, \quad (31)$$

where

$$\hat{\Lambda}_{kk'}=\frac{1}{2}\begin{pmatrix}\hat{\Lambda}^+ +\hat{\Lambda}^- & \hat{\Lambda}^+ -\hat{\Lambda}^-\\ \hat{\Lambda}^+ -\hat{\Lambda}^- & \hat{\Lambda}^+ +\hat{\Lambda}^-\end{pmatrix}. \quad (32)$$

Matrices $\hat{\Lambda}^+$ and $\hat{\Lambda}^-$ in Eq. (32) are defined by formulas (13)–(15) in which the parameter φ is replaced by $\varphi+s$ and $\varphi-s$ respectively. Note that although formulas (29) and (30) become meaningless for $\varphi=s$, the expressions (31) and (32) remain valid even in this case. The situation $\varphi=s$ corresponds to infinite rigidity of the antiphase oscillations of gauge fields. Going over in (29) and (30) to new variables corresponding to synphase and antiphase oscillations, we must consider for the integration variables in the case $\varphi=s$ only synphase oscillations of the fields $a_{i\mu}$ and put the variable corresponding to antiphase oscillations equal to zero. It can be easily verified that in this case also we arrive at the relations (31) and (32).

For the geometry in which the z-coordinate of the first and second layer is equal to $-a$ and $-(a+d)$ respectively, we obtain from (31) the following equation for the scalar potential of the system:

$$\frac{1}{4\pi}\int dq_z'\{e^{i(q_z-q_z')a}[(\Lambda_{00}^+(q)+\Lambda_{00}^-(q))(1+e^{i(q_z-q_z')d})+(\Lambda_{00}^+(q)-\Lambda_{00}^-(q))(e^{-iq_z'd}+e^{iq_zd})]+\varepsilon_{q_z-q_z'}(q^2+q_zq_z')\}A_0(\mathbf{q},q_z')=j_0, \quad (33)$$

where the nondiagonal components of the tensors Λ^+ and Λ^- are neglected as before.

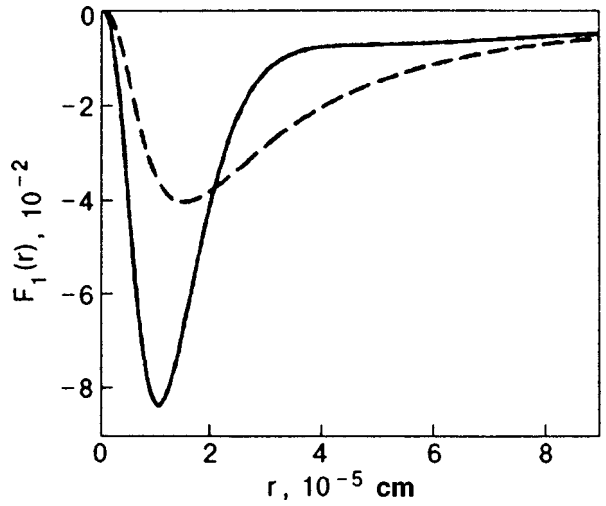

FIG. 2. Relative screening of the test charge field by a double-layer system for $\nu=2/5$, $\varphi=2$, and $s=2$ (solid curve) and $\varphi=4$, $s=0$ (dashed curve).

The solution of Eq. (33) is sought in the form

$$A_0(\mathbf{q},q_z)=\frac{C_1(q)+C_2(q)e^{iq_z a}+C_3(q)e^{iq_z(a+d)}}{q^2+q_z^2}. \quad (34)$$

As a result, we arrive at an expression for the electric field, whose form for $z=0$ coincides with (27) in which the function $F_1(q)$ is modified to the form

$$F_1(r)=\frac{\varepsilon}{\varepsilon'} r^2 \int dq\, J_1(qr) \times \frac{qS_q e^{-2qa}}{R_q-(\varepsilon-1)(\varepsilon+1)^{-1}S_q e^{-2qa}}, \quad (35)$$

where

$$R_q=(\Delta_2^+-f_q E_q^+\Sigma_0)(\Delta_2^--f_q E_q^-\Sigma_0), \quad (36)$$

$$S_q=f_q\Sigma_0\left[\frac{1}{2}(E_q^+)^2\Delta_2^-+\frac{1}{2}(E_q^-)^2\Delta_2^+-f_q E_q^+E_q^-\Sigma_0\right]. \quad (37)$$

In formulas (36) and (37), the functions Δ_2^+ and Δ_2^- are defined by formula (13) in which φ is replaced by $\varphi+s$ and $\varphi-s$ respectively, and $E_q^\pm=(1\pm e^{-qd})$.

It can be seen from formulas (35)–(37) that screening in a two-layer system depends on parameter $\varphi+s$ as well as $\varphi-s$. Hence for a fixed value of the filling factor which depends only on the first of these parameters, the expression (35) differs for the cases $s=0$ and $s\neq 0$. Consequently, a transition from a state with $s=0$ to a state with nonzero s (such a state corresponds to Halperin's wave function) will be manifested in a variation of the dependence of screened field of a test charge on distance.

By way of an example, let us consider a system with filling factor 2/5. In such a system, the fractional quantum Hall effect may correspond to sets of parameters ($\varphi=4$ and $s=0$) and ($\varphi=2$ and $s=2$). Figure 2 shows the dependence $F_1(r)$ for these two cases for the same values of the system parameters as in Sec. 1 and for $d=400$ Å. It can be seen from the curves that the dependences $F_1(r)$ differ considerably for these two cases. An experimental observation of such a sharp variation in screening upon a slight variation in the separation between layers points towards a phase transition between different ground states in a two-layer system. Note that the situation considered in this work differs from the one considered by us in Ref. 10 where we studied screening in a two-layer system in an infinite medium with two test charges located in adjoining layers. In such a case, the screening of the test charge field depends only on parameter $\varphi+s$, and the variation of the spatial distribution of the charge induced during a phase transition between generalized Laughlin states is associated just with a variation of this parameter with a simultaneous reversal of the sign of B_{eff}. Only a few of the possible transitions satisfy this condition. In particular, the transition considered above for $\nu=2/5$ (which is most suitable for observation since it corresponds to lowest level in the hierarchy of the generalized Laughlin states) does not satisfy such a condition. The origin of the effect considered in this work is associated with the asymmetric arrangement of the test charge relative to the two-layer system. In particular, this is manifested in that a decrease in the separation between layers leads to a suppression of the effect.

Thus, we have considered in this work the screening of the field of a test charge by a monolayer and a two-layer systems of composite fermions. The expressions for the screened test charge field are obtained by taking into account the effect of the interface. It is shown that a partial screening of test charge occurs in the system at distances much larger than the magnetic length. The specific form of the dependence of the screened field on the distance from the test charge is modified considerably upon a variation of the ground state of the system. The observation of the screening effect as a function of the filling factor and separation between layers (in a two-layer system) can be treated as a possible experimental verification of the model of composite fermions and the method of recording changes in the topological order in a quantum Hall system. The solutions obtained in this work specify the case when the test charge and the electric field detector are placed on the surface of the sample containing a two-dimensional electron layer. The approach used in this work can be modified easily to describe a different geometry of the experiment.

*E-mail fil@isc.kharkov.ua

[1] J. K. Jain, Phys. Rev. Lett. **63**, 199 (1989).
[2] A. Lopez and E. Fradkin, Phys. Rev. B **44**, 5246 (1991).
[3] B. I. Halperin, P. A. Lee, and N. Read, Phys. Rev. B **47**, 7312 (1993).
[4] A. Lopez and E. Fradkin, Phys. Rev. B **51**, 4347 (1995).
[5] B. I. Halperin, Helv. Phys. Acta **56**, 75 (1983).
[6] Y. W. Suen, L. W. Enhel, M. B. Santos *et al.*, Phys. Rev. Lett. **68**, 1379 (1992).
[7] J. P. Eisenstein, G. S. Boebinger, L. N. Pfeiffer *et al.*, Phys. Rev. Lett. **68**, 1383 (1992).
[8] D. Yoshioka, A. H. MacDonald, and S. M. Girvin, Phys. Rev. B **39**, 1932 (1989).
[9] Y. H. Chen, F. Wilczek, E. Witten, and B. I. Halperin, Int. J. Mod. Phys. B **3**, 1001 (1989).
[10] D. V. Fil, Fiz. Nizk. Temp. **24**, 905 (1998) [Low Temp. Phys. **24**, 681 (1998).

Translated by R. S. Wadhwa

Point-contact spectroscopy of metallic heterojunctions at high frequencies

O. P. Balkashin

*B. Verkin Institute for Low Temperature Physics and Engineering, National Academy of Sciences of the Ukraine, 310164 Kharkov, Ukraine**

(Submitted July 8, 1998)
Fiz. Nizk. Temp. **24**, 1151–1156 (December 1998)

The point-contact spectroscopy is used to study singularities of the electron–phonon spectra of heterojunctions made of different metals Cu–Cu (1 at. % Fe) and Cu–Au. Measurements at high frequencies made it possible to distinguish and identify contributions to the spectrum from the nonequilibrium phonon relaxation. © *1998 American Institute of Physics.* [S1063-777X(98)00412-5]

Point-contact spectroscopy, i.e., the measurement of nonlinear singularities in the electrical conductivity of point contacts at low temperatures, is a very effective tool for studying the spectra of elementary excitations including the electron-phonon interactions (EPI) in metals and alloys.[1,2] A large number of experiments were carried out on heterojunctions, viz., point contacts made of different metals. The specific nature of heterojunctions led to the discovery of some new effects, such as superposition of the EPI spectra of the metals in contact,[3–5] asymmetry of point-contact (PC) conductivity with respect to the polarity of the applied voltage,[6] and the asymmetry of the EPI spectra.[7] Singularities of the PC spectra of bimetallic contacts revealed in these investigations were explained satisfactorily in theoretical works[8–10] in which nonlinear contributions were calculated in the conductivity of heterojunctions, taking into consideration the processes of electron scattering as well as the kinematics of processes of reabsorption of nonequilibrium phonons. In ''dirty'' contacts with a small mean free path of electrons and phonons (thermal regime of point-contact spectroscopy), the asymmetry of electrical conductivity is attributed[6,9] to the contribution from the Seebeck thermoelectric effect. The asymmetry of PC spectra in contacts with a diffusive motion of quasiparticles is explained by the drag of conduction electrons by the flow of nonequilibrium phonons from the region of current concentration to the bulk electrodes.[7,10]

The recently developed method of high-frequency PC spectroscopy[11,12] makes it possible to study the kinetics of relaxation processes and to single out the contributions to the PC spectra from various mechanisms of quasiparticle scattering in the junction. In this communication, we present the results of experimental investigations of asymmetric effects in heterojunctions carried out by using the high-frequency PC spectroscopy. Measurements were made at 4.2 K on point contacts between copper and an alloy of copper with 1 at. % iron, as well on point contacts between copper and gold. For the Cu–Cu (1 at. % Fe), the bulk electrodes forming the point contact are characterized by practically identical phonon spectra, but have quite different degrees of purity. Electrodes in Cu–Au point contacts were made of metals of identical purity, but having quite different phonon spectra. The copper electrode was in the form of a needle with a radius 1 μm of the tip formed by sharpening electrochemically a copper wire of diameter 0.25 mm with a resistance ratio $R_{300}/R_{4.2}\sim 85$. Measurements of PC spectra were made by using modulation technique involving the recording of the second harmonic of the modulation current in low-frequency experiments and of the rectified voltage amplitude in high-frequency measurements. A detailed description of the measuring technique is given in Ref. 11.

The PC spectra of a Cu–Cu (1 at. % Fe) junction are presented in Fig. 1 for two polarities of the applied bias voltage: the electron flux for $V>0$ is directed from the copper electrode towards Cu(Fe). The spectra were measured at modulation frequencies of 0.21 (curve *1*) and 79.5 GHz (curve *2*). The dependence for the frequency 0.21 GHz fully coincides with the dependence obtained by the conventional low-frequency modulation technique,[1)] and is a correct reproduction of the analogous spectrum for the contact in Ref. 6.

It can be seen from Fig. 1 that the PC spectra of the heterojunction Cu–Cu(Fe) are considerably asymmetric. In addition to a well-defined singularity at low bias voltages caused by scattering of the conduction electrons by the magnetic moments of iron impurity atoms (Kondo effect), the spectra reveal a considerable difference in the height of the phonon lines for $eV\sim\pm 17$ meV, as well as in the level of the background signal for large values of the bias voltage. In order to emphasize this, a part of the spectrum for negative voltages is inverted to the region of positive bias voltages (curve *3*). The asymmetry of the spectrum is enhanced in measurements at a frequency 79.5 GHz. This can be judged from a decrease in the intensity of the phonon singularity at $eV\sim +17$ meV. The curves for 0.21 and 79.5 GHz are specially normalized for $eV\sim -17$ meV and coincide in the region of the Kondo minimum. The justification for such a procedure comes from the fact that in these energy regions the nonlinear contributions to the contact conductivity are associated with rapid processes of electron scattering by phonons and magnetic impurities with characteristic frequencies $(\sim 10^{13}\,\mathrm{s}^{-1})$[11,14] considerably exceeding the current modulation frequency in the experiment. Besides, all measurements were made for extremely weak signals (~ 1 μV), when the amplitude of the signal being measured depends

 © 1998 American Institute of Physics

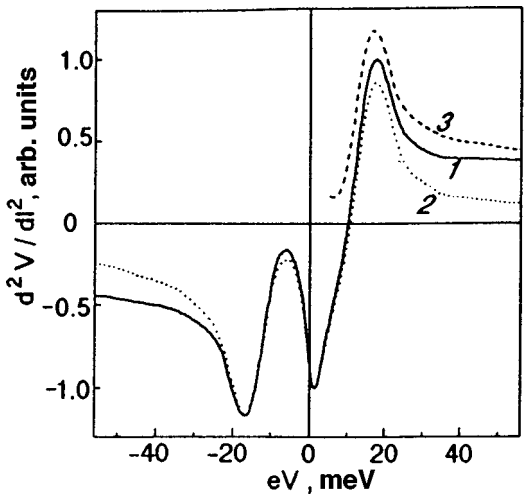

FIG. 1. Spectrum of a Cu–Cu (1 at. % Fe) point contact, measured at a frequency of 0.21 (curve *1*) and 79.5 GHz (curve *2*). Curve *3* describes the part of dependence (1) inverted from the region of negative bias voltages. For $V>0$, electrons are injected into Cu(Fe) alloy.

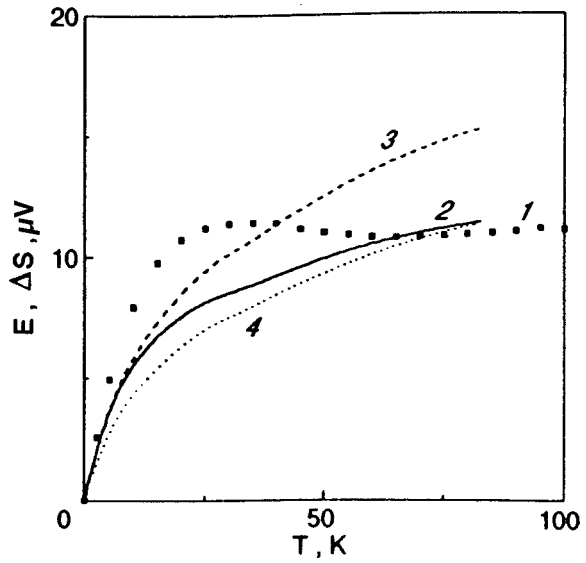

FIG. 2. Temperature dependence of differential thermo-emf of the couple Cu–Cu (1 at. % Fe) (curve *1*) and the values of $\Delta S(T_c)$ calculated by formulas (1) and (2) for different frequencies, GHZ: 0.21 (curve *2*), 79.5 (curve *3*), and corrected data for 79.5 GHz (curve *4*).

linearly on the power of the electromagnetic radiation.

According to the results obtained in Refs. 8, 10, contamination of one of the electrodes in the heterojunction (i.e., a decrease in the elastic mean free path of electrons in this electrode) leads to an identical weakening of intensity of spectral singularities and of the background signal amplitude in both electrodes. However, the results presented in Fig. 1 show that although the ratio of the phonon intensity peak to the background is identical for both polarities of the bias voltage, their absolute values differ significantly. Moreover, the asymmetry of the spectra is observed for both frequencies at which measurements were made. Following Naidyuk *et al.*,[6] it is reasonable to assume that the asymmetry of the PC spectra observed in our experiments is associated with the contribution from the Seebeck thermoelectric effect to the signal being measured. For small elastic and inelastic mean free paths of electrons and phonons in the contact ($l_i, l_e, l_r, l_{\rm ph} \ll d$, where d is the contact diameter), which is typical of the thermal regime of PC spectroscopy, the dependence of the asymmetric part of the differential resistance of a heterojunction on the applied bias voltage is defined by the expression[9,15]

$$R_d^a(V_c) = R_0 \Delta S(T_c) \left[\frac{\rho_1 \rho_2}{(L_1\rho_2 + L_2\rho_1)(\rho_1+\rho_2)} \right]^{1/2}, \qquad (1)$$

where $R_d^a(V) = 1/2[R_d(V^+) - R(V^-)]$, $R_0 \equiv R_d(V=0)$ is the contact resistance, ρ_1 and ρ_2 are the resistivities and L_1 and L_2 the Lorentz numbers for the two constituents of the contact, and ΔS is the differential thermo-emf of the metals in contact. The relation between the contact temperature and the voltage across it is described by the expression

$$T_c = |V_c| \left[\frac{\rho_1 \rho_2}{(L_1\rho_2 + L_2\rho_1)(\rho_1+\rho_2)} \right]^{1/2}. \qquad (2)$$

The quantities in the radicand are the characteristics of metals in the direct vicinity of the contact and hence may differ considerably from analogous parameters for bulk electrodes because of the introduction of structural defects and surface contamination into the volume of the contact during its formation. However, the quantities ρ and L appear in the same proportion in formulas (1) and (2) connecting $R_d^a(V_c)$ with $\Delta S(T_c)$ and V_c with T_c respectively, and hence we can compare the experimental dependences $R_d^a(V_c)$ obtained by us for the asymmetric part of the differential resistance with the temperature dependence $E(T)$ of the differential thermo-emf for the Cu–Cu(Fe) couple, selecting identical scale factor along the vertical and the horizontal axes. The results of such a comparison are presented in Fig. 2. The scale factor for curve *2* was chosen equal to 1.47, so that the values of $\Delta S(T_c)$ calculated by using formula (1) do not exceed the thermo-emf $E(T)$ for the Cu–Cu(Fe) couple.[16,17] The relation between the contact temperature and the voltage across it has the form

$$T_c[\mathrm{K}] = 1.47[\mathrm{K/mV}] V_c[\mathrm{mV}],$$

which is practically identical with the data obtained by Naidyuk *et al.*[6] Curve *3* in Fig. 2, calculated for a modulation frequency of 79.5 GHz for the same value of the scale factor, is slightly higher than the dependence for 0.21 GHz, and the deviation increases with the contact temperature (voltage). Let us analyze the possible reasons behind such a discrepancy. It is well known[16] that the phonon drag thermo-emf is inversely proportional to the phonon–electron relaxation time, i.e., $S_g \propto \tau/(\tau + \tau_{\rm ph-e})$, where τ is the characteristic time of other relaxation processes. Consequently, S_g decreases upon a slowing down of the process of energy transport from phonons to the electron subsystem of the metal. In high-frequency experiments at $\Omega = 79.5$ GHz ($\Omega \tau_{\rm ph-e} \gg 1$),[2)], nonequilibrium phonons do not have time to transfer their excess energy to electrons during a period of the rf field, and the contribution from the drag effect to the thermo-emf must become weaker in contradiction to the data presented in Fig. 2. Apparently, the normalization of the PC

spectra in Fig. 1, which is usually carried out by the high-frequency PC spectroscopy for taking into account the electrodynamic mismatching of the contact with the high-frequency guide at various frequencies,[11] is not quite correct for our experiments. This is due to the fact that in this case the nonlinear contribution to the electrical conductivity of the contact has a frequency-dependent component S_g with a significant frequency dispersion even for small contact voltages. Hence we believe that it would be more realistic to normalize the asymmetric components of differential resistance for different rf modulation frequencies.[3)] Curve *4* in Fig. 2 shows the thermo-emf of the contact calculated by using formula (1), proceeding from the normalized values of the asymmetric part of differential resistance at a frequency 79.5 GHz. It can be seen from the figure that in this case, the dependence $\Delta S(T_c)$ lies below the curve for a frequency 0.21 GHz, which is in complete accord with the above-mentioned expected decrease in the contribution from the drag thermo-emf. The difference in the curves *2* and *4* is of the same order of magnitude as the absolute value of the thermo-emf of phonon drag (e.g., $\sim 1.5\ \mu$V for copper).[16]

Theoretical dependences of $\Delta S(T_c)$ (curves *2* and *4* in Fig. 2) for both frequencies of the rf field differ from the temperature dependence of the thermo-emf of a Cu–Cu(Fe) couple. However, it must be borne in mind that calculations are based on formulas for the thermal regime of PC spectroscopy, while the high-intensity line of the phonon spectrum of copper in the PC spectra of Cu–Cu(Fe) shown in Fig. 1 indicate that the actual regime of the flight of electrons in the contacts under investigation was diffusive. Hence it should be certainly interesting to calculate the kinetics of thermoelectric phenomena in point contacts at high frequencies in order to understand the nature of the ongoing processes and to carry out a more correct comparison of the obtained experimental data with the theory.

The second series of experiments was carried out on Cu–Au heterojunctions formed by metals of identical purity (electrolytic copper and gold were used) but having quite different phonon spectra. Since the contacts were formed uncontrollably as the two bulk electrodes approached each other, individual volumes of copper and gold could differ considerably in the bulk of the contact. This led to a corresponding modification of the overall PC spectrum from a decrease in intensity to a complete disappearance of the spectral lines characterizing one of the electrodes. Hence we carried out our investigations only on those heterojunctions whose PC spectra were a superposition of the spectra of electron–phonon interaction of copper and gold. Figure 3 shows the spectrum of one such contact, measured at different modulation frequencies for two polarities of the applied bias voltage. The observed singularities correspond to the peaks for transverse and longitudinal branches of the phonon spectra of contacting metals whose position is indicated by arrows in the lower part of the figure. It can be seen from Fig. 3 that the intensity of the spectral lines varies considerably upon a reversal of the polarity of the applied bias voltage, but the level of the background signal at high energies does not depend on polarity and remains constant.

The above-mentioned singularities of the PC spectra

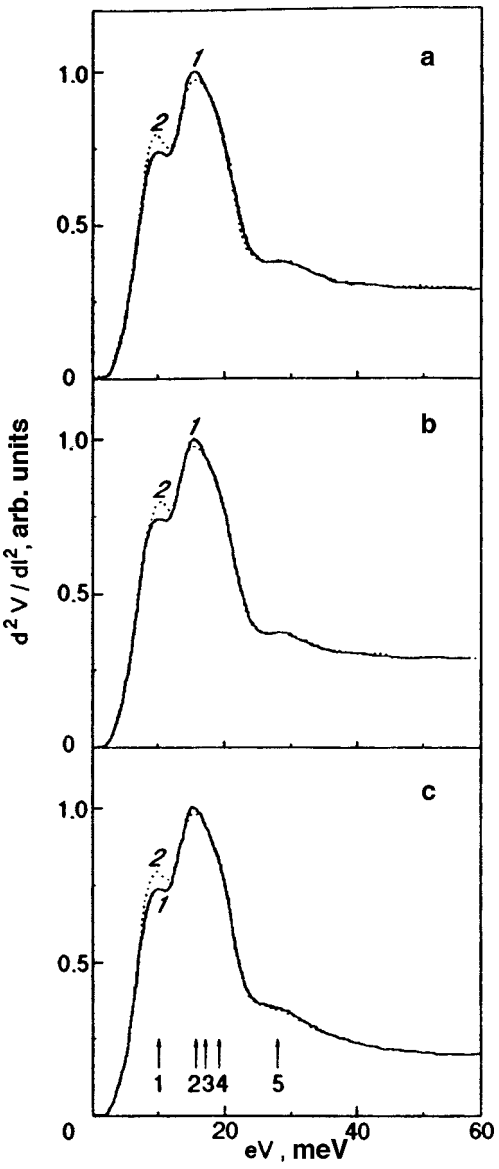

FIG. 3. Spectra of a Cu–Au contact with resistance $R_0 = 3.3\ \Omega$ for different polarities of the applied bias voltage: positive potential at the copper electrode (curve *1*) and the opposite bias polarity (curve *2*). Measurements are made at frequencies 3747 Hz (a), 0.7 (b), and 3.7 GHz (c).

cannot be attributed to the thermoelectric effect considered above for the Cu–Cu(Fe) contacts. Since the spectra of the Cu–Au point contact shown in Fig. 3 do not display any enhancement of asymmetry upon an increase in bias voltage (as in the case of Cu–Cu(Fe) contact shown in Fig. 1), and since the values of the absolute thermo-emf for copper and gold are identical,[16] the thermoelectric contribution to the nonlinearity of the current-voltage characteristics must be negligible.

The asymmetry of the PC spectra of Cu–Au heterojunctions, which is analogous to the one shown in Fig. 3, was first investigated experimentally by Naidyuk and Yanson[7] who interpreted their experimental results by using the theoretical computations of the drift of electrons dragged by nonequilibrium phonons.[9,10] According to Itskovich and Shekhter,[10] the diffusion drag of nonequilibrium phonons from the bulk of the contact to massive banks in the case of

a strong elastic scattering of phonons in the contact ($l_r \ll d$) accelerates the electron flow in one conductor and retards it in the other. For a bimetallic contact, the phonon drag of electrons in normal processes of electron-phonon scattering leads to a decrease in the intensity of the PC spectrum of the metal into which electrons are injected, and increases the amplitude of the spectral line of the other conductor. If the electron-phonon umklapp scattering processes dominate in a metal as in the case of scattering by transverse acoustic phonons in copper and gold, the sign of asymmetry is reversed. The degree of asymmetry, i.e., the ratio of the asymmetric and symmetric parts of the spectrum, is proportional to the ratio l_r/d. The drift drag does not affect the background in the PC spectrum whose level must be preserved for both polarities of the bias voltage applied to the contact.[10]

The data presented by us in Fig. 3a are in good agreement with the results obtained by Naidyuk and Yanson[7] and completely fit into the theoretical concepts presented in Ref. 10. Indeed, it follows from Fig. 3a that injection of electrons to the copper electrodes increases the intensity of the peak of transverse phonons line for copper ($eV \sim 17$ meV). For the opposite polarity (injection into the gold electrode), the intensity of transverse phonons line for gold increases ($eV \sim 10$ meV), the background level remaining the same for both curves. Using the values of the characteristic parameters (ρl) for copper and gold[19] from the formula $R_0 = 8[(\rho l)_1 + (\rho l)_2]/3\pi d^2$, we can determine the contact diameter ($d \sim 20$ nm). The difference in the spectra shown in Fig. 3a can be used to estimate the elastic mean free path of phonons in the contact. The obtained values $l_r \sim 1-2$ nm coincide with the earlier estimates.[7,11] An increase in the current modulation frequency to 0.7 GHz, close to the frequency of thermal relaxation of the contact, did not lead to any change in the PC spectrum (see Fig. 3b). In experiments at a frequency of 3.7 GHz (Fig. 3c), comparable with the characteristic phonon–electron relaxation frequencies[11] in gold ($\tau_{\mathrm{ph}-e}^{-1} = 2$ GHz)) and in copper ($\tau_{\mathrm{ph}-e}^{-1} = 5$ GHz)), the spectral asymmetry was preserved but, as expected, the background level decreased considerably due to a decrease in the contribution to the spectrum coming from reabsorption of nonequilibrium phonons at high frequencies.[11]

In order to interpret the results of rf measurements, we use the expression for the PC spectrum of a heterojunction from Ref. 10:

$$\frac{d^2V}{dI^2}(|eV|) \sim \sum_{n=1}^{2} \frac{d_n}{v_{F_n}} \left[g_n^{(1)}(|eV|) + Q_n(|eV|) g_n^{(2)} \times (|eV|) + 2\int_0^{|eV|} Q_n(\omega) g_n^{(2)}(\omega) \frac{d\omega}{\omega} + (-1)^n \operatorname{sgn}(eV) g_n^2(|eV|) \right]. \quad (3)$$

Here v_F is the Fermi velocity, and summation over n takes into account the partial contributions of metals. The functions $g^{(i)}(eV)$ $(i=1,2)$ describe the EPI spectrum for the processes of spontaneous and stimulated emission of phonons. They differ only in the magnitude of the geometrical K-factor which is more weakly directional for $g^{(2)}$. The coefficient $Q(\omega)$ is defined by the kinetics of nonequilibrium phonons in the contact and for a complete phonon reabsorption, its value is equal to about 0.3 at the Debye energies for the model of the contact in the form of a long channel.[18] The first term in formula (3) is the PC spectrum of the EPI, the second corresponds to the renormalization of this spectrum caused by the interaction of electrons with the nonequilibrium phonons, the third to the background in the spectrum for high energies, and the fourth term determines the asymmetry of the spectrum for different directions of the current through the contact.

If the current modulation frequency is quite high ($\Omega \tau_{\mathrm{ph}-e} > 1$), the correspondence between the number of nonequilibrium phonons and the instantaneous value of the alternating voltage across the contact is violated. The number of acts of reabsorption of phonons occurring synchronously with a change in voltage is reduced, and the amplitude of the background part of the spectrum decreases. The remaining components of the spectrum (3) are characterized by the electron–phonon scattering time ($\tau_{e-\mathrm{ph}} \ll \tau_{\mathrm{ph}-e}$, $\Omega \tau_{e-\mathrm{ph}} \ll 1$), hence their magnitude must remain unchanged in the investigated frequency range. The experimental results presented in Fig. 3 are confirmed by the mechanism of modification of the PC spectrum at high frequencies considered above.

Thus, we have observed in this work the effect of the electromagnetic radiation frequency on the asymmetry of the current–voltage characteristics of different types of heterojunctions, which is associated with the specific features of the relaxation of nonequilibrium phonons. The obtained results considerably supplement the results of previous investigations.[6,7] In conclusion, it should be remarked that theoretical computations of the asymmetric effects in bimetallic contacts at high frequencies and their comparison with the experimental results presented here are undoubtedly of considerable interest.

The author is indebted to I. K. Yanson for his continued attention and support in the course of this research, and to A. G. Shkorbatov for fruitful discussions.

*E-mail: balkashin@ilt.kharkov.ua

[1)] This is an expected result since the modulation frequency of 0.21 GHz is much lower than the characteristic frequency of slowest relaxation process in the contact, viz., the relaxation of temperature with a characteristic frequency $f_T \sim 1$ GHz.[13]

[2)] The characteristic phonon relaxation time in copper with Debye energies is $\tau_{\mathrm{ph}-e} \sim 2 \times 10^{-10}$ s, while the opposite inequality holds for the frequency 0.21 GHz.

[3)] The theoretical values of ΔS on curve *3* cannot be reduced simply by magnifying the scale of the coefficient, since this would lead to a considerable increase in the contact temperature in rf measurements for the same values of the d.c. bias voltage, which contradicts the experimental results[11] indicating a decrease in contact heating upon rf modulation.

[1] I. K. Yanson and A. V. Khotkevich, *Atlas of Point-Contact Spectra and Electron-Phonon Interaction in Metals* [in Russian], Naukova Dumka, Kiev (1986).
[2] I. K. Yanson and O. I. Shklyarevskii, Fiz. Nizk. Temp. **12**, 899 (1986) [Sov. J. Low Temp. Phys. **12**, 509 (1986)].
[3] A. G. M. Jansen, A. P. van Gelder, and P. Wyder, J. Phys. C **13**, 6073 (1980).

[4] A. G. Batrak and I. K. Yanson, Fiz. Nizk. Temp. **5**, 1404 (1979) [Sov. J. Low Temp. Phys. **5**, 663 (1979)].
[5] H. Sato, K. Yonemitsu, and J. Bass, Phys. Rev. **35**, 2484 (1987).
[6] Yu. G. Naidyuk, N. N. Gribov, O. I. Shklyarevskii *et al.*, Fiz. Nizk. Temp. **11**, 1053 (1985) [Sov. J. Low Temp. Phys. **11**, 580 (1985)].
[7] Yu. G. Naidyuk and I. K. Yanson, Fiz. Tverd. Tela (Leningrad) **30**, 1535 (1988) [Sov. Phys. Solid State **30**, 888 (1988)].
[8] R. I. Shekhter and I. O. Kulik, Fiz. Nizk. Temp. **9**, 46 (1983) [Sov. J. Low Temp. Phys. **9**, 22 (1983)].
[9] I. F. Itskovich, I. O. Kulik, and R. I. Shekhter, Fiz. Nizk. Temp. **11**, 886 (1985) [Sov. J. Low Temp. Phys. **11**, 488 (1985)].
[10] I. F. Itskovich and R. I. Shekhter, Fiz. Nizk. Temp. **11**, 1176 (1985) [Sov. J. Low Temp. Phys. **11**, 649 (1985)].
[11] O. P. Balkashin, I. K. Yanson, and Yu. A. Pilipenko, Fiz. Nizk. Temp. **13**, 389 (1987) [Sov. J. Low Temp. Phys. **13**, 222 (1987)].
[12] O. P. Balkashin, Fiz. Nizk. Temp. **18**, 659 (1992) [Sov. J. Low Temp. Phys. **18**, 470 (1992)].
[13] O. P. Balkashin, I. K. Yanson, V. S. Solov'ev, and A. Yu. Krasnogorov, Zh. Tekh. Fiz. **52**, 811 (1982) [Sov. Phys. Tech. Phys. **27**, 522 (1982)].
[14] M. A. Blachly and N. Giordano, Phys. Rev. **51**, 12 537 (1995).
[15] Yu. Naidyuk, M. Reiffers, A. N. Omelyanchouk *et al.*, Physica B **194–196**, 1321 (1994).
[16] F. J. Blatt, P. A. Schroeder, C. L. Foils, and D. Greig, *Thermoelectric Power of Metals*, Plenum Press, N.Y. (1976).
[17] V. M. Beilin, I. Ya. Levin, I. L. Rogel'berg, and V. A. Cherenkov, Fiz. Met. Metalloved. **42**, 288 (1976).
[18] I. O. Kulik, Fiz. Nizk. Temp. **11**, 937 (1985) [Sov. J. Low Temp. Phys. **11**, 516 (1985)].
[19] I. K. Yanson, Fiz. Nizk. Temp. **9**, 676 (1983) [Sov. J. Low Temp. Phys. **9**, 343 (1983)].

Translated by R. S. Wadhwa

Anomalous skin effect in magnetic field: dependence on the shape of the Fermi surface

L. T. Tsymbal, A. N. Cherkasov, and O. F. Panchenko

*A. Galkin Institute of Physics and Technology, National Academy of Sciences of the Ukraine, 340114 Donetsk, Ukraine**

(Submitted July 16, 1998)
Fiz. Nizk. Temp. **24**, 1157–1165 (December 1998)

A non-traditional point of view to the nature of anomalous skin effect is proposed on the basis of an analysis of the problem of coupling modes in the electron plasma of a metal. It is shown that the anomalous skin effect in an applied magnetic field is in fact the result of interaction and coupling of a number of intrinsic electromagnetic modes excited due to nonlocal effects and specific properties of doppleron modes. It is proved that the magnetic field dependence of anomalous skin effect is determined by the shape of the Fermi surface of the metal and that the classical anomalous skin effect in the model of free electrons is just a special case. © *1998 American Institute of Physics.* [S1063-777X(98)00512-X]

Dedicated to I. M. Dmitrenko and A. M. Kosevich, pioneers in electron physics of metals, ''who, consuming midnight oil in studies diligent and slow, teach themselves, with painful toil, the things that other people know'' (*from Piet Hein*)

INTRODUCTION

Skin effect is closely related to the problem of excitation and propagation of electromagnetic waves in conducting media and is one of classical effects in the electrodynamics of metals. In relatively ''dirty'' metals, the so-called normal skin effect takes place, and the wave vector $k_{\rm ns}$ of the electromagnetic wave obeys the relation $k_{\rm ns}\propto(i\omega/\nu)^{1/2}$. In pure metals at low temperatures, the interaction between the current and the electric field becomes nonlocal, and the skin effect becomes anomalous.[1–3] The wave vector $k_{\rm as}\propto(i\omega)^{1/3}$ and is independent of the electron relaxation frequency ν, which points to a collisionless mechanism of attenuation of waves. Here ω is the frequency of an electromagnetic wave. The developed theoretical methods were naturally extended to metals in an external magnetic field $\mathbf{H}$.[4–6] It was proved that the presence of the magnetic field weakly affects the anomalous skin effect in a certain region of fields and frequencies.

At first sight, anomalous skin effect has been studied extensively by the present time. Nevertheless, it is expedient to carry out a detailed analysis of this phenomenon once again, especially anomalous skin effect in an external magnetic field. The present paper is devoted to such an analysis. Our attention will be concentrated on the following two aspects of the problem.

(1) The anomalous skin effect exists due to nonlocal effects in the conductivity of a metal. Consequently, certain preferred groups of charge carriers on the Fermi surface (FS) take part in the formation of skin components. As a result, the solution of the dispersion equation is determined to a considerable extent by peculiarities of the electron energy spectrum and hence is ''model-dependent.'' Along with the conventional model of free electrons, we consider here some simple, but typical and quite realistic models of the FS and prove that the magnetic field dependence of skin effect is determined to a considerable extent by the properties of real FS. The ''classical'' anomalous skin effect (for a spherical FS) is generally a special case of the phenomenon.

(2) In strong magnetic fields, the solutions of the dispersion equation describe the spectrum and attenuation of electromagnetic waves forming a system of coupled modes. In certain ranges of extrinsic parameters, these modes possess typical features determining (together with historical reasons) their names. We prove that anomalous skin effect in an external magnetic field can be interpreted as the result of coupling of these electromagnetic modes (Gelicons and dopplerons in the given case). The existence of the doppleron mode and its hybridization with a *g*elicon are associated with nonlocal effects and specific properties of dopplerons distinguishing them from the series of collective excitations of other types.

We confine our analysis to the spectra of electromagnetic modes in an infinite translation-invariant medium in the geometry $\mathbf{k}\|\mathbf{H}\|\hat{z}$. We assume that the FS of the metal possesses rotational symmetry relative to the $\hat{z}$-axis. The dispersion equation for the circularly polarized field components $(E_\pm=E_x\pm iE_y)$ in this case has the form

$$k^2c^2=4\pi i\omega\sigma_\pm(k), \quad (\pm\text{polarization}), \tag{1}$$

where $\sigma_\pm=\sigma_{xx}\pm i\sigma_{yx}$ is the conductivity defined by the integral over the Fermi surface:

$$\sigma_\pm(k)=i\,\frac{2\pi e^2}{(2\pi\hbar)^3}\int_{FS}\frac{|m|v_\perp^2\,dp_z}{\omega+i\nu\pm\omega_c-kv_z}. \tag{2}$$

Here v_z and p_z are the z-components of the electron velocity and momentum, $v_\perp$ is the electron velocity component perpendicular to the $\hat{z}$-axis, and $\omega_c=eH/mc$ is the cyclotron frequency.

We shall describe the shape of the FS by the functional dependence $S(p_z)=\pi(mv_\perp)^2$, where $S(p_z)$ is the area of the

 © 1998 American Institute of Physics

section of the FS by the plane $p_z=\text{const}$. We write Eqs. (1) and (2) using the relation $v_z=-(\partial S/\partial p_z)/2\pi m$ and introducing the dimensionless parameters

$$q=\frac{kv_m}{\omega_c},\quad \xi^3=\frac{\omega_c^3c^2}{\omega_p^2\omega v_m^2},\quad \gamma=\frac{\nu-i\omega}{\omega_c} \tag{3}$$

in the form

$$\mp q^2\xi^3=F_\pm(q),\quad (\pm\text{polarization}), \tag{4}$$

$$F_\pm(q)=\frac{2\ \text{sgn}(m)}{N(2\pi\hbar)^3}\int_{FS}\frac{S(p_z)dp_z}{1\pm i\gamma\pm q(\partial S/\partial p_z)/|\partial S/\partial p_z|_m}. \tag{5}$$

In Eqs. (3)–(5), $v_m=|\partial S/\partial p_z|_m/2\pi m;|\partial S/\partial p_z|_m$ is a certain typical value of the derivative $\partial S/\partial p_z$ (maximum value in the present case), $\omega_p=(4\pi Ne^2/m)^{1/2}$ the plasma frequency, $F_\pm(q)$ a nonlocal factor in the conductivity ($\sigma_\pm=\pm i(Nec/H)F_\pm$), sgn($m$) the sign of the cyclotron mass, and N the carrier concentration defined as

$$N=\frac{2}{(2\pi\hbar)^3}\int_{FS}S(p_z)dp_z. \tag{6}$$

In this paper, we do not consider the excitation of electromagnetic waves in a metal and the complicated boundary problem associated with it and confine ourselves to an analysis of solutions of the dispersion equation (which was solved numerically). The zeros of the analytically defined function $f=\mp q^2\xi^3-F_\pm$ were determined by the Muller method (generalized method of secants) with deflation.[7] The nature of the roots of the dispersion equation was also determined by using the graphic method of the solution of the equation.

MODELS OF FERMI SURFACE: CONDUCTIVITY OF METAL

The existence of the FS is associated with the Fermi degeneracy of conduction electrons in metals. An important property of real FS is the existence of extremal cross section $S(p_m)=S_m(\partial S/\partial p_z=0)$ and cross sections with extremal values of the derivative $\partial S/\partial p_z$. We consider here the models of FS for which the quantity $|\partial S/\partial p_z|$ as a function of p_z varies continuously from zero to a certain value $|\partial S/\partial p_z|_m$. Naturally, we choose simple models to simplify the derivation of an analytic expression for conductivity and the numerical solution of the dispersion equation.

In the region of relatively low frequencies and strong fields we are interested in, which is defined by the inequalities

$$\omega\ll\nu\ll\omega_c, \tag{7}$$

collisions can be neglected. Consequently, we calculate the function $F_\pm$ (5) in the limit $\gamma\to0(F_\pm|_{\gamma=0}=F_0)$.

Let us consider several FS models, assuming for the sake of definiteness that all the surfaces are of the electron type. Three of them will be described by the even function

$$S(p_z)=\pi p_0^2(1-|x|^n),\quad |x|\leqslant1. \tag{8}$$

Here and below, $x=p_z/p_0$. Model $A(n=2)$ is the basic model and is the well-studied model of free electrons. Two other models, viz., model $B(n=3)$ and model $C(n=3/2)$ are proposed to determine the effect of distortions of a spherical

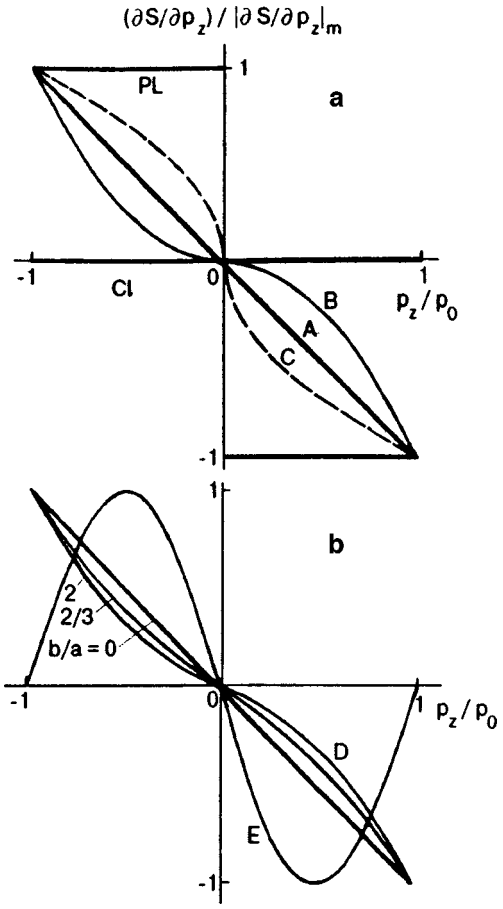

FIG. 1. Dependence of the normalized derivative $(\partial S/\partial p_z)/|\partial S/\partial p_z|_m$ on p_z/p_0 for models *A*, *B*, and *C* [see Eq. (8)] as well as the ''parabolic lens'' (PL) model and the cylindrical FS (along the $\hat{z}$-axis (Cl) (a) and the same for models *D* and *E* (see (12) and (13)) (b).

FS, which is described by an increase or a decrease in the value of the parameter n relative to the value $n=2$ on the solutions of the dispersion equation. The function F_0 for these three models has the form

$$F_0^A=\frac{3}{4q^2}\left[\left(1-\frac{1}{q^2}\right)\ln\frac{1+q}{1-q}+\frac{2}{q}\right], \tag{9}$$

$$F_0^B=\frac{1}{3}\left[\frac{1}{q^{1/2}}\ln\frac{1+q^{1/2}}{1-q^{1/2}}+\frac{1}{q^2}\ln(1-q^2)+\frac{2}{q^{1/2}}\arctan(q^{1/2})\right], \tag{10}$$

$$F_0^C=\frac{5}{3q^2}\left[\left(\frac{1}{q^3}-1\right)\ln(1-q)-\left(\frac{1}{q^3}+1\right)\ln(1+q)+\frac{2}{q^2}+\frac{2}{3}\right]. \tag{11}$$

The curves describing the functions $\partial S/\partial p_z$ and F_0 are shown in Fig. 1a and in the inset to Fig. 2 respectively.

The fourth model (*D*) described by the expression

$$S(p_z)=\pi p_0^2(1-ax^2-b|x|^3),\quad |x|\leqslant1, \tag{12}$$

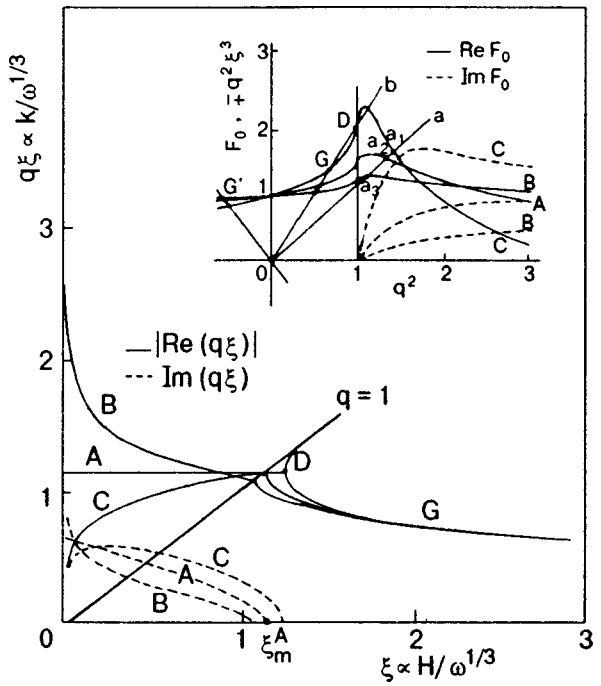

FIG. 2. Spectrum of electromagnetic modes in the ''−'' polarization for models *A*, *B*, and *C* (numerical solution of Eq. (4) with conductivity (9), (10), and (11) respectively). The inset illustrates graphical solution of Eq. (4) for models *A*, *B*, and *C*. The curves describe the functions F_0^A, F_0^B, and F_0^C. Straight lines a and b describe the left-hand side of Eq. (4) in the ''−'' polarization for successively large values of ξ, *c* is the left-hand side of Eq. (4) in the ''+'' polarization; *G* and *D* are the gelicon and doppleron solutions respectively, and G' is a damped gelicon.

is a ''hybrid'' of models *A* and *B*.[12] In this equation, $a+b=1$, $a>0$, and $b>0$. We do not write here the expression for F_0^D since it is very cumbersome. The curves describing the function $\partial S/\partial p_z$ in model *D* for various values of the parameter b/a are shown in Fig. 1b.

The function $\partial S/\partial p_z$ in models $A-D$ has extrema at the points $p_z=\pm p_0$, at which $S(p_z)=0$ and $\partial^2 S/\partial p_z^2 \neq 0$. Consequently, the functions F_0^{A-D} are finite for $q^2=1$ even in the collisionless limit, although the denominator in the integrand in (5) vanishes at these points for $q^2=1$ (singularity of the ''weak logarithm'' type; see the ''hierarchy'' of singularities in Ref. 8). For this reason, we consider for comparison one more model (*E*) of the ''corrugated cylinder'' type:[8]

$$S(p_z)=S_0+S_1\cos(\pi x), \quad |x|\leqslant 1. \tag{13}$$

Here S_0, $S_1<S_0$, and p_0 are the model parameters. The curve describing the function $\partial S/\partial p_z$ is presented in Fig. 1b. In this model, the expression for F_0, i.e.,

$$F_0^E=(1-q^2)^{-1/2} \tag{14}$$

has a root singularity for $q^2=1$ (cf. insets to Figs. 2 and 4).

ANALYSIS OF SPECTRA OF ELECTROMAGNETIC MODES

We present numerical solutions of the dispersion equation graphically in the coordinates $q\xi \propto k/\omega^{1/3}$, $\xi \propto H/\omega^{1/3}$. In the limit $\gamma \to 0$, these coordinates are universal since the obtained dependences describe uniquely the spectrum of electromagnetic modes for any values of the extrinsic parameters ω and H.[9]

1. Figure 2 shows the spectra of electromagnetic modes in the ''−'' polarization for models *A*, *B*, and *C*. The graphic solution of the dispersion equations (see inset to Fig. 2) shows that one of the spectral branches corresponds to a purely real gelicon (*G*) solution of the dispersion equation in the ''−'' polarization for all values of ξ larger than certain threshold values ξ_m. Besides, one more (doppleron) solution (*D*) of this equation exists in a relatively narrow range of ξ. For $q^2>1$, the functions F_0 become complex-valued due to collisionless damping of electromagnetic waves associated with the Doppler-shifted cyclotron resonance (DSCR). The formal condition for the DSCR is the vanishing of the denominator of the integrand in (2) and (5). Consequently, points a_i are not solutions of the dispersion equation, and solutions also become complex-valued for $\xi<\xi_m$. In the ''+'' polarization the unique solution (G') existing for all model is a damped gelicon. These solutions are not shown in Fig. 2 to simplify the figure.

The solution of the dispersion equation in model *A* for $\xi \to 0 (H \to 0, \omega = \text{const})$ coincides with the well-known solution $q\xi=(3\pi i/4)^{1/3}$ which was obtained earlier in zero magnetic field. It is natural to assume that all the solutions obtained by us for $\xi<\xi_m$ describe anomalous skin effect in an external magnetic field. There are two such solutions for each model in the ''−'' polarization, which differ only in the sign of the phase velocity of the wave, i.e., the sign of the quantity $\mathrm{Re}(q\xi)$.

It can be seen from Fig. 2 that the value of $\mathrm{Re}(q\xi)$ for model *A* is virtually independent of ξ up to the gelicon threshold, while $\mathrm{Im}(q\xi)$ decreases monotonically to zero with increasing ξ. Hence the impedance of alkali metals depends weakly on *H* for $\xi<\xi_m$.[5] In the region of small ξ, we have $|q^2| \gg 1$, and hence the solution of the dispersion equation is determined by the asymptotic form of the function F_0^A in the essentially nonlocal limit $q^2 \gg 1$: $F_0 \to \mp 3\pi i/4q + 3/q^2$. The second term can be neglected, and we obtain from (4) the following well-known expression:

$$k=\left(\frac{3\pi i}{4}\frac{\omega_p^2\omega}{c^2 v_m}\right)^{1/3}. \tag{15}$$

We shall call the anomalous skin effect defined by the asymptotic form $F_0 \propto i/q (\gamma \to 0)$ the ''classical'' anomalous skin effect.

For $q^2<1$ in the limit $\gamma \to 0$, F_0 is obviously a pure real-valued function. For $q^2>1$, FS cross sections appear for which the denominator in the integrand in (2) and (5) vanishes, i.e., electrons emerge for which the DSCR condition

$$\frac{\partial S/\partial p_z}{|\partial S/\partial p_z|_m}=\pm\frac{1}{q}, \tag{16}$$

is observed. As a result, the dissipative component of conductivity becomes nonzero for $q^2>1$. It can be seen from (16) that for $q^2 \gg 1$, ''resonant'' cross sections $S_r(p_z=p_{zr})$ are localized near extremal cross sections S_m of the FS (see, for example, Fig. 1). Consequently, the asymptotic form of

$\mathrm{Im}(F_0)$ for large values of q^2 is determined by the behavior of the function $S(p_z)$ and its derivatives in the vicinity of these cross sections. Using the expansion of the function $S(p_z)$ at the point p_{zr} defined by formula (16), we can easily derive from (5) the following expression for the function $\mathrm{Im}(F_0)$:

$$\mathrm{Im}(F_0)=\mp\frac{\pi i}{q}\left|\frac{SS_m^{(1)}}{VS^{(2)}}\right|_{p_z=p_{zr}}. \tag{17}$$

Here $S^{(i)}=\partial^i S/\partial p_z^i$ and V is the volume occupied by electrons. It can be seen from (17) that the asymptotic form of the function $\mathrm{Im}(F_0^A)$ in the model of free electrons (model *A*) is determined by the fact that the second derivative $S^{(2)}=\mathrm{const}$, and $S_r\approx S_m$ in the limit $q^2\gg 1$.

Using (8), we can write (17) in the form

$$\mathrm{Im}(F_0)=\mp\frac{\pi i}{q^{1/(n-1)}}\frac{S_r}{S_m}\frac{n+1}{2n(n-1)}. \tag{18}$$

It can be seen that the anomalous skin effect is classical only for $n=2$: $\mathrm{Im}(F_0^A)=\mp 3\pi i/4q$ in the limit $q^2\gg 1$. For example, we have $\mathrm{Im}(F_0^B)=\mp\pi i/3q^{1/2}$ for model *B* and $\mathrm{Im}(F_0^C)=\mp 5\pi i/3q^2$ for model *C*. Consequently, the spectra of electromagnetic modes for models *A*, *B* and *C* in the region of small ξ differ significantly. Naturally, it should be borne in mind that the form of the spectra is also determined by the asymptotic form of the function $\mathrm{Re}(F_0)$ since $|\mathrm{Im}(F_0^A)|\gg\mathrm{Re}(F_0^A)$ only for model *A*. On the other hand, $|\mathrm{Im}(F_0^B)|=\mathrm{Re}(F_0^B)$ for model *B* and $|\mathrm{Im}(F_0^C)|\ll\mathrm{Re}(F_0^C)$ for model *C*, where $\mathrm{Re}(F_0^C)<0$. It can be seen from Fig. 2 that the spectra of electromagnetic modes for models *A*, *B*, and *C* differ radically in the region of anomalous skin effect. In contrast to model *A*, both imaginary and real components of $q\xi$ increase indefinitely for $\xi\to 0$ in model *B* and tend to zero in model *C*. Such a qualitatively definite form of the spectra is preserved for any $n>2$ and $n<2$ respectively. This is associated with the asymptotic form of the second derivative $S^{(2)}$ for $p_z\to 0$ ($p_{zr}\to 0$ for $\xi\to 0$) since its magnitude is inversely proportional to the number of resonant (effective)[1] electrons participating in the formation of spin component of the field. For models described by formula (8), $S^{(2)}\to 0$ for $n>2$ and $S^{(2)}\to\infty$ for $n<2$. It should be noted, however, that electron relaxation must be taken into account for $\xi\to 0$. For this reason, the values of $\mathrm{Re}(q\xi)$ and $\mathrm{Im}(q\xi)$ for $\xi=0$ are equal to their values for $\xi=\xi|_{\omega_c=\nu}$. It should also be noted that in the two limiting cases ($n\to\infty$ and $n\to 1$), formula (8) describes two more characteristic FS models. In the first limit, we go over to a cylindrical (relative to the $\hat{z}$-axis) FS for which $F_0=1$, since $v_z=0$ for all electrons, and nonlocal effects are absent. As a result, the dispersion equation has only two solutions: *G* and *G′* (see the straight line and curve *L* in Fig. 4). In the other limit, we have the model of ''parabolic lens''[10] for which $\partial S/\partial p_z=\mathrm{const}$ and $\mathrm{Im}(F_0)=0$($F_0=(1-q^2)^{-1}$) since the DSCR condition is satisfied only for $q^2=1$. Nevertheless, the dispersion equation for this model has solutions describing anomalous skin effect. The spectrum of electromagnetic waves corresponding to these solutions is qualitatively similar to the spectrum for model *C*.

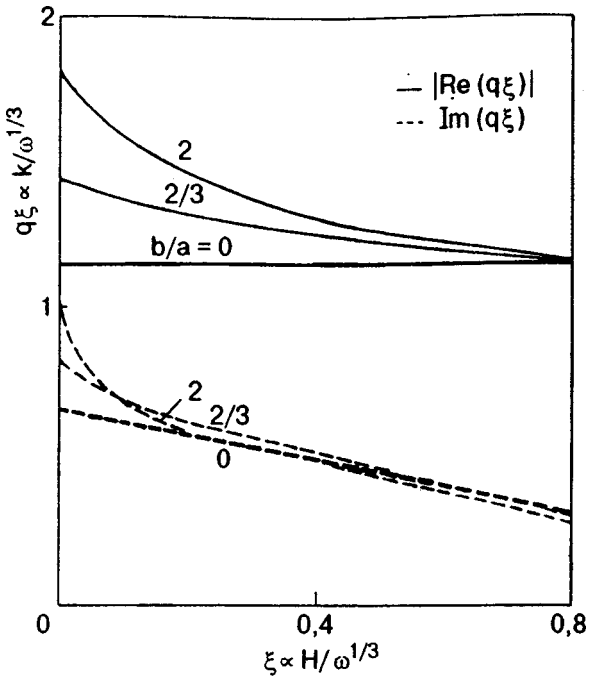

FIG. 3. The spectrum of electromagnetic modes for model *D* in the ''+'' polarization. For $b/a=0$, model *D* coincides with model *A* (see Eqs. (8), (12), and Fig. 1).

2. Let us now analyze an important aspect of the problem under investigation, associated with the correctness of the choice of the FS model. In view of the presence of an inversion center, $S(p_z)$ is an even function of p_z. We assume that $p_z=0$ at the inversion center. If the function $S(p_z)$ is analytic at this point, it can be presented in the form of an expansion only in even powers of p_z:

$$S(p_z)=a_0+a_1p_z^2+a_2p_z^4+\dots . \tag{19}$$

In this connection, a very important question arises: must the function $S(p_z)$ be analytic since the function (8) is not analytic at the point $p_z=0$ for $n=3$ and $n=3/2$? We cannot give an answer to this complicated question here and confine ourselves only to an analysis of analytic functions $S(p_z)$. The function (8) for $n=4$ is such a function. In this case, however, the expression for F_0 was found to be so complicated that we could not obtain a numerical solution of the dispersion equation. It was proved above, however, that model *B* provides a correct qualitative description for the spectrum of electromagnetic modes for $n=4$ also. An insignificant quantitative difference is for example, that for small ξ and $n=4$, the curve lies above the corresponding curve obtained for model *B*. This is due to a continuous transition to a cylindrical FS for $n\to\infty$. Model (8) of a FS with $n=4$ obviously describes a specific particular case. For this reason, we consider a more realistic model, retaining the first three terms in expansion (19) and assuming that the next terms are negligibly small for small values of p_z. In this case, however, we cannot obtain an analytic expression for the function F_0. This model can obviously be approximated qualitatively by model *D* (12) which is a ''hybrid'' of models *A* and *B*. For $b/a=0$, model *D* coincides with *A*, while for $b/a\to\infty$ we go over to model *B*. Figure 3 shows the

spectra of electromagnetic modes in the ''−'' polarization for model *D*, which were obtained for different values of the parameter b/a. It can be seen that the solutions of the dispersion equation become functions of the quantity ξ for small ξ even for relatively small values of b/a. As a result, the anomalous skin effect described by these solutions is not ''classical'' any longer.

3. It was noted above that the type of anomalous skin effect for small ξ in the model of free electrons (model *A*) is determined by the asymptotic form of the dissipative component of conductivity for $q^2 \gg 1$ since $\mathrm{Im}(F_0) \gg \mathrm{Re}(F_0)$ in this model for large q^2. Consequently, it is natural to assume that anomalous skin effect for the model of free electrons is associated with collisionless absorption of electromagnetic waves due to DSCR. It was noted above, however, that $|\mathrm{Re}(F_0)| \gg \mathrm{Im}(F_0)$ for $q^2 \gg 1$ in the case of large n and $n \sim 1$. However, complex solutions of the dispersion equation exists for these models also, which describe the skin effect that is anomalous but not ''classical'' by nature. We do not consider here the correctness of application of such models. It is important for us that solutions indicating that the skin effect in a magnetic field may not be due to collisionless damping of electromagnetic waves exist in principle. This fact is illustrated by solutions of the dispersion equation for the PL model. For this reason, we analyze the spectrum of electromagnetic modes from a nontraditional point of view. Without any loss of generality, we use model *E* (13) for this purpose.

Figure 4 shows the spectrum of electromagnetic modes for model *E*. It can be seen that in contrast to models *A*–*C*, the doppleron solution (*D*) is purely real-valued for all $\xi > \xi_m$. This is due to the fact that the singularity in conductivity (14) in model *E* is of the root type (cf. the graphic solution of the dispersion equation in Figs. 2 and 4). The simplicity of expression (14) for the function F_0^E allows us to write the dispersion equation in the form

$$(q^2 - q_{G_L}^2)(q^2 - q_{G_L'}^2)(q^2 - q_D^2) = -q^2/\xi^6, \tag{20}$$

where $q^2 = 1$ is the equation of the straight line corresponding to the edge of collisionless damping of waves due to DSCR in Fig. 4, and $q_{G_L}^2 = q_{G_L'}^2 = \xi^{-3}$ are solutions of Eq. (4) in the local limit (curve *L* in Fig. 4). It can be seen that the dispersion equation written in such a form can be regarded as the equation of three coupled modes. Two of them can be naturally identified as the gelicon and the damped gelicon modes, while the third can be called the DSCR mode, or doppleron. It can be seen from Eq. (20) and Fig. 4 that coupling of modes can be neglected for relatively large values of ξ far away from the point of mode degeneracy ($\xi = 1$). As the value of ξ decreases, the *G*- and *D*-branches of the spectrum converge and are coupled (to be more precise, hybridized) for $\xi = \xi_m (\xi_m = (27/4)^{1/6})$. As a result, the solutions of the dispersion equation in the ''−'' polarization become complex-valued in the range $\xi < \xi_m$, i.e., a ''nontransparency'' region or ''gap'' is formed. It is important to note that the point of mode coupling lies below the straight line $q^2 = 1 : q_{G,D}^2 = 2/3$ for $\xi = \xi_m$. Consequently, there are no

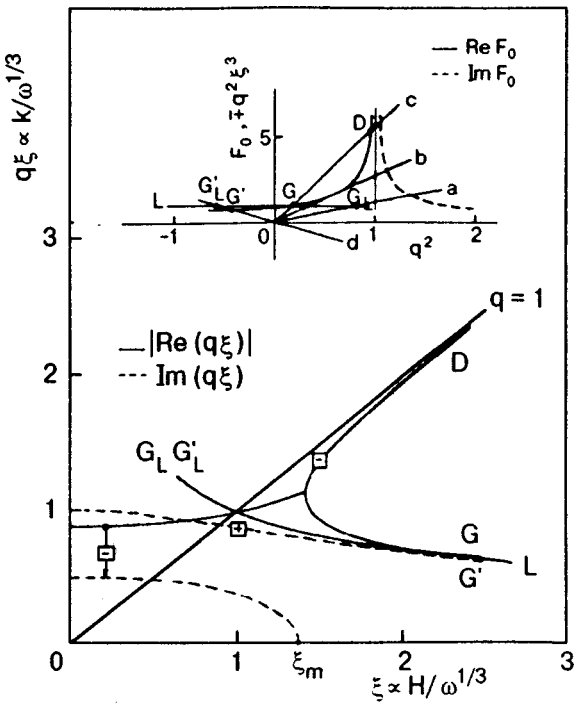

FIG. 4. Spectrum of electromagnetic modes for model *E* (numerical solution of Eq. (4) with conductivity (14)). The symbols of circular polarization are shown in squares. The inset illustrates the graphic solution of Eqs. (4) and (14). The curves describe the function F_0^E (14). The straight line *L* describes the function F_0^E in the local ($q^2 \to 0$) limit. Straight lines a, b and c describe the left-hand side of Eq. (4) in the ''−'' polarization for successively large values of ξ, d is the left-hand side of Eq. (4) in the ''+'' polarization; *G* and *D* are the gelicon and doppleron solutions respectively, G' is a damped gelicon, and G_L and G_L' present a gelicon and a damped gelicon in the local limit.

electrons obeying the DSCR condition (16) at this point and in its neighborhood. All the three solutions for $\xi < \xi_m$ obviously describe anomalous skin effect in an external magnetic field for model *E*. For small ξ, they coincide with solutions obtained for model *A* to within the factor $3\pi/4$ on the right-hand side of (15).

Just as in the case of models *A*–*D*, the phase ($v_{\mathrm{ph}} = \omega/k$) and group ($v_{\mathrm{gr}} = d\omega/dk$) velocities of a doppleron for model *E* have opposite directions in contrast to those of a gelicon. This can be easily verified by using Eq. (4) which leads in the limit $\gamma \to 0$ to the following relation:

$$v_{\mathrm{gr}} = 2 v_{\mathrm{ph}} \frac{\xi^3 - \partial F_0/\partial(q^2)}{\xi^3}, \tag{21}$$

connecting the values of v_{gr} and v_{ph}. The inset to Fig. 4 shows that $\xi^3 < \partial F_0$ for a doppleron, while for a gelicon we have $\xi^3 > \partial F_0$, which confirms what has been said above. Consequently, the doppleron and gelicon modes having phase velocities of the same direction, but propagating towards each other, are hybridized. This explains the hybridization of the *G*- and *D*-branches of the spectrum and the formation of the ''gap.'' In the opposite case, spectral branches are not coupled together, but are ''pushed apart,'' which is illustrated by the structure of the spectrum of

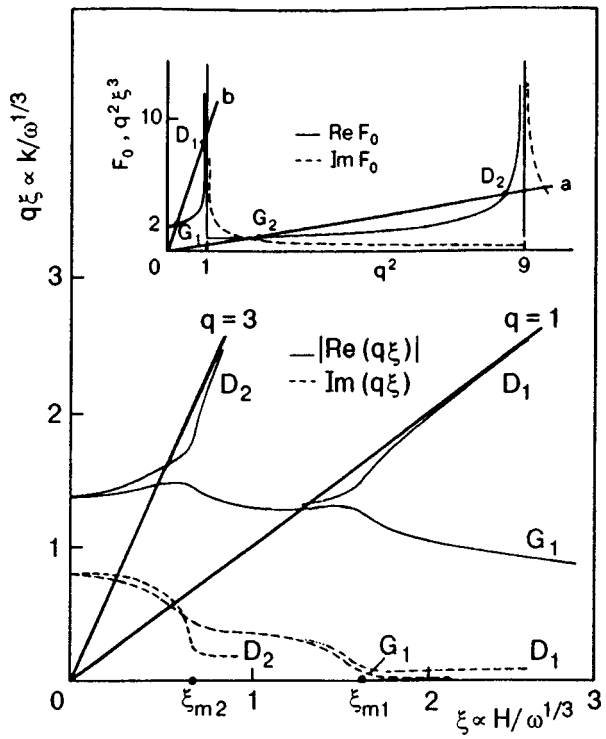

FIG. 5. A fragment of the spectrum of electromagnetic modes in the ''−'' polarization for model E' (numerical solution of Eq. (4) with conductivity (22)). The inset illustrates the graphic solution of Eqs. (4) and (22) in the limit $\gamma\to 0$. The curves describe the functions $F_0^{E'}$ (22). Straight lines a and b describe the left-hand side of Eq. (4) in the ''−'' polarization for successively large values of ξ, G_1 is a gelicon solution, D_1 and D_2 are doppleron solutions; point G_2 is not a solution of the equation since $\mathrm{Re}(F_0)$ and $\mathrm{Im}(F_0)$ are of the same order of magnitude in this range of q^2.

coupled modes in gelicon-phonon resonance under the conditions of strong coupling of a gelicon with sound.[11]

We analyzed several simple models of the FS and proved that the anomalous spin effect can be interpreted as the result of coupling of weakly damped electromagnetic modes of gelicons and dopplerons. Let us now consider a more complex model (E') consisting of two electron surfaces (13) having the same volume ($N_1=N_2=N$), but different values of $|\partial S/\partial p_z|_m$. In this model, the function $F_\pm$ has the form

$$F_\pm^{E'}=[(1\pm i\gamma)^2-q^2]^{-1/2}+[(1\pm i\gamma)^2-\beta^2 q^2]^{-1/2}, \qquad (22)$$

where $q=kv_{m1}/\omega_c$; $\beta=|\partial S/\partial p_z|_{m2}/|\partial S/\partial p_z|_{m1}$. Subscripts $m1$ and $m2$ mark the parameters corresponding to the first and second groups of electrons respectively. In contrast to (14) and (22), $\gamma\neq 0$, which facilitates the identification of different spectral branches. In this case, we assume that $m=\mathrm{const}$ and $\nu=\mathrm{const}$ for all charge carriers.

Figure 5 shows the fragment of the spectrum of electromagnetic modes for model E' with the parameters

$$N=10^{22}\ \mathrm{cm}^{-3},\quad |\partial S/\partial p_z|_m/2\pi\hbar=10^8\ \text{Å}^{-1},$$
$$\omega=10^8\ \mathrm{s}^{-1},\quad \nu=2\times 10^{10}\ \mathrm{s}^{-1},\quad \beta=1/3. \qquad (23)$$

The graphic solution of Eqs. (4) and (22) shows (see the inset to Fig. 5) that if we neglect collisionless damping ($\mathrm{Im}(F_0)=0$), the dispersion equation has four purely real-valued solutions in the limit $\gamma\to 0$. Solutions G_1 and G_2 are of the gelicon type and D_1 and D_2 of the doppleron type. For $\mathrm{Im}(F_0)\neq 0$, point G_2 is not a solution of the equation any longer since $\mathrm{Re}(F_0)\leqslant\mathrm{Im}(F_0)$ in the corresponding range of q^2. The solution D_2 is essentially real-valued if the value of $\mathrm{Re}(F_0)$ (to be more precise, $\partial(\mathrm{Re}(F_0))/\partial(q^2))^{12}$ is large enough as compared to $\mathrm{Im}(F_0)$. For $\nu\neq 0$, all the four solutions become complex-valued.[12] It can be seen from Fig. 5 that the gelicon (G_1) and the doppleron (D_1) modes are coupled in the vicinity of a certain value $\xi=\xi_{m1}$, and both solutions become essentially complex-valued for $\xi<\xi_m$. As the value of ξ decreases further, one of the mode (the one for which v_{gr} and v_{ph} have the same sign) is now coupled with the doppleron mode D_2 in the vicinity of the second critical value $\xi=\xi_{m2}$. As a result, for $\xi<\xi_{m2}$ we go over to the conditions of anomalous skin effect, which is ''classical'' in the region of quite small ξ: $\mathrm{Im}(F_0^{E'})\approx\pm i(1+\beta^{-1})/q$ for $q^2\gg 1$.

CONCLUSIONS

In this paper, we analyzed the nature and forms of anomalous skin effect in normal metals in an external magnetic field. The analysis was based on the graphic and numerical solutions of the dispersion equation. We considered a few simple but typical FS models in order to establish the relation between the peculiarities of the electron energy spectrum and the details of the spectrum of electromagnetic modes. The main results obtained here can be formulated as follows.

(1) From the classical point of view, anomalous skin effect is associated with nonlocal effects in conductivity and the existence of the region of collisionless absorption of waves. The function $F_0\propto i/q$ in the limit $q^2\gg 1$, and the solutions of the dispersion equations are almost independent of H in the region of relatively weak fields (see Fig. 2, model *A*, and Figs. 4 and 5). The analysis of the spectrum of electromagnetic waves for models *A*–*D* proved that in actual practice such a mode can be realized if all the terms in expansion (19) except the first two can be neglected for small p_z. Otherwise, anomalous skin effect is not ''classical'' any longer since the solutions of the dispersion equation can depend significantly on magnetic field. It should also be noted that in zero field this leads to a dependence of anomalous skin effect on the quantity ν.

(2) We proposed a nontraditional point of view to the nature of anomalous skin effect. It was shown that anomalous skin effect can be interpreted as the result of coupling of electromagnetic modes: gelicons and dopplerons. The mechanism responsible for coupling of these modes involves nonlocal effects leading, first, to the emergence of a doppleron solution of the dispersion equation, and second, to hybridization of the gelicon and doppleron spectral branches. This results in the emergence of a ''gap'' in fields smaller than the threshold value since the solutions of the dispersion

equation become essentially complex-valued (see Figs. 2 and 4). These solutions describe anomalous skin effect in an external magnetic field. The problem of coupling of electromagnetic modes is illustrated successfully by model E' (see Fig. 5), in which one of spectral branches is hybridized successively with two doppleron branches. It should be noted, however, that the conditions of the ''classical'' anomalous skin effect are created only in the region $\xi<\xi_{m2}$. However, the conditions of skin effect in the generally accepted sense are not formed in the interval $\xi_{m2}<\xi<\xi_{m1}$ since in addition to complex-valued solutions of the dispersion equation, there exist a solution corresponding to weakly damped doppleron mode D_2.

This research was supported by the Ukrainian State Foundation for Fundamental Studies, Project No. 2.4/211.

*E-mail: tsymbal@host.dipt.donetsk.ua

[1] A. B. Pippard, Proc. R. Soc. London, Ser. A **191A**, 385 (1947).
[2] G. E. H. Reuter and E. H. Soundheimer, Proc. R. Soc. London, Ser. A **195A**, 336 (1948).
[3] A. B. Pippard, Rep. Prog. Phys. **23**, 176 (1960).
[4] M. Ya. Azbel and M. I. Kaganov, Dokl. Akad. Nauk SSSR **XCV**, 41 (1954).
[5] R. C. Alig, Phys. Rev. **165**, 833 (1968).
[6] A. V. Kobelev and V. P. Silin, Fiz. Met. Metalloved. **39**, 231 (1975).
[7] D. E. Muller, Math. Tables and Other Aids to Comput. **10**, 208 (1956).
[8] D. S. Falk, B. Gerson, and J. F. Carolan, Phys. Rev. B **1**, 406 (1970).
[9] V. P. Naberezhnikh, D. E. Zherebchevskii, L. T. Tsymbal, and T. M. Yeryomenko, Solid State Commun. **11**, 1529 (1972).
[10] R. G. Chambers and V. G. Skobov, J. Phys. F **1**, 202 (1971).
[11] E. A. Kaner and V. G. Skobov, Adv. Phys. **17**, 605 (1968).
[12] L. T. Tsymbal and A. N. Cherkasov, Fiz. Nizk. Temp. **24**, 250 (1998) [Low Temp. Phys. **24**, 189 (1998)].

Translated by R. S. Wadhwa

LOW-DIMENSIONAL AND DISORDERED SYSTEMS

The influence of heating of two-level systems on low-temperature nuclear spin–lattice relaxation

N. P. Giorgadze and L. Zh. Zakharov

*Institute of Physics, Georgian Academy of Sciences, 380077 Tbilisi, Georgia**

A. I. Tugushi and L. L. Chotorlishvili

Tbilisi State University, 380028 Tbilisi, Georgia
(Submitted May 18, 1998; revised July 27, 1998)
Fiz. Nizk. Temp. **24**, 1166–1170 (December 1998)

The influence of heating of two-level systems on low-temperature spin–lattice relaxation is studied. Effects of the type of a ''phonon bottleneck'' are investigated in amorphous substances in which the role of resonant phonons is played by resonant tunnel two-level systems.
© *1998 American Institute of Physics.* [S1063-777X(98)00612-4]

The heating of ''resonant phonons'' during spin–lattice relaxation is known as the ''phonon bottleneck effect.''[1] This effect has been reliably established in electron spin–lattice relaxation.[2–4] According to some indications,[5–7] this effect is also manifested in the nuclear spin–lattice relaxation (NSLR).

What has been said above refers directly to NSLR in amorphous materials (glasses) as well as dielectric crystals with defects. It was proved[8–11] that a significant role in nuclear relaxation in these materials is played by two-level systems (TLS) responsible for additional channels for energy flow from a nuclear spin system (NSS) to a thermostat (an aggregate of phonons in the case under investigation). The analysis was based on the prevailing ideas concerning the nature of the relaxation process, according to which the TLS ensuring energy removal from relaxing spins remain in thermal equilibrium with the lattice during the entire process. At the same time the first-order relaxation studied by Buishvili *et al.*[9–11] and associated with modulation of constants of dipole–dipole interaction between the nuclear spins of the matrix and the spins of electron shells of paramagnetic impurities by TLS tunneling from one region of an asymmetric potential well to another is a one-quantum process. This process involves resonant exchange of energy between the nuclear spin and the TLS, during which the NSS interacts directly only with a comparatively small part of the TLS with quasi-Zeeman frequencies which are close to the Zeeman frequency of nuclei. In other words, the situation in this case is completely similar to the one-phonon relaxation, and heating of resonant TLS can generally take place in the course of NSLR when the heat capacity of NSS is considerably larger than the heat capacity of resonant TLS on the one hand, while the rate of energy supply from relaxing nuclei is higher than the rate of energy removal from resonant TLS to the thermostat on the other hand.

The ''phonon bottleneck'' effect can not only change the temperature and field dependences of the observed NSLR time, but also increase this time by two-three orders of magnitude and hence affect the hierarchy of relaxation mechanisms. For this reason, the study of one-quantum NSLR involving TLS taking into account possible heating of the latter systems is of considerable importance. This communication is devoted to an analysis of this problem for the modulation mechanism of relaxation proposed in Ref. 9.

1. Let us consider an amorphous sample a fraction of whose atoms form a TLS in a magnetic field $\mathbf{H}_0$ oriented along the z-axis. Using the model of spin analogy,[12,14] we can write the Hamiltonian of interacting two-level systems in the form

$$H_D=\sum_m H_D(m)+H_{DD}. \tag{1}$$

The first term in this expression is the pseudo-Zeeman energy of a TLS, written as the sum of the energies of TLS packets with identical quasi-Zeeman frequencies ω_m in the expression for the Hamiltonian

$$H_D(m)=\hbar\omega_m\sum_{j_m} d^z_{j_m}. \tag{2}$$

The second term contains the part of interaction between TLS responsible for spectral diffusion and is defined as

$$H_{DD}=\sum_{m\neq n}\sum_{i_m j_n} B_{i_m j_n}(d^+_{i_m}d^-_{j_n}+d^-_{i_m}d^+_{j_n}), \tag{3}$$

where $\omega_m=E_m/\hbar$; $E_m=(\varepsilon_m^2+\Delta_m^2)^{1/2}$ is the energy difference between the levels of TLS, ε_m the asymmetry parameter, Δ_m the binding energy due to tunneling, $d^\alpha_{i_m}$ the TLS pseudospin with the properties of spin 1/2, $B_{ij}\sim 1/64\times\gamma^2\pi\rho v^2 r_{ij}^3$, γ– the TLS–phonon coupling constant, ρ the density of the material, v the velocity of sound in it, and r_{ij} the separation between TLS.

We neglect the secular part of the interaction between TLS belonging to packet m as compared to the quasi-Zeeman energy of the packet, retaining for it only the role of the factor ensuring ''instantaneous'' (from the point of view of

 © 1998 American Institute of Physics

the characteristic time scale of a relaxation process) establishment of thermal equilibrium in packets. The part

$$H'_{DD}=\sum_{m\neq n}\sum_{i_m j_n} A_{i_m j_n} d^z_{i_m} d^z_{j_n}, \tag{4}$$

of interaction between packets, where the constant $A_{i_m j_n} \sim B_{i_m j_n}$, is also omitted in Hamiltonian (1) since it does not affect the form of kinetic equations describing the relaxation process under investigation. However, this part must be taken into account in the calculation of corresponding correlation functions that determine some coefficients in this equation. The remaining part of the interaction between TLS is neglected.

We write the NSS Hamiltonian in the form to the Zeeman energy of the system, i.e.,

$$H_I=-\hbar\omega_I\sum_i I^z_i \tag{5}$$

(ω_I is the Zeeman frequency of the nuclear spins of the matrix), neglecting the secular component of the dipole–dipole interaction of nuclei in view of its comparative smallness. However, this component still plays the role of a source of randomization in the NSS, which establishes thermal equilibrium in the nuclear Zeeman reservoir during the time T_2 of transverse relaxation. We also assume that the time T_2 is smaller than the characteristic time scales of the relaxation process.

The Hamiltonian describing the interaction of nuclear spins with TLS and responsible for the relaxation mechanism under investigation follows from the Hamiltonian of dipole dipole interaction of nuclear spins of the matrix with electron spins of paramagnetic impurities in the representations chosen for describing TLS:[9,11]

$$H_{ID}=-\frac{1}{4}\sum_\mu\sum_m\sum_{j_m}(v^{z-}_{j_m\mu}I^+_{j_m}+v^{z+}_{j_m\mu}I^-_{j_m}) \times s^z_\mu(d^+_{j_m}+d^-_{j_m})\sin\theta_m, \tag{6}$$

where

$$v^{z\pm}_{ij}=(3\gamma_I g\hbar^2/r^3_{ij})(l/r_{ij})F^{z\pm}_{ij}(\theta_{ij}\varphi_{ij});$$

$$\sin\theta_m=\frac{\Delta_m}{E_m};$$

γ_I and $(-g)$ are the gyromagnetic ratios for matrix nuclei and electrons of impurities $(g>0)$, l the separation between the minima of the asymmetric potential well of the TLS (we neglect the spread in l_m), $\mathbf{r}_{j_m\mu}$ is the radius vector connecting the j_mth nucleus with the μth impurity, $F^{z\pm}_{ij}$ is the $\mathbf{r}_{ij}$ function depending on the meridional (θ_{ij}) and azimuthal (φ_{ij}) angles (its explicit form will not be required in our analysis), and S^z_μ the electron spin.

Expressions (1), (5), and (6) must be supplemented with the Hamiltonian H_L of the lattice (thermostat) and the Hamiltonian H_{DL} describing the interaction of the TLS system with the thermostat, whose explicit forms will not be required either. Thus, we can write the initial Hamiltonian describing the interacting NSS and the lattice in the form

$$H=H_0+H', \tag{7}$$

where

$$H_0=H_I+\sum_m H_D(m)+H_L,$$

$$H'=H_{DD}+H_{ID}+H_{DL}. \tag{8}$$

2. Let us go over to a semi-thermodynamic description of the NSLR process. Taking into account the presence of fast randomization sources in the NSS and TLS packets and presuming the presence of such a source in the thermostat (lattice), we regard them as thermodynamic subsystems characterized by the temperatures T_I, T_m, and T_L respectively. In this case, NSLR is the process of establishment of complete thermal equilibrium in the quasi-equilibrium system comprising the thermodynamic subsystems (NSS, TLS packets, and thermostat).

We shall describe the time evolution of this system by using the method of nonequilibrium statistical operator (NSO).[13] After simple calculations (similar to those made by Buishvili *et al.*[6,16,17]), we obtain the following system of equations in the high-temperature approximation in nuclear spins:

$$\frac{d\beta_I}{dt}\approx-\frac{\beta_I-\beta(E_I)}{T_{IE_I}}, \tag{9}$$

$$\frac{\partial\beta(E)}{\partial t}=D\frac{\partial^2\beta(E)}{\partial E^2}-\frac{\beta(E)-\beta_I}{T_{EI}}-\frac{\beta(E)-\beta_L}{T_{EL}}, \tag{10}$$

where

$$\frac{1}{T_{IE_I}}=\frac{\pi}{4}f_{ID}f_s(\overline{s^z_0})^2\frac{6v^2(a)}{\hbar E_{\max}}, \tag{11}$$

$$\frac{1}{T_{EI}}=\frac{\pi}{2}f_s(\overline{s^z_0})^2\langle I^+_0 I^-_0\rangle\frac{6v^2(a)}{\hbar^2}G(E/\hbar-\omega_I), \tag{12}$$

$$D=2\pi\frac{[12A(a)B(a)]^2}{\hbar\beta_L E^2_{\max}}f^4_{ID}, \tag{13}$$

$$\frac{1}{T_{EL}}=\frac{\gamma^2E^2}{\pi\rho v^5\hbar^4\beta_L}. \tag{14}$$

Here $\beta(E_I)$ is the reciprocal temperature of a TLS with energy E_I, f_{ID} the relative concentration of TLS, f_s the relative concentration of paramagnetic impurities, $E_{\max}$ the maximum energy of splitting of tunnel TLS, D the diffusion coefficient obtained earlier,[16], and $G(E/\hbar-\omega_I)$ the Fourier transform of the correlation function

$$G_m(t)=\frac{\langle\tilde{d}^+_{i_m}(t)d^-_{i_m}\rangle}{\langle d^+_{i_m}d^-_{i_m}\rangle}.$$

While deriving Eqs. (9) and (10), we considered limited spectral diffusion in the ensemble of TLS, assuming that the diffusion length is smaller than ω_I. In this case, an active role in NSLR is played only by TLS with quasi-Zeeman frequencies from a frequency interval of the order of diffusion length in the vicinity of ω_I. The remaining TLS rather play a passive role in this process and can be included in the

thermostat (as if often done in an analysis of the ''phonon bottleneck'' effect).[1,4] While deriving Eq. (9), we assumed that $\beta(E)$ changes insignificantly over the correlator width $G_m(t)=G(t)$ and neglected the first moment of the correlator

$$G_{mn}(t)=\frac{\langle \tilde{d}^+_{i_m}(t)\tilde{d}^-_{j_n}(t)d^-_{i_m}d^+_{j_n}\rangle}{\langle d^+_{i_m}d^-_{j_n}d^-_{i_m}d^+_{j_n}\rangle},$$

which is small in the high-temperature approximation. We also took into account the fact that only resonant TLS with energies $E\sim E_I=\hbar\omega_I\gg l_D$ play an active role in the NSLR (here l_D is the spectral diffusion length which will be estimated below). Finally, Eq. (10) is supplemented with a term describing the relaxation of TLS to the lattice. The source of this term is the interaction H_{DL} whose explicit form is borrowed from Ref. 15.

Concluding the section, we observe that the limiting case in which the width of the NMR line is much larger than the width of the Fourier transform of the correlator $G_m(t)$ can be considered in complete analogy with the case analyzed above. In this limiting case, the Fourier transform of the TLS correlator in expression (12) is replaced by the Fourier transform of the nuclear spin correlator

$$I^{+-}(\omega)=\frac{1}{2\pi}\int_{-\infty}^{+\infty}dt e^{i\omega t}\frac{\langle \tilde{I}^+_{i_n}(t)I^-_{i_n}\rangle}{\langle I^+_{i_n}I^-_{i_n}\rangle},$$

$$\tilde{I}^+_i(t)=e^{iH_{II}t/\hbar}I^+_i e^{-iH_{II}t/\hbar}.$$

3. Let us now analyze qualitatively the system of equations (9) and (10). It is natural to expect that when the thermal equilibrium between the NSS and the thermostat is violated, heat transfer emerges first of all between the NSS and the TLS packets belonging to a narrow energy range $|E-E_I|\sim\hbar/\tau_D$, where $\tau_D=128\rho v^2a^3\beta_L E_{\max}\hbar/\gamma^2 f_{ID}$ is the time of correlation $G(t)$ given in Ref. 17. Since the value of T_{EI} is virtually the same for all these TLS packets and is of the same order of magnitude as T_{E_II}, we can assume that these packets will have the same temperature in the course of heat transfer, forming together a certain ''initial'' thermodynamic subsystem. It can easily be seen that the heat capacity of this subsystem is given by

$$e^*=\frac{1}{4}k_B(2\hbar/\tau_D E_{\max})N_{ID}(\beta_L E_I)^2$$

(here N_{ID} is the number of TLS per unit volume of the sample) and is negligibly small as compared to the heat capacity of the NSS. It follows hence (according to Eqs. (9) and (10)) that if $T_{E_II}\ll T_{E_IL}$, the temperature of the TLS subsystem formed during mutual relaxation with the NSS tends to the NSS temperature at the rate

$$\frac{1}{T^*}=\frac{\pi}{4}f_s(\overline{s^z_0})^2\langle I^+_0I^-_0\rangle\left(\frac{6v^2(a)}{\hbar^2}\right)\tau_D\sim\frac{1}{T_{E_II}}.$$

At the same time, spectral diffusion ''smears'' the energy supplied from the NSS over a ''distance'' of the order of diffusion length $l_D\sim\sqrt{DT^*}$ during the time of the order of T^*. Consequently, we can assume in our qualitative analysis that a subsystem of resonant TLS characterized by the same reciprocal temperature β_p and consisting of TLS packets belonging to the energy interval of the order of l_D near the frequency ω_I is formed in the aggregate of TLS at the initial stage of the relaxation process. As regards the remaining TLS packets, they can be assumed to be in equilibrium with the thermostat, forming a single entity with it.[1)] It was mentioned above that such a simplified approach is often used in analysis of the ''phonon bottleneck'' effect.[1,4]

The equations describing the next stage of NSLR including the relaxation of the NSS and the subsystem of resonant TLS to the thermostat can be obtained from the initial system by multiplying Eq. (10) by $(1/4)(N_{ID}E^2/E_{\max})$, integrating with respect to E over the interval $E_I\pm l_D$ for $\beta(E)=\beta_p$ and substituting the values of $\beta(E_I)=\beta_p$ into Eq. (9). This gives

$$\frac{d\beta_I}{dt}=-\frac{\beta_I-\beta_p}{T_{Ip}},\quad \frac{d\beta_p}{dt}=-\frac{\beta_p-\beta_I}{T_{pI}}-\frac{\beta_p-\beta_L}{T_{pL}},\qquad (15)$$

where

$$\frac{1}{T_{pI}}=\frac{\pi}{2}f_s(\overline{s^z_0})^2\langle I^+_0I^-_0\rangle\left(\frac{6v^2(a)}{\hbar^2}\right)(\hbar/2l_D);\qquad (16)$$

$T_{Ip}=T_{IE_I}$ is defined by expression (11) and $T_{pL}=T_{E_IL}$ by expression (14). The system of equations (15) formally coincides with that obtained in Refs. 1, 4 while analyzing the phonon bottleneck effect, and its consequences are well known. If $T_{pI}\gg T_{pL}$, the subsystem of resonant TLS remains in equilibrium with the thermostat during the entire NSLR process ($\beta_p=\beta_L$), while the NSS relaxes (according to the first equation from (15)) to the thermostat during the time T_{Ip} which is independent of magnetic field and temperature in the given case. This obviously corresponds to the conventional NSLR. If, however, $T_{pI}\ll T_{pL}$, the ''light'' subsystem of resonant TLS whose heat capacity $e_p=1/4[k_B\times(2l_D/E_{\max})(\beta_I E_I)^2N_{ID}]$ is much smaller than the heat capacity of the NSS is the first to attain equilibrium with the NSS during the time of the order of T_{pI} (short stage), after which the resulting combined thermodynamic subsystem NSS+TLS comes in equilibrium with the thermostat over the time $T_{IL}=T_{pL}l_I/l_p\gg T_{pL}$ (long stage). The total relaxation time is virtually determined by T_{IL} which is longer than T_{Ip}, i.e., the NSLR time that would have been observed under given conditions in the absence of heating of resonant TLS, by a factor of $\sigma=T_{pL}/T_{pI}$. It is important that $T_{IL}\propto(H_0T_L)^{-2}$. Thus, we can see that the heating of resonant TLS slows down NSLR and also changes the field and temperature dependences of relaxation time. In the opposite limiting case, the field and temperature dependences of T_{IL} are slightly modified and assume the form $T_{IL}\propto H_0^{-2}T_L^{-3/2}$.

Concluding the section, we give some numerical estimates. Assuming that $f_{ID}\sim10^{-4}$, $f_s\sim10^{-4}$, $\gamma\sim10^{-12}$ erg, $E_{\max}\sim4\times10^{-14}$ erg, $\rho\sim3$ g/cm^3, $v\sim4\times10^5$ cm/s, $a\sim5\times10^{-8}$ cm, $l/a\sim5\times10^{-2}$, $\gamma_I\sim2.5\times10^4\,\mathrm{G}^{-1}\cdot\mathrm{s}^{-1}$, $g\sim10^7\,\mathrm{G}^{-1}\cdot\mathrm{s}^{-1}$, $T\sim10^{-2}$ K, $H_0\sim3\times10^3$ G, $(\overline{s^z_0})^2\sim1/4$, $\langle(I^z_0)^2\rangle\sim1/4$, $\langle I^+_0I^-_0\rangle\sim1/2$, we obtain $T_2\sim2\times10^{-4}$ s and $\tau_D\sim3\times10^{-3}$ s, i.e., the NMR line width is larger than the width of the correlator $G(t)$. Using the corresponding ex-

pressions for kinetic coefficients, we obtain $T^* \sim 0.8 \times 10^{-2}$ s, $D \sim 7.6 \times 10^{-42}\,\mathrm{erg^2 \cdot s^{-1}}$, $l_D \sim 2.5 \times 10^{-22}$ erg, $T_{pI} \sim 4 \times 10^{-1}$ s, and $T_{pL} \sim 10$ s. It follows hence that the high-temperature approximation in nuclei, the hierarchy of time scales $T_2 \ll \tau_D \ll T^* \ll T_{pI} \ll T_{pL}$, and the hierarchy of energy scales $\hbar/T_2 \ll l_D \ll \hbar\omega_I$ which were adopted in the construction of the theory are preserved. The bottleneck coefficient $\sigma = 25$. For $l/a \sim 10^{-1}$ and $\gamma_I \sim 10^4\,\mathrm{G^{-1} \cdot s^{-1}}$, we obtain $E_{\max} \sim 10^{-14}$ erg for constant values of the remaining parameters $T_2 \sim 10^{-3}$ s and $\tau_D \sim 7 \times 10^{-4}$ s, and hence the opposite limiting case is realized. The corresponding expressions for kinetic coefficients give in this case

$$T^* \sim 3 \times 10^{-3} \text{ s}, \quad D \sim 10^{-40} \text{ erg}^2 \cdot \text{s}^{-1},$$

$$l_D \sim 10^{-21} \text{ erg}, \quad T_{pI} \sim 1 \text{ s},$$

i.e., the conditions assumed in the construction of the theory can be observed in this case also, and for the bottleneck coefficient we have $\sigma \sim 10^3$.

Thus, the above estimates suggest that the heating of resonant TLS in one-quantum NSLR in amorphous materials can affect significantly the relaxation process at ultralow temperatures also.

The authors are grateful to R. R. Homeriki for valuable remarks made during the discussion of this paper.

This research was carried out owing to Grant No. 2.12 from the Georgian Academy of Sciences.

*E-mail: root@imedil.postnet.ge

[1)] If, on the contrary, $T_{E_jL} \ll T_{E_jI}$, all the TLS packets will remain in equilibrium with the thermostat during the entire relaxation process. Consequently, the ensemble of resonant TLS can be formally treated, as before, as a thermodynamic subsystem, which however, does not participate actively in the NSLR.

[1] C. J. Gorber. L. C. Van der Mavel, and B. Bolger, Physics **21**, 103 (1955).
[2] L. C. Van der Mavel. J. Van der Broech, and C. J. Gorber, Physics **123**, 361 (1957).
[3] P. L. Scott and C. D. Jeffries, Physics **127**, 32 (1962).
[4] B. W. Faughnan and M. V. P. Strandberg, J. Phys. Chem. Solids **19**, 155 (1961).
[5] S. M. Day, E. Obsuka, and B. Josephson, Phys. Rev. A **137**, 108 (1965).
[6] L. L. Buishvili, N. P. Giorgadze, and G. R. Khutsishvili, Zh. Éksp. Teor. Fiz. **60**, 1433 (1971) [Sov. Phys. JETP **33**, 776 (1971)].
[7] M. A. Teplov, M. Staudte, and G. Feller, Fiz. Tverd. Tela (Leningrad) **22**, 2460 (1980) [Sov. Phys. Solid State **22**, 1433 (1980)].
[8] T. L. Reineke and K. L. Ngai, Phys. Rev. B **12**, 3476 (1975); G. Balzer-Jollenbeck, O. Kanest, and J. Steinert, Solid State Commun. **65**, 303 (1988).
[9] L. L. Buishvili, A. I. Tugushi, L. Zh. Zakharov, and N. P. Fokina, Physica B **168**, 205 (1991).
[10] L. L. Buishvili, A. I. Melikadze, and A. I. Tugushi, Zh. Éksp. Teor. Fiz. **94**, 227 (1988) [*sic*].
[11] L. L. Buishvili, N. P. Giorgadze, and R. L. Lepsveridze, Fiz. Nizk. Temp. **21**, 931 (1995) [Low Temp. Phys. **21**, 717 (1995)].
[12] P. W. Anderson, B. J. Halperin, and C. Varma, Philos. Mag. **25**, 1 (1972).
[13] D. N. Zubarev, *Nonequilibrium Statistical Thermodynamics* [in Russian], Nauka, Moscow (1971).
[14] J. Black, in *Glassy Metals* (ed. by H. Güntherodt and H. Beck), Springer, Heidelberg (1981).
[15] S. Hunklinger and W. Arnold, in *Physical Acoustics* (ed. by R. N. Thurston and W. A. Mason). vol. 12 (1976).
[16] L. L. Buishvili, L. Zh. Zakharov, and A. I. Tugushi, Teor. Mat. Fiz. **96**, 453 21 (1993).
[17] L. L. Buishvili and N. P. Giorgadze, Izv. Vuzov, Radiofizika **14**, 1493 (1971).

Translated by R. S. Wadhwa

Optical spectroscopy of disorder in molecular chains (*J*-aggregates)

Yu. V. Malyukin, O. G. Tovmachenko, and G. S. Katrich

Institute of Single Crystals, National Academy of Sciences of the Ukraine, 310001 Kharkov, Ukraine[*]

K. Kemnitz

Europhoton GmbH, D-12247 Berlin, Germany[**]

(Submitted May 22, 1998; revised July 30, 1998)
Fiz. Nizk. Temp. **24**, 1171–1180 (December 1998)

The form of the exciton absorption band for $1D$ molecular chains and their luminescence are investigated in glass matrices of various composition and in Langmuir–Blodgett (LB) films under selective excitation. It is shown that the exciton absorption band for $1D$ chains is always asymmetric. The shape of the low-frequency edge of their absorption band changes from the Gaussian to the Lorentzian depending on the method of obtaining of $1D$ chains due to a change in the diagonal and off-diagonal disorder in molecular chains. Under selective excitation of $1D$ molecular chains, the effect of considerable luminescence band narrowing is not observed. This is associated with statistical properties of the exciton absorption band and with relaxation processes in the materials under investigation in the excited state.
© *1998 American Institute of Physics.* [S1063-777X(98)00712-9]

1. INTRODUCTION

From the moment of their discovery in 1930's,[1,2] *J*-aggregates (molecular chains)[3] remained exotic objects of chemical investigations for a long time. During the last decade, however, the situation has changed radically. A number of fundamental physical results on exciton dynamics in these systems were obtained by using *J*-aggregates.[4–13] The concept of exciton delocalization played the key role in the interpretation of these results.[12–17] The degree of delocalization of an exciton in *J* aggregates is usually expressed in terms of the number of coherently coupled molecules in a molecular chain.[12–17] Delocalization of an exciton in a *J*-aggregate is determined by two physical parameters, viz., resonant dipole–dipole interaction and diagonal disordering.[12–17]

It should be noted that an analysis of the effect of (diagonal and off-diagonal) disordering[18] on the electron states of $1D$ systems extends far beyond the application specifically to *J*-aggregates and is of general importance.[18–20] The overwhelming majority of publications in this field are of theoretical type, and the conclusions have not received a detailed experimental verification. For example, the well-known general concept[18,19] concerning complete localization of electron (and any other)[18] excitations in $1D$ systems with an indefinitely small diagonal disordering gives rise (from the experimental point of view) to the following questions (which are quite important even today): is this statement applicable to actual $1D$ systems? how can the quantitative characteristic of the degree of delocalization of electron wave functions be obtained from the results of experiments? and how can the disorder of actual $1D$ systems be monitored and controlled?

Some answers to these questions were obtained as a result of analysis of the spectra and dynamics of exciton excitations in *J*-aggregates.[4–8,12,13] Considerable advances in the solution of the problem concerning the effect of disordering on exciton dynamics were made just for *J*-aggregates both in the experimental[4–8,12,13] and in the theoretical[12–17] aspects. An analysis of the effect of disorder on the spectra and exciton dynamics of $1D$ systems was based on the model of a completely noncorrelated diagonal disordering associated with the Gaussian distribution of optical transition frequencies in individual molecules forming a $1D$ system. Knapp[17] proved that the full width at half maximum ($\Delta\nu_{\mathrm{FWHM}}$) of the absorption band for *J*-aggregates is smaller by a factor of $N^{1/2}$ (N is the number of coherently coupled molecules in the *J*-aggregate) than $\Delta\nu_{\mathrm{FWHM}}$ of the absorption band for isolated molecules. Besides, N appears in the relation connecting the radiation decay constant for excitons in *J*-aggregates with the radiation decay constant for an electron excitation in individual molecules: the time of exciton radiation decay is smaller by a factor of N than the radiation decay constant for an electron excitation in individual molecules.[14–16] In other words, the results obtained in Refs. 14–17 make it possible to connect independent experimentally observed quantities with exciton delocalization in *J*-aggregates.

It was established in the same simple approximation of noncorrelated diagonal disorder[21,22] that this disorder leads to asymmetry of the exciton absorption band in $1D$ systems. The form of the absorption band is described by half the Gaussian contour from the low-frequency side and half the Lorentzian contour on the high-frequency side.[21,22] Such an asymmetry of the exciton absorption band was observed in *TKhB* crystals[23] and in *J*-aggregates of PIC[12,13] and TDBC.[5]

Knoester[24] analyzed a more complex model of diagonal disorder with interstitial correlation, which can be estimated only on the basis of experiments on two-frequency pumping.[24] The shape of the exciton absorption band for $1D$ systems is insensitive to the degree of correlation of diagonal disordering.[17,24] Experiments with two-frequency pumping

 © 1998 American Institute of Physics

were carried out for *J* aggregates of PIC[6] and TDBC.[5] It follows[5,6] that the correlation scale of diagonal disorder amounts to 50–100 molecules for *J*-aggregates in PIC[6] and several hundred molecules for *J*-aggregates in TDBC.[5,6] On the other hand, the exciton absorption band for *J*-aggregates in PIC ($\Delta\nu_{\mathrm{FWHM}}=34\,\mathrm{cm}^{-1}$)[25] is much narrower than that for *J*-aggregates in TDBC ($\Delta\nu_{\mathrm{FWHM}}=240\,\mathrm{cm}^{-1}$).[5] These contradictory results are not quite clear[5,6] and indicate that the model of correlated diagonal disorder requires further detailed investigations.

In analogy with $3D$ systems,[12,13,18,19] it was assumed for a long time that off-diagonal disorder in $1D$ systems is manifested similarly to diagonal disorder. It was proved, however,[12,13] that off-diagonal disorder associated with a random distribution of distances (orientations) between nearest molecules in a $1D$ system leads to a change in the contour of the low-frequency edge of the exciton absorption band in the $1D$ system. In this case, it is described by half the Lorentzian contour like the high-frequency edge.[12,13,21,22] This fact has not been confirmed experimentally so far. It should also be noted that the degree and type of disordering in experiments with real $1D$ systems[4–9,12,13,18,19] virtually remained uncontrolled.

Having analyzed the known methods of obtaining *J*-aggregates in solutions[1,2,26,27] and monomolecular layers,[28] we drew the preliminary conclusion that the method of obtaining *J*-aggregates used by us earlier[10,11] can make it possible to monitor and control the disordering in molecular chains, which would apparently provide a real opportunity to verify experimentally the basic concepts concerning the effect of disordering on the exciton spectra and exciton dynamics in $1D$ systems, which were formulated in Refs. 12, 13, 18–22.

This research aims at a detailed analysis of the contour of the low-temperature exciton absorption band of *J*-aggregates in 1-methyl-1′-octadecyl-2,2′-iodide cyanine (S120) in glass matrices of various compositions and in Langmuir–Blodgett (LB) films[28] as well as at an analysis of the luminescence spectrum for *J*-aggregates under selective excitation to the absorption band.

2. EXPERIMENTAL TECHNIQUE

Absorption and luminescence spectra of the samples under investigation were recorded by automated spectrofluorimeter based on the monochromator *MDR*-23. The monochromator was controlled and spectra were recorded by using electronic moduli manufactured in the CAMAC standard. The CAMAC crate was connected through an interface with a PC based on an INTEL-286 processor.

Low temperatures were attained by using an optical helium cryostat P-46 with evacuation of helium vapor. The cooling rate for the samples was constant when the cryostat was filled with liquid nitrogen and helium in each experiment.

The technique used for obtaining *J*-aggregates of S120 in solution was borrowed from Ref. 27. The essence of this method is that the association of molecules into the initial S120 solution in dimethyl formamide (DMFA) with a concentration of 10^{-4} M is initiated by adding a fraction of distilled water. Only in this case the association of molecules is observed, and the narrow long-wave absorption band for *J*-aggregates appears.[27] A gradual increase in water concentration in the binary solution did not lead to a monotonic increase in the number of associated molecules. We found that the fraction of associated molecules changes abruptly from 30 to 45% when the water content in the binary solution is ~50%. A further increase in water concentration from 50 to 80% led to an insignificant increase in the number of associated molecules. The binary solution prepared in this way and containing *J*-aggregates and nonassociated molecules of S120 was poured into glass cells and cooled to superfluid helium temperature. If we assume that a *J*-aggregate consists of 50 molecules of S120 (according to estimates given below, the number of coherently coupled molecules in a *J*-aggregate of S120 amounts to 25–30), the actual concentration of free S120 molecules and *J* aggregates (a *J*-aggregate is treated as a single molecule) in the glass matrix is of the order of 10^{-6} mole/l. For such concentrations, the interaction between free S120 molecules and *J*-aggregates is ruled out completely, and the overall absorption spectrum of the investigated samples is an additive sum of the absorption spectra of nonassociated molecules and *J*-aggregates.

Molecular layers of S120 were deposited on glass substrates prepared preliminarily according to the Langmuir–Blodgett technology.[28] Molecular piles of S120 molecules were stacked on a substrate to form two-dimensional structures of the ''brick-laying'' type.[29]

While processing experimental spectra, we used, in addition of minimization of the standard deviation, the visual representation of the result of approximation in the form of deviations of experimental points from the approximation curve. In the ideal case, statistical noises in the experimental spectrum should be distributed uniformly relative to the approximation curve which is taken as the zero line.

3. DISCUSSION OF EXPERIMENTAL RESULTS

The absorption spectrum of the samples under investigation was an additive sum of the narrow absorption band for *J*-aggregates of S120 and a broad absorption band for nonassociated S120 molecules. In order to analyze the form of the exciton absorption band for *J*-aggregates, we had to determine the effect produced on it by the absorption band of S120 molecules. The most important case that will be considered in detail is observed in a glass matrix with 50% of water, when the intensity of the absorption band for individual S120 molecules is higher than the intensity of absorption band for *J*-aggregates (Fig. 1). In order to choose the correct number and type of contours for approximating the experimental spectra by the least squares method, we proceeded from physical considerations following from experiments. Above all, we were interested in the shape of the long-wave edge of the absorption band for S120 molecules, which could produce the strongest effect on the absorption band of *J*-aggregates.

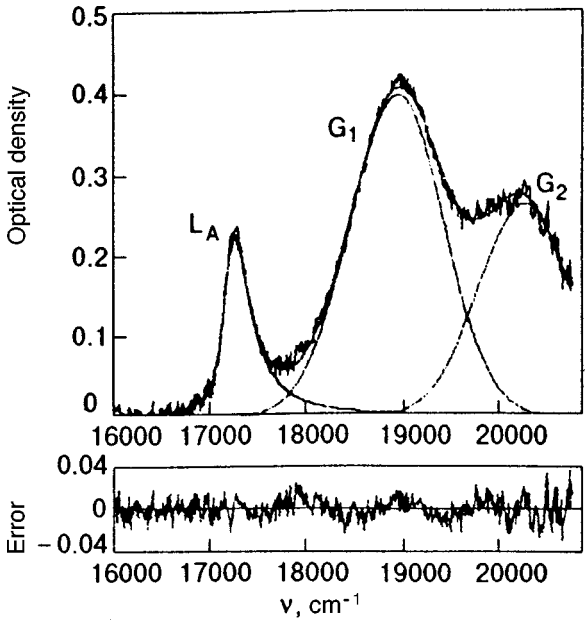

FIG. 1. Overall absorption spectrum of S120 molecules and *J*-aggregates in the glass matrix DMFA:B with 50% water ($T=1.5$ K).

The absorption spectrum of S120 molecules in a binary solution with 15% of water (without *J*-aggregates) contained the principal peak ($\lambda_{max}=528$ nm) and an oscillatory repetition ($\lambda_{max}=492$ nm) (Fig. 2). The absorption spectrum of S120 molecules was described best of all (we mean the minimum standard deviation and the criterion of uniform distribution of noises relative to the zero line) by the sum of two Gaussian contours $G_1(\Delta\nu_{FWHM}=1206\,\text{cm}^{-1}, \lambda_{max}=528\,\text{nm})$ and $G_2(\Delta\nu_{FWHM}=1005\,\text{cm}^{-1}, \lambda_{max}=492\,\text{nm})$ (Fig. 2a). The description using two Lorentzian curves deteriorated the approximation considerably especially near the long-wave edge (Fig. 2b). This is in accord with the fact that low-temperature spectra of individual molecules in dielectric matrices of various structure are broadened nonuniformly as a rule and are described by Gaussian contours.[30–34] Normalizing the absorption spectra presented in Figs. 1 and 2 to unity, we superimposed them on the same diagram (Fig. 3). It can be seen that the spectrum of individual S120 molecules in a binary solution with 20% of water exactly coincides with the absorption spectrum of S120 molecules in the presence of *J*-aggregates. Consequently, we can rightfully use two Gaussian contours for approximating the absorption band of S120 molecules in the spectrum shown in Fig. 1. We approximated the absorption band for *J*-aggregates (see Fig. 1) by symmetric and asymmetric Lorentzian and Gaussian contours as well as the asymmetric compound Gauss–Lorentz contour with different half-width of the components. The best approximation of the spectrum presented in Fig. 1 was obtained by using two Gaussian contours $G_1(\Delta\nu_{FWHM}=1176\,\text{cm}^{-1}, \lambda_{max}=527.5\,\text{nm})$ and $G_2(\Delta\nu_{FWHM}=995\,\text{cm}^{-1}, \lambda_{max}=493.3\,\text{nm})$ and an asymmetric Lorentzian contour $L_A(\Delta\nu_{FWHM}=380\,\text{cm}^{-1}, \lambda_{max}=580\,\text{nm})$. The parameters of the Gaussian contours are close to those used for approximating the spectrum of S120 molecules without the absorption band for *J*-aggregates (see Fig. 2). The contour amplitude G_1 in the region of the absorption band of *J*-aggregates is negligibly small (equal to zero at the low-frequency edge of the *J*-band). Consequently, the effect of the absorption band for S120 molecules on the absorption band of *J*-aggregates is insignificant, and the *J*-band can be singled out from the overall spectrum (see Fig. 1) by subtracting the experimental absorption spectrum for S120 molecules or two contours G_1 and G_2 with the parameters obtained from the approximation. The results of such a subtraction in both cases are identical and are presented in Fig. 4. The same

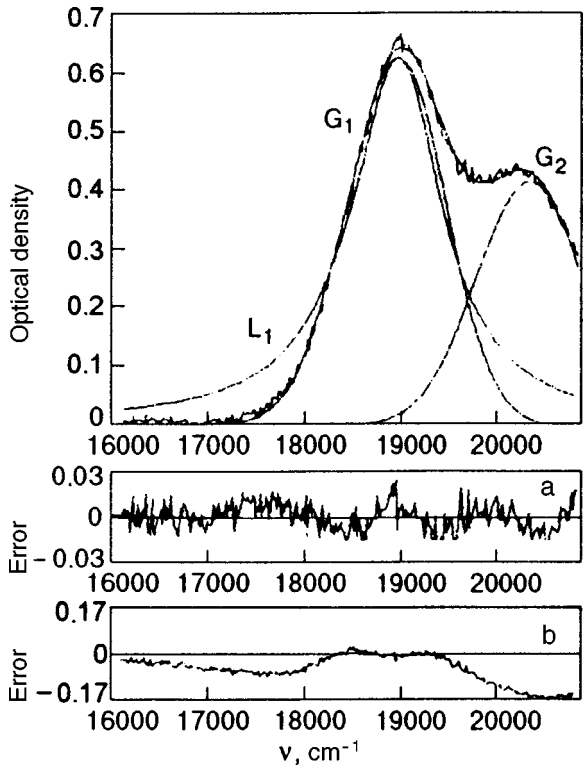

FIG. 2. Absorption spectrum of S120 molecules in the glass matrix DMFA:B with 15% water ($T=1.5$ K): deviation of experimental points from the approximation curve (G_1+G_2) (a) and (L_1+L_2) (b). (The L_2 contour and the overall theoretical curves are not shown).

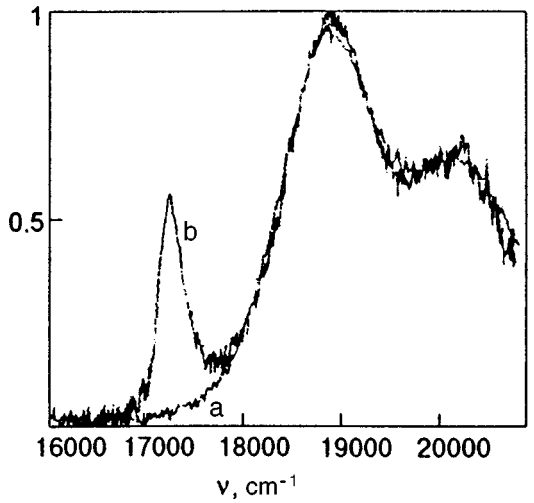

FIG. 3. Absorption spectrum (a) shown in Fig. 2 inscribed in the absorption spectrum (b) shown in Fig. 1.

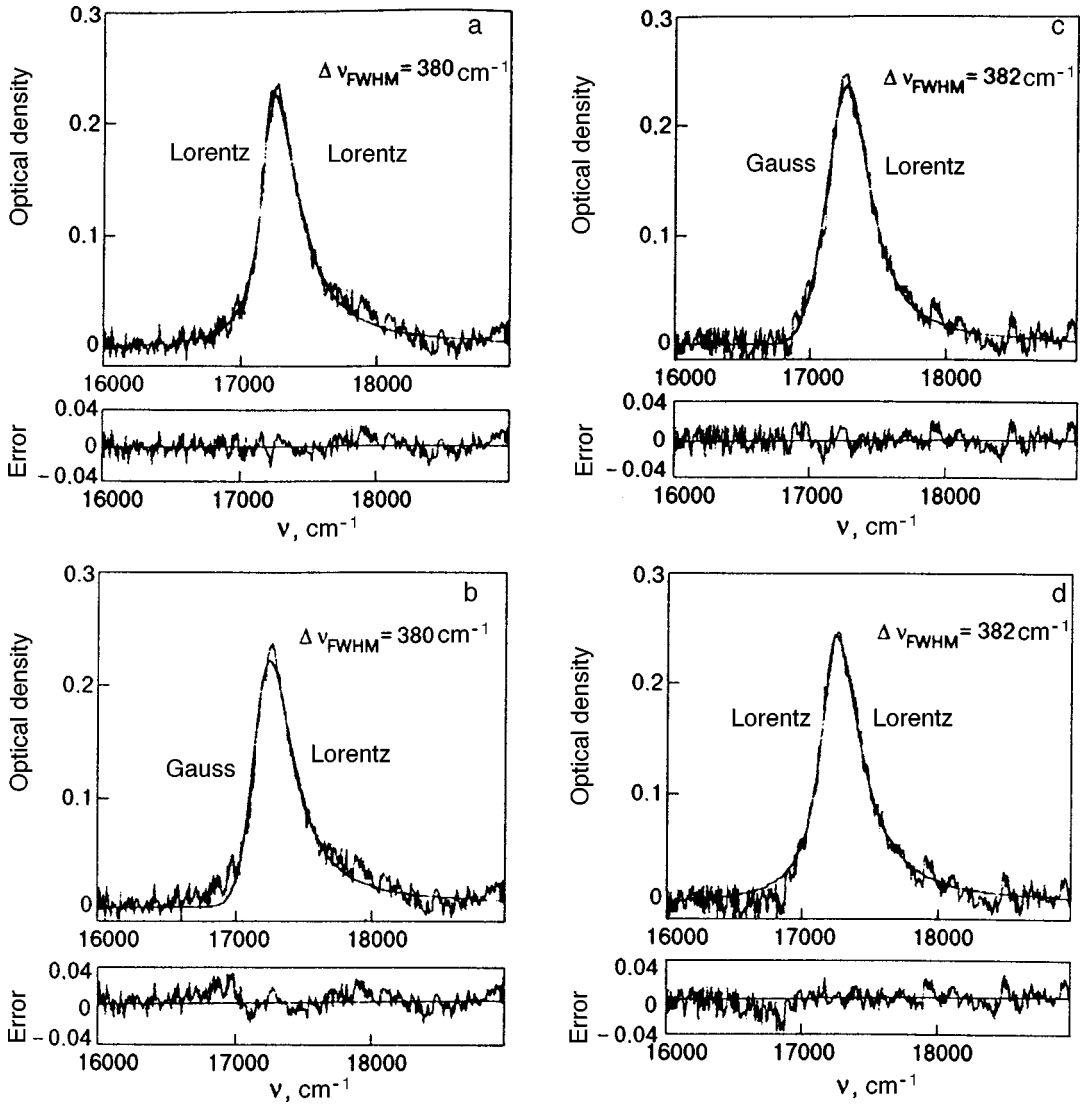

FIG. 4. Absorption band for *J*-aggregates of S120 at $T=1.5$ K in the glass matrix DMFA:B=1:1, approximated by an asymmetric Lorentz contour (a) and by a compound Gauss–Lorentz contour (b); in the glass matrix DMFA:B=1:2.5 approximated by a compound Gauss–Lorentz contour (c) and by an asymmetric Lorentz contour (d).

figure shows a comparative approximation of the *J*-band by an asymmetric Lorentzian contour (Fig. 4a) and a compound Gauss–Lorentz contour (Fig. 4b). It can be seen that the Gaussian function describes worse the low-frequency edge of the *J*-band since the statistical spread deviates noticeably from the zero line (see Fig. 4b). In the dielectric glass matrix DMFA:B=1:2.5, the *J*-band was broader than the absorption band of nonassociated S120 molecules by a factor of several units,[11] and hence the effect of this band on the *J*-band was even smaller. However, we singled out the *J*-band in the same way as above for the sake of unification in the glass matrix with a high water content (see Fig. 4c), the absorption band for *J*-aggregates is described most successfully by a compound asymmetric Gauss–Lorentz contour. The application of an asymmetric Lorentz–Lorentz curve in this case deteriorated the approximation of the experimental spectrum considerably (Fig. 4d).

Our analysis shows that the shape of the exciton absorption band for *J*-aggregates in the glass matrix with a high content of water (see Fig. 4) coincides with those predicted for 1*D* systems with diagonal disordering[21,22] and observed earlier for *J* aggregates of PIC and TDBC.[5,6,12,13] The microscopic mechanism of the emergence of diagonal disorder in the molecular chain of a *J*-aggregate is associated with fluctuation of local molecular fields leading to the well-known nonuniform broadening of optical transitions of impurity centers in crystals and glasses.[30–34] The change in the shape of the long-wave edge of the absorption band for *J*-aggregates in the glass matrix with a low content of water (see Fig. 4) should be attributed to the emergence of off-diagonal disorder in the molecular chain.[12,13] It is well known that water molecules play a key role in the formation of *J*-aggregates: in the absence of water, *J*-aggregates are not observed.[26,27] Consequently, a small number of water molecules in a binary solution can lead to the formation of imperfect molecular chains with a random spread in separations between nearest neighbors or random relative orientation of molecules. Both factors ultimately lead to fluctuations in the

resonant dipole–dipole interaction, and hence to the emergence of off-diagonal disorder.[12,13,18,24]

In our experiments, we traced the variation of $\Delta\nu_{\mathrm{FWHM}}$ and the position of the peak of the *J*-band and the absorption band of nonassociated S120 molecules upon a variation in the composition of the glass matrix. As a result of transition from the glass matrix DMFA:B=1:1 to the glass matrix DMFA:B=1:2.5, the absorption band of individual S120 molecules was broadened by $25.4\,\mathrm{cm}^{-1}$ and shifted to the long-wave region by $45\,\mathrm{cm}^{-1}$, which is usually observed upon an increase in the polarity of dielectric glass matrices.[31,32] At the same time, the value of $\Delta\nu_{\mathrm{FWHM}}$ for the absorption band of *J*-aggregates remained practically unchanged (see Fig. 4), and the peak of the band was shifted to the long-wave region by $16\,\mathrm{cm}^{-1}$. The observed long-wave shift of the peak in the *J*-band as well as in its $\Delta\nu_{\mathrm{FWHM}}$ is apparently determined by the joint operation of two mechanisms. On the one hand, an increase in water content in the glass matrix reduces the degree of disorder in *J*-aggregates, and their exciton absorption band must be shifted to the short-wave region and become narrower.[12,13] However, on the other hand, an increase in water content leads to an increase in the overall polarity of the dielectric glass matrix, which must shift the absorption band of *J*-aggregates towards the long-wave regions in accordance with the Lippert rule[35] and its broadening. In this case, the absorption band of nonassociated molecules obeys only the Lippert rule.[35] Indeed, the *J*-band and the absorption band of nonassociated S120 molecules shifted in experiments by different values as a result of an increase in the water content in the glass matrix.

The absorption spectrum of an LB film virtually did not contain a band corresponding to nonassociated S120 molecules. The absorption band of *J*-aggregates of S120 in the LB film was asymmetric in shape (Fig. 5) and was characterized by a much larger value of $\Delta\nu_{\mathrm{FWHM}}$ than that for the glass matrix (see Fig. 4). The shape of the *J*-band could not be described correctly by an asymmetric Lorentz–Lorentz contour or by an asymmetric Gauss–Lorentz contour (see Fig. 5). In both cases, the statistical spread of the points in the experimental spectrum relative to the approximating contour noticeably deviates from the zero line (Figs. 5a and 5b). The absorption band for *J*-aggregates of PIC in a LB film[12] is described best of all by an asymmetric Lorentz–Lorentz contour, which was attributed to a considerable off-diagonal disorder. Off-diagonal disorder is also observed for *J*-aggregates of S120 obtained in a LB film, but it is smaller than in the glass matrix with a low water content (see Fig. 4). A comparison of the values of $\Delta\nu_{\mathrm{FWHM}}$ for the absorption band of *J*-aggregates in the LB film (see Fig. 5) and in the glass matrix (see Fig. 4) indicates that their diagonal disorder in the LB film is much larger.

It was noted above that the number N of coherently coupled molecules in a $1D$ system is a very important parameter determining the dynamics of exciton excitations.[12–17] The value of N for *J*-aggregates can be estimated proceeding from two independent experimentally observed quantities[12–17] since N appears in relations connecting the spectral characteristics of absorption and kinetic parameters of luminescence of nonassociated molecules and *J*-aggregates:[14]

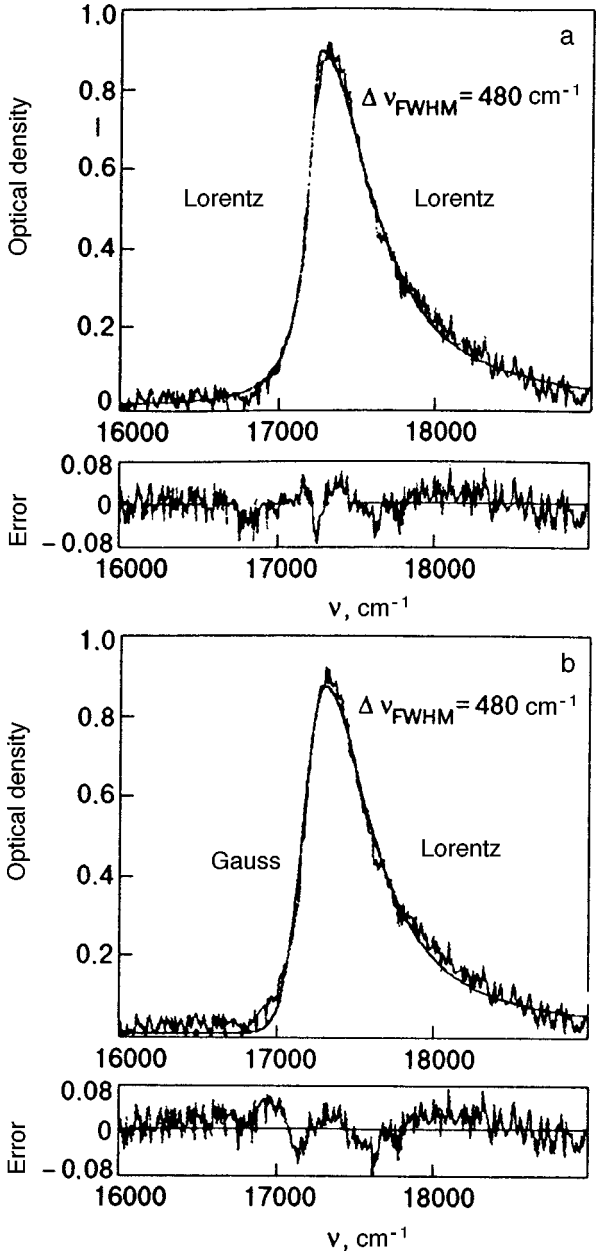

FIG. 5. Absorption band for *J*-aggregates of S120 at $T=1.5\,\mathrm{K}$ in the LB film approximated by an asymmetric Lorentz contour (a) and by a compound Gauss–Lorentz contour (b).

$$\tau_J=\pi^2\frac{\tau_M}{8N},\quad \sigma_J=\frac{\sigma_M}{\sqrt{2(N+1)/3}},\tag{1}$$

where τ_J and σ_J are the luminescence time and the full width at half maximum of the absorption band for *J*-aggregates, and τ_M and σ_M are the same quantities for nonassociated molecules.

If we use the experimental results on luminescence kinetics for *J*-aggregates of S120[10] and nonassociated S120 molecules as well as the values of $\Delta\nu_{\mathrm{FWHM}}$ for the *J*-band and absorption band for nonassociated molecules, we can substitute the following values of parameters (for the glass

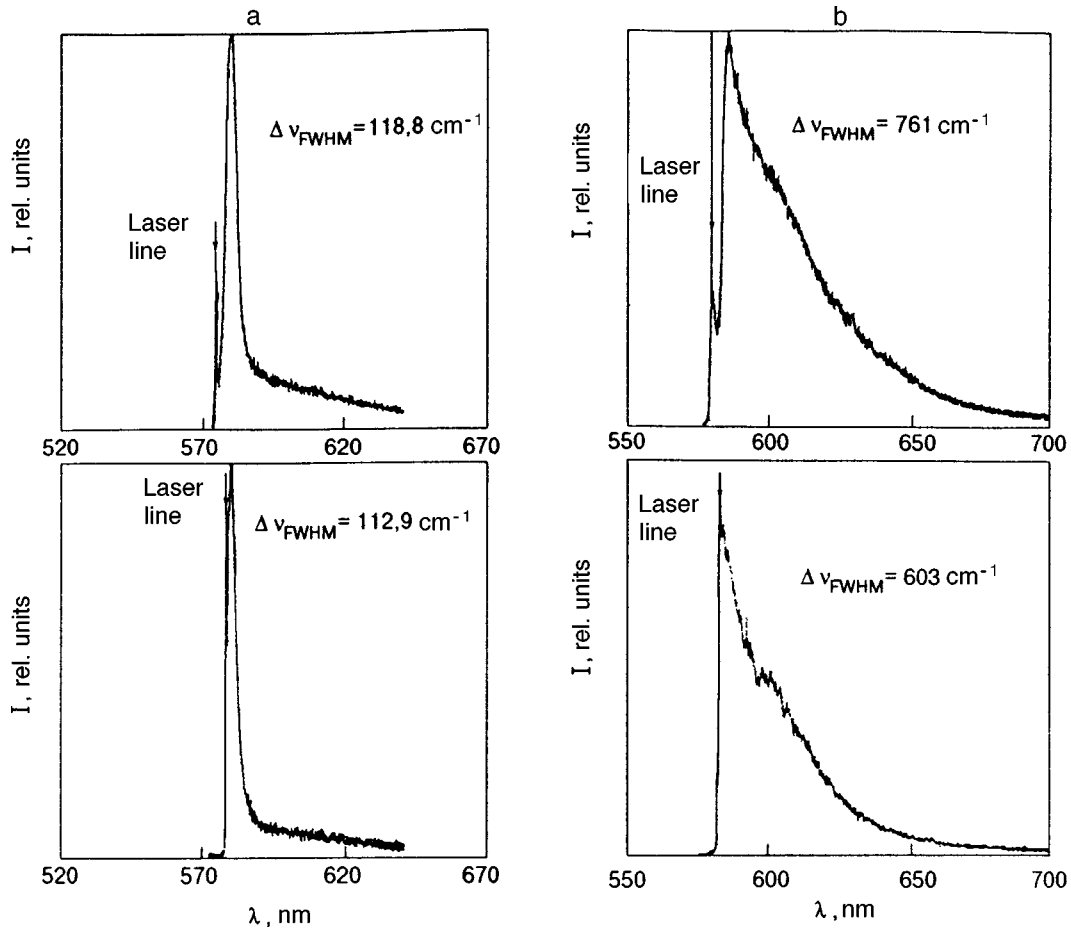

FIG. 6. Luminescence band for *J*-aggregates of S120 under selective excitation at $T=1.5$ K in the glass matrix DMFA:B=1:2.5 (a) and in the glass matrix DMFA:B=1:1 (b).

matrix DMFA:B=1:2.5) into relation (1): $\tau_J=0.12$ ns, $\tau_M=3.2$ ns, $\sigma_j=382\,\mathrm{cm}^{-1}$, $\sigma_M=1460\,\mathrm{cm}^{-1}$. It follows from the two independent relations (1) that delocalization of an exciton in *J*-aggregates of S120 at $T=1.5$ K amounts to 25–30 molecules. The number of coherently coupled molecules in a *J*-aggregate is determined by the resonant dipole–dipole interaction tending to delocalize an exciton as well as by diagonal disordering having the opposite tendency. These three parameters are connected through the following general relation[14]

$$\frac{\Delta}{V}=\frac{3\pi^2}{(N+1)^{3/2}}, \tag{2}$$

where Δ characterizes diagonal disorder and V the resonant dipole–dipole interaction.

Using formula (2) and substituting the value of N determined from (1), we obtain the average diagonal disorder in *J*-aggregates of S120 in the units of resonant dipole–dipole interaction $\Delta/V\sim0.2$ ($V\sim600\,\mathrm{cm}^{-1}$ according to the estimate obtained from the experimental spectra[10] in the nearest neighbor approximation).

Selective excitation of luminescence of *J*-aggregates to the exciton absorption band by a narrow-band ($\Delta\nu_{\mathrm{FWHM}}=0.2\,\mathrm{cm}^{-1}$) laser with a tunable frequency did not lead to a considerable narrowing of their luminescence band (Fig. 6). For the glass matrix DMFA:B=1:2.5 in which the luminescence of *J*-aggregates is mainly due to emission of free excitons,[10,11,36–39] the luminescence band was characterized by $\Delta\nu_{\mathrm{FWHM}}=118.8\,\mathrm{cm}^{-1}$ for $\lambda_B=574.4$ nm and $\Delta\nu_{\mathrm{FWHM}}=112.9\,\mathrm{cm}^{-1}$ for $\lambda_B=579.3$ nm (Fig. 6a). In the case when the luminescence band of *J*-aggregates is formed by the luminescence of free and self-trapped excitons[10,11,36–39] in the glass matrix DMFA:B=1:1, the scanning of the laser line within the absorption band of *J*-aggregates from 579.4 to 582.9 nm led to a change of $\Delta\nu_{\mathrm{FWHM}}$ of the luminescence band from 761 to $603\,\mathrm{cm}^{-1}$ (Fig. 6b). It can be seen from the figure that the narrowing of the luminescence band occurs at the long-wave edge formed by the luminescence of self-trapped excitons.[10,11,36–39]

In experiments on selective excitation (see Fig. 6), a frequency shift was always observed between the peaks of the laser line and the luminescence band of *J*-aggregates. This shift decreased and ultimately vanished when the laser line was displaced towards the long-wave edge of the absorption band of *J*-aggregates. For example, this shift for the glass matrix DMFA:B=1:2.5 was $162\,\mathrm{cm}^{-1}$ for $\lambda_B=574.4$ nm and $62.6\,\mathrm{cm}^{-1}$ for $\lambda_B=579.3$ nm. Such a shift for the glass matrix DMFA:B=1:1 was larger than for the matrix DMFA:B=1:2.5 for the excitation at the same wavelength. For example, for $\lambda_B\sim579$ nm, this shift amounted to

276.9 cm^{-1} for DMFA:B=1:1 and 62.6 cm^{-1} for DMFA:B =1:2.5 (see Fig. 6). The spectral shift of the luminescence band of *J*-aggregates under investigation was not observed for the excitation at the long-wave edge of the absorption band (to the bottom of the exciton band) (see Fig. 6b).

The absence of a considerable narrowing of the luminescence band of free excitons (see Fig. 6a) can be explained by two factors. First, the absorption of a photon in a *J*-aggregate occurs in a segment containing *N* molecules, whose length changes in each act of absorption and is localized at random over the entire physical length of the *J*-aggregate.[12,13] For this reason, a single *J*-aggregate can form the entire absorption band observed in experiments. It should be noted that the optical absorption band for simple impurity centers (ion or molecule) in dielectric matrices of various structure is an additive sum of uniformly broadened lines belonging to each impurity center separately.[30–34] However, the absorption band of an ensemble of *J*-aggregates cannot be presented as the sum of uniformly broadened spectral contours corresponding to each individual *J*-aggregate with the corresponding function of nonuniform broadening,[30–34] and hence the effect of selective excitation of luminescence in an isolated group of molecular impurity chains cannot be observed for *J*-aggregates. Second, the formed exciton preserves its mobility while migrating over the molecular chain of a *J*-aggregate. This follows from the exciton–exciton annihilation[4,40] and quenching of luminescence band of free excitons by traps.[37,39] If a laser line falls into the short-wave edge of the *J*-band, short segments of the *J*-aggregate with a large diagonal disorder are excited predominantly. However, a migrating exciton reaches segment with a lower degree of disorder, in which its energy decreases insignificantly. The peculiar properties of the absorption band for *J* aggregates mentioned above and the migration of excitons are responsible for the absence of narrowing of the luminescence line for *J*-aggregates (see Fig. 6) under selective excitation of their luminescence, which is usually observed for impurity centers in dielectric matrices.[30–34] Besides, the migration of free excitons to segments of *J*-aggregates with a smaller diagonal disorder is responsible for the shift of the peak of the luminescence band for free excitons relative to the laser line (See Fig. 6). Naturally, this shift decreases and vanishes altogether when the laser excitation line is displaced to the long-wave edge of the absorption band of *J*-aggregates.

Along with luminescent relaxation and migration, free excitons in *J*-aggregates have one more relaxation channel associated with their self-trapping.[10,11,36–38] Luminescence of self-trapped excitons forms a broad luminescence band (see Fig. 6b). Self-trapping of excitons in segments of *J*-aggregates with a higher degree of diagonal disorder (such segments are excited at the short-wave edge of the *J*-band) is more effective in view of its higher probability as well as a strong lowering of the level of a self-trapped exciton below the bottom of the exciton band. For this reason, a displacement of the laser line to the long-wave edge of the absorption band for *J*-aggregates causes an insignificant narrowing of the luminescence band in the luminescence range of self-trapped excitons (see Fig. 6b).

Thus, we have proved that the asymmetric shape of the exciton absorption band of *J*-aggregates of S120 in a glass matrix with a high water content coincides with that predicted earlier[21,22] for 1*D* systems with diagonal disordering. A change in the shape of the low-frequency edge of the absorption band for *J*-aggregates in a glass matrix with a low content of water and in a LB film is associated with the emergence of off-diagonal disorder in molecular chains. The absence of a considerable spectral narrowing of the luminescence line for *J*-aggregates under the excitation of their luminescence by a narrow-band laser is due to statistical properties of the absorption band for *J*-aggregates and the presence of nonradiative relaxation processes occurring in the excited state. The results obtained here demonstrate the possibility of controlling the type of disorder in molecular chains constructed from molecules of the same type, but by different methods and under different conditions.

The authors are grateful to V. Tkachev for his help in preparing LB films.

This research was supported by INTAS Grant (No. 96-0626).

*E-mail: malyukin@isc.kharkov.ua
**E-mail: 100520.3341@compuserve.com

[1] E. E. Jelly, Nature (London) **139**, 631 (1937).
[2] G. Scheibe, Angew. Chem. **50**, 212 (1937).
[3] D. A. Vanden Bout, J. Kerimo, D. A. Higgins, and P. F. Barbara, Acc. Chem. Res. **30**, 204 (1997).
[4] V. Sundstrom, T. Gillbro, R. A. Gadonas, and P. A. Piskarskas, J. Chem. Phys. **89**, 2754 (1988).
[5] J. Moll, S. Daehne, J. R. Durrant, and D. A. Wiersma, J. Chem. Phys. **102**, 6362 (1995).
[6] H. Fidder, J. Knoester, and D. A. Wiersma, J. Chem. Phys. **98**, 6564 (1993).
[7] H. Fidder and D. A. Wiersma, Phys. Rev. Lett. **66**, 1501 (1991).
[8] H. Fidder, J. Knoester, and D. A. Wiersma, Chem. Phys. Lett. **171**, 529 (1990).
[9] M. A. Drobizhev, M. N. Sapozhnikov, I. G. Scheblykin *et al.*, Chem. Phys. **211**, 455 (1996).
[10] Yu. V. Malyukin and O. G. Tovmachenko, JETP Lett. **58**, 393 (1993).
[11] Yu. V. Malyukin, V. P. Seminozhenko, and O. G. Tovmachenko, Zh. Éksp. Teor. Fiz. **107**, 812 (1995) [JETP **80**, 460 (1995)].
[12] H. Fidder, J. Knoester, and D. A. Wiersma, J. Chem. Phys. **95**, 7880 (1991).
[13] H. Fidder, J. Terpstra, and D. A. Wiersma, J. Chem. Phys. **94**, 6895 (1991).
[14] V. A. Malyshev, Opt. Spectrosc. **71**, 873 (1991).
[15] V. A. Malyshev, Opt. Spectrosc. **84**, 235 (1998).
[16] V. Malyshev and P. Moreno, Phys. Rev. B **51**, 14587 (1995).
[17] E. W. Knapp, Chem. Phys. **85**, 73 (1984).
[18] J. Ziman, *Models of Disorder*, Cambridge Univ. Press, Cambridge (UK) (1979).
[19] N. F. Mott, *Metal–Insulator Transition* [Russian Transl.], Nauka, Moscow (1979).
[20] S. A. Gredeskul, L. A. Pastur, and I. M. Lifshits, *Introduction to the Theory of Disordered Systems* [in Russian], Nauka, Moscow (1982).
[21] J. Klaffter and J. Jortner, J. Chem. Phys. **68**, 1513 (1978).
[22] M. Schreiber and Y. Toyozawa, J. Phys. Soc. Jpn. **51**, 1528 (1981).
[23] M. D. Feuer, in *Exciton Coherence: Spectroscopy and Dynamics of Excitations in Condensed Media* (ed. by V. M. Agranovich and R. M. Hochstrasser), Nauka, Moscow (1987).
[24] J. Knoester, J. Chem. Phys. **99**, 8466 (1993).
[25] S. Boer and D. A. Wiersma, J. Lumin. **45**, 241 (1990).
[26] A. N. Terenin, *Photonics of Molecules of Dyes and Allied Organic Compounds* [in Russian], Nauka, Leningrad (1967).
[27] A. A. Ishchenko, Usp. Khim. **60**, 1708 (1991).
[28] D. S. Chemla and I. Zyss (Eds.), *Nonlinear Properties of Organic Mol-*

ecules and Crystals, Academic Press, Orlando (USA) (1987).
[29] C. Dusehl, W. Frey, and W. Knoll, Thin Solid Films **160**, 251 (1988).
[30] I. S. Osad'ko, Phys. Rep. **206**, 45 (1991).
[31] R. Jankowiak and G. I. Small, Science **257**, 618 (1987).
[32] R. I. Personov, E. I. Al'shits, and L. A. Bykovskaya, Zh. Éksp. Teor. Fiz. **65**, 1825 (1973) [Sov. Phys. JETP **38**, 912 (1973)].
[33] R. M. Macfarlane, J. Lumin. **45**, 1 (1990).
[34] J. L. Skiner, B. B. Laird, and L. Root, J. Lumin. **45**, 6 (1990).
[35] J. Lakowics, *Principles of Fluorescence Spectroscopy*, Plenum, New York (1983).
[36] Yu. V. Malyukin, V. P. Seminozhenko, and O. G. Tovmachenko, Fiz. Nizk. Temp. **22**, 442 (1996) [Low Temp. Phys. **22**, 344 (1996)].
[37] Yu. Malyukin, Fiz. Nizk. Temp. **23**, 476 (1997) Low Temp. Phys. **23**, 351 (1997).
[38] Yu. V. Malyukin, V. P. Seminozhenko, and O. G. Tovmachenko, Zh. Prikl. Spektrosk. **62**, 104 (1995).
[39] Yu. Malyukin, O. G. Tovmachenko, and A. A. Ishchenko, Colloid Polym. Sci. **16**, 1785 (1997).
[40] S. Kobayashi and F. Sasaki, J. Lumin. **60/61**, 824 (1994).

Translated by R. S. Wadhwa

Pumping of energy into a mesoscopic ring: Exactly solvable model

L. Gorelik and S. Kulinich

Department of Applied Physics, Chalmers University of Technology and Göteborg University, S-412 96 Göteborg, Sweden[1)] *and B. Verkin Institute for Low Temperature Physics and Engineering, 310164 Kharkov, Ukraine*[2)]

Yu. Galperin

Department of Physics, University of Oslo, P.O. Box 1048 Blindern 0316 Oslo, Norway and A. F. Ioffe Institute, 194021 St. Petersburg, Russia[3)]

R. I. Shekhter and M. Jonson

Department of Applied Physics, Chalmers University of Technology and Göteborg University, S-412 96 Göteborg, Sweden[1)]

(Submitted July 13, 1998)
Fiz. Nizk. Temp. **24**, 1181–1191 (December 1998)

We consider the energy stored in a one-dimensional ballistic ring with a barrier subjected to a linearly time-dependent magnetic flux. An exact analytical solution for the quantum dynamics of electrons in the ring is found for the case when the electromotive force multiplied by the electron charge, $e\varepsilon$, is much smaller than the interlevel spacing, Δ. Electron states exponentially localized in energy space are found for irrational values of the dimensionless ratio $A \equiv \Delta/2e\varepsilon$. Relaxation limits the dynamic evolution and the localization does not develop if A is sufficiently close to a rational number. As a result the accumulated energy becomes a regular function of A containing a set of sharp peaks at rational values with small enough denominators (fractional pumping). The shape of the peaks and the distances between them are governed by the interplay between the strength of backscattering and the relaxation rate.
© *1998 American Institute of Physics.* [S1063-777X(98)00812-3]

1. INTRODUCTION

Physical properties of mesoscopic system are strongly influenced by quantum interference of electronic states.[1] Anderson localization of electrons,[2] universal fluctuations of conductance,[3] as well as periodic magnetic field dependence of thermodynamic- and transport properties of multiply connected devices (e.g., metallic rings) are important examples.

Previous extensive studies in mesoscopic physics were concentrated mainly on thermodynamics, as well as on linear response of nanostructures to dc or slowly time-varying electrical and magnetic perturbations. At the same time, relatively little is known about the *nonlinear* response of mesoscopic systems to a time-dependent bias. In general, an electron driven by an external time-dependent force does not conserve the energy. In spite of the fact that energy is not conserved, interference processes remain crucially important if the phase breaking rate is much less than the rate characterizing *dynamical* redistribution of the electron wave function between different states in energy space.

In this paper, we consider an example of such a system, namely a single-channel mesoscopic ring subjected to a nonstationary perpendicular magnetic field, linearly dependent on time. We concentrate on the energy accumulation in such a system as a function of time. To investigate the role of interference, we take into account electron backscattering from a single potential barrier (''defect''), embedded in the ring. It is shown that tuning either the time derivative of the external magnetic field variation, or the transmission amplitude through the barrier (by the gate potentials) one can influence the interference pattern, and in this way change the dynamics significantly.

Disordered conducting rings have been extensively discussed in connection with energy dissipation in mesoscopic metallic systems.[4,5] Gefen and Thouless[6,7] have suggested that randomly distributed impurities lead to the so-called *dynamical localization* of electrons in *energy space*. This phenomenon, similar to Anderson localization in real space, should exist even in ballistic rings, i.e., when the elastic mean free path is much bigger than the ring's diameter. To be more precise, the electron energy as a function of time should *saturate* rather than increase without bound (as is expected to happen in a perfectly ballistic ring without any impurities at all[8]). In the saturation regime the time-averaged electric current vanishes. Consequently, a slow-varying magnetic flux $\Phi(t)$ through the ring induces a circular slowly varying current *only in the presence of phase breaking processes*. The role of these processes was analyzed numerically in Refs. 9 and 10.

Dynamical localization in energy space, as well as Anderson localization in the real space, occurs due to *destructive interference* of partial waves with random phases forming the electron state. However, in our case the nature of the randomness is dynamic (cf. the case of so-called kicked rotator[11,12]). Consequently, the interference is crucially sen-

 © 1998 American Institute of Physics

sitive to the rate of change of magnetic flux, scattering amplitude against the barrier, etc. As was shown in Refs. 13 and 14, for certain values of $\dot{\Phi}(t)$ the energy-space propagation of the electrons can in the single-impurity case be mapped onto the real-space motion of a particle in a *periodic* potential. Such a Bloch-like state results in the conductance behavior qualitatively similar to the one of pure rings.

At the same time, according to numerical studies[10,13] the electron appears localized in energy space at other rates of magnetic flux variation; the energy pumped into the systems saturates as expected for disordered systems. This result makes the crucial importance of the rate of change of flux clear; by tuning the time derivative of the flux (i.e., the induced electromotive force in the ring) one can crossover from one regime to the other, and in this way control the energy pumping. This is the subject of the present paper.[15]

We shall show that the scenario of the crossover is as follows. Consider the conductance of the ring, G, defined as the ratio between the circulating current and the electromotive force $\mathscr{E}=-\dot{\Phi}/c$ induced in a ring of radius r_0 by a magnetic field linearly dependent on time. If scattering is strong, $G\propto\mathscr{E}^{-2}$. As the scattering strength decreases, a set of peaks in the $G(\mathscr{E})$ dependence appears. The peaks correspond to rational values p/q of the dimensionless ratio $A\equiv\Delta/2e\mathscr{E}$, where $\Delta=\hbar^2N_F/mr_0^2$. Here N_F is the number of filled electron states while m is the effective mass. The shape of the peaks as well as the distances between them are governed by an interplay between the height V of the potential barrier and the relaxation rate, ν, the maximum value of q being determined by the condition $\tau^q/q\simeq\hbar\nu/e\varepsilon$. Here $\tau\equiv\exp(-\mathscr{E}_c/\mathscr{E})$ is the effective amplitude of Zener tunneling through the energy gaps in the electron spectrum, $\mathscr{E}_c=\pi^2V^2/2\Delta e$. The peak structure near a maximum can be described by the interpolation formula

$$g=\tau^{2q}\,\frac{\hbar\nu\Delta}{(\hbar\nu)^2+(e\mathscr{E}q)^2\varepsilon^2}+\eta q^2\,\frac{\hbar\nu\Delta}{(e\mathscr{E})^2},\quad \varepsilon=A-\frac{p}{q}. \tag{1}$$

Here $g=G/G_0$, $G_0=e^2/h$, while $\eta(\varepsilon)$ is a smooth function of ε. If $|\varepsilon|\lesssim\tau^q/q^2$ the function $\eta\sim1$, beyond this region it decreases as $|\varepsilon|$ increases. As the barrier becomes more transparent, $\tau\to1$, the inter-peak distance (determined by the maximum value of q) decreases. Finally, the peaks overlap forming the conductance $g=\Delta/\hbar\nu$ independent of the barrier's properties.

To understand the result conjectured above let us consider the electron energy levels in the vicinity of the Fermi level, E_F, where the energy dispersion can be considered as linear. In a ballistic ring, one has then two sets of adiabatic energies $E_l(\Phi)$ corresponding to clock- and counterclockwise motion (Fig. 1). The scattering from the barrier opens gaps for the flux values $E_l=E_F+l\Delta/2$, $l=0,\pm1,\pm2,...$ the energy levels for clockwise and counterclockwise motion coincide. Consequently, the energy pumping into the system by a slowly varying magnetic flux can be mapped onto the one-dimensional motion of a quantum particle in the field of periodically placed scatterers (cf. Refs. 6, 7 and 13). Landau–Zener tunneling (with the amplitude τ introduced above) through the gaps corresponds to forward scattering while reflection from the gaps is similar to backscattering. The important difference from the usual impurity problem is that there is no translational invariance at an arbitrary value of the driving force $\mathscr{E}$. This invariance is only present for rational values p/q of the dimensionless ratio A.[13] In this case we arrive at a superlattice containing q ''impurities'' per unit cell. As a result, the motion along E-axis is described by q allowed bands, the ''velocity'' being $v_E\equiv\dot{E}\sim\Delta\tau^q/t_0$ (here $t_0\equiv h/e\mathscr{E}=\Phi_0/\dot{\Phi}$ is twice the time interval between two sequential Landau–Zener scattering events). Since the upper bound of the Brillouin zone is $4\pi\hbar/q\Delta$, the corresponding bandwidth for the motion along E-axis is $W\simeq v_E4\pi\hbar/q\Delta\simeq4\pi\hbar\tau^q/t_0q$. At rational values p/q of the quantity A the electron experiences $2p$ rotations around the ring while the enclosed magnetic flux changes by q quanta. As a result the «motion» of the system along E-axis can be mapped onto the motion of a quantum particle in a one-dimensional periodic potential, the corresponding eigenstates being extended. If p/q is irrational the equivalent potential is *quasi-periodic*. It turns out that in such a case the corresponding states are then localized (see below) in spite of the fact that there is no real disorder in the system. The localization length in *energy space*, $R_{\rm loc}$, can be estimated for $A=p/q+\varepsilon$, $|\varepsilon|\ll1/q$ as follows. At finite ε the phase mismatch with respect to the case of rational $A=p/q$ can be ascribed to a quasiclassical potential $U(E)=\varepsilon\alpha E$ with $\alpha=8\pi\hbar/\Delta t_0$. This potential gives rise to band bending which creates semiclassical turning points for the modes propagating along the E-axis. The localization length can be estimated as half the distance between the turning points produced by the upper and lower band edges, $R_{\rm loc}\simeq W/2\alpha|\varepsilon|=\Delta\tau^q/4q|\varepsilon|$. Consequently, the localization time is $t_{\rm loc}\sim4R_{\rm loc}/v_E\sim t_0/q|\varepsilon|$.

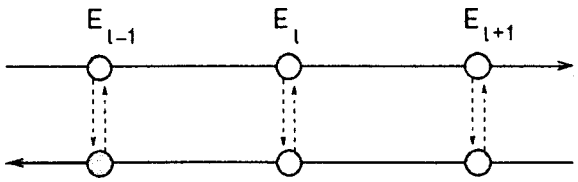

FIG. 1. Diagram showing coincidence of flux-driven energy levels (corresponding to clockwise and anti-clockwise motion of electrons around ring) at a special flux value (cf. text).

The manifestation of localization in the energy pumping depends on the product $\nu t_{\rm loc}$. At $\nu t_{\rm loc}\gg1$ localization has no chance to develop and the band picture of energy pumping is relevant. The conductance is estimated as (cf. with Ref. 7) $G=P/\mathscr{E}^2$, where P is the average energy accumulation rate. The quantity P, in its turn, is determined as $\nu(\delta E)N_{\rm eff}$. Here $\delta E\sim v_E/\nu$ is the energy accumulated by a single state, while $N_{\rm eff}(\delta E)\sim\delta E/\Delta$ is the number of involved states. It follows that $g\sim\tau^{2q}(\Delta/\hbar\nu)$. If $\nu t_{\rm loc}\ll1$, on the other hand, G is determined by hops between intraband localized states. In this case, $\delta E\sim2R_{\rm loc}$, and we obtain $g\sim\hbar\nu\Delta\tau^{2q}/(e\mathscr{E}q\varepsilon)^2$. These estimates are consistent with the first term in Eq. (1).

The paper is organized as follows. In the following section the theoretical model is described and basic expressions

for the electrical current are obtained. These expressions are analyzed and discussed in Sec. 3, the details of calculations being outlined in Appendices.

2. THEORY

A. The model

The following model is employed. The electron system is described by the Hamiltonian

$$\mathscr{H}(t,\varphi)=-\Delta\sigma_z\left(i\frac{\partial}{\partial\varphi}+\frac{t}{t_0}\right)+\mathscr{H}_{\rm imp}(\varphi). \tag{2}$$

Here σ_i are Pauli matrices. We are interested in the current, averaged over the time t_0,

$$I(t)=\frac{1}{t_0}\int_{t_-}^{t_+}dt'\ \mathrm{Tr}\,\hat{\rho}\hat{j} \tag{3}$$

where $t_\pm=t\pm t_0/2$,

$$\hat{j}\equiv(ie/\hbar)[\mathscr{H},\hat{\varphi}]$$

is the current operator. The single-electron density matrix, $\hat{\rho}$, is calculated from the equation

$$\frac{\partial\hat{\rho}}{\partial t}=\frac{i}{\hbar}[\hat{\rho},\mathscr{H}]-\nu(\hat{\rho}-f_0[\mathscr{H}(t)]), \tag{4}$$

where f_0 is the Fermi function.

B. The average current

The formal solution of Eq. (4) can be expressed in terms of the evolution operator $\hat{u}(t,t')$, which satisfies the equation

$$i\hbar\frac{d\hat{u}(t,t')}{dt}=\mathscr{H}\hat{u}(t,t')$$

with the initial condition $\hat{u}(t,t)=1$. It has the form

$$\hat{\rho}(t)=\nu\int_{-\infty}^{t}dt'\,\mathrm{e}^{\nu(t'-t)}\hat{u}(t,t')f_0[\mathscr{H}(t')]\hat{u}^+(t,t'). \tag{5}$$

The average current can be expressed through the Heisenberg operators for the current, $\hat{j}(t)$, and the velocity in energy space, $\hat{v}(t)$,

$$\hat{j}(t)=\hat{u}^+(t,0)\hat{j}\hat{u}(t,0),$$

$$\hat{v}(t)=\hat{u}^+(t,0)\dot{f}_0[\mathscr{H}(t)]\hat{u}(t,0)$$

as

$$I(t)=\frac{1}{t_0}\int_{t_-}^{t_+}dt'\int_{-\infty}^{t'}dt''\mathrm{e}^{-\nu(t'-t'')}\mathrm{Tr}[\hat{j}(t')\hat{v}(t'')]. \tag{6}$$

Using the symmetry property of the Hamiltonian (2)

$$\mathrm{e}^{i\hat{\varphi}}\hat{\mathscr{H}}(t,\varphi)\mathrm{e}^{-i\hat{\varphi}}=\hat{\mathscr{H}}(t+t_0,\varphi) \tag{7}$$

one obtains the symmetry properties of the operators $\hat{u}$, $\hat{\rho}$ and $\hat{v}$:

$$\hat{u}(t+t_0,t'+t_0)=\mathrm{e}^{i\hat{\varphi}}\hat{u}(t,t')\mathrm{e}^{-i\hat{\varphi}},$$

$$\hat{\rho}(t+t_0)=\mathrm{e}^{i\hat{\varphi}}\hat{\rho}(t)\mathrm{e}^{-i\hat{\varphi}},$$

$$\hat{v}(t+t_0)=\hat{T}^+\hat{v}(t)\hat{T}, \tag{8}$$

where operator $\hat{T}$ is

$$\hat{T}=\mathrm{e}^{-i\hat{\varphi}}\hat{u}(t_0,0). \tag{9}$$

Using (7) and (8) it is easy to prove that the average current (3) is time-independent, $I(t)=\mathrm{const}\equiv I$. Having in mind the symmetry properties (7) and (8) it is convenient to divide the integration interval $(-\infty,t')$ in (6) into the intervals $-t_0/2-mt_0<t''<t_0/2-mt_0$, $m=0,1,\ldots$. In this way one can express the average current I as

$$I=\sum_{m=0}^{\infty}\mathrm{e}^{-2\tilde{\nu}m}\ \mathrm{Tr}(\hat{T}^{-m}\hat{J}\hat{T}^m\hat{\mathscr{F}})-\mathrm{Tr}\,\hat{J}_1, \tag{10}$$

where $\tilde{\nu}\equiv\nu t_0/2$, while

$$\hat{J}=\frac{1}{t_0}\int_{-t_0/2}^{t_0/2}dt\,\mathrm{e}^{-\nu t}\hat{j}(t),$$

$$\hat{\mathscr{F}}=\int_{-t_0/2}^{t_0/2}dt\,\mathrm{e}^{\nu t}\hat{v}(t). \tag{11}$$

$$\hat{J}_1=\frac{1}{t_0}\int_{-t_0/2}^{t_0/2}dt\int_{t}^{t_0/2}dt'\,\mathrm{e}^{-\nu(t-t')}\hat{j}(t)\hat{v}(t').$$

Thus the average current is expressed in terms of the operators $\hat{J}$, $\hat{\mathscr{F}}$, $\hat{J}_1$ defined along the time interval $-t_0/2$, $t_0/2$ which are dependent on the dynamics between the successive Landau–Zener tunneling events, and by the operator $\hat{T}$ which describes the long-time dynamics. Below we shall show that long-time behavior of the system is actually determined by the eigenstates $|\beta\rangle$ and eigenvalues $\exp(i\beta)$ of the unitary operator $\hat{T}$.

C. Analysis of the operator $\hat{T}$

As was shown above, one has to analyze the unitary operator $\hat{T}$ in order to understand the long-time dynamics. Its eigenstates and eigenvalues are determined by the equation

$$\hat{T}|\beta\rangle=\exp(i\beta)|\beta\rangle. \tag{12}$$

In the following, we restrict ourselves to the case of weak scattering, i.e., we assume that the relevant matrix element V (which corresponds to a momentum transfer $\sim 2p_F$) is much smaller than the interlevel spacing, Δ. For $|V|\ll\Delta$ the impurity potential is important only near the crossings of ''clockwise'' and ''counterclockwise'' adiabatic terms, that takes place at the times $t_m=mt_0/2$. As a result of scattering, gaps are created in the adiabatic spectrum at $t=t_m$. Beyond the adiabatic approximation, these gaps can be penetrated by Landau–Zener tunneling.

Consequently, one can discriminate between rather large time intervals of ballistic evolution (with the duration $\sim t_0/2$) and small intervals of Landau–Zener tunneling. The typical duration of the later intervals is $\lesssim\sqrt{t_0\hbar/\Delta}$ (cf. with Ref. 16). Thus at $\Delta t_0/\hbar\gg 1$ the Landau–Zener tunneling is indeed essentially confined within narrow intervals and therefore can be described in terms of the scattering matrix

$$\hat{S}=\exp(i\theta_0)[\sqrt{1-\tau^2}\,\exp(i\theta_1\sigma_z)+i\tau\sigma_x]. \tag{13}$$

The physical meaning of τ is the probability amplitude for Landau–Zener ''forward scattering,'' i.e., to the transition into the state with the same angular moment while traversing the interval of non-adiabatic motion. It turns out that the quantities of interest here are independent of the phases θ_0 and θ_1. For simplicity we put $\theta_0=\theta_1=0$.

Having in mind the periodicity of φ we introduce the vector basis

$$|n,\pm\rangle\equiv\frac{e^{\pm i(N_F+n)\varphi}}{\sqrt{2\pi}}\,\mathbf{s}_\pm,\quad \mathbf{s}_+=\begin{pmatrix}1\\0\end{pmatrix},\quad \mathbf{s}_-=\begin{pmatrix}0\\1\end{pmatrix}.$$

In this representation, the operator $\hat{T}$ (9) can be treated as an operator acting on direct product n and pseudo-spin ($s\equiv\pm$) spaces,

$$\hat{T}=\sqrt{1-\tau^2}\hat{S}e^{i\pi a\sigma_z}\otimes e^{4i\pi a\hat{n}} +i\tau\sum_{\pm}\hat{S}\sigma_\pm\otimes e^{2i\pi a\hat{n}}\hat{R}_\pm e^{2i\pi a\hat{n}}. \tag{14}$$

The operators $\hat{R}_\pm$ and $\hat{n}$ are defined as

$$\hat{R}_\pm|n,s\rangle=|n\mp1,s\rangle,\quad \hat{n}|n,s\rangle=n|n,s\rangle,$$

a is the fractional part of the quantity $A=\Delta/2e\mathscr{E}$ introduced above, while $\sigma_\pm=(\sigma_x\pm i\sigma_y)/2$.

The most interesting situation is the case of weak relaxation, $\nu t_0\ll1$. This inequality means that the relaxation time is much longer than the interval between successive Landau–Zener transitions. It can be shown by a direct calculation that if this inequality is met then the operators $\hat{J}$ and $\hat{\mathscr{T}}$ acquire the form[17]

$$\hat{J}=I_0\hat{V}\otimes\delta_{n,n'},$$

$$\hat{\mathscr{T}}=\hat{V}\otimes\delta_{0,n}\delta_{0,n'},$$

where $I_0=|e|\Delta/\hbar$ is the amplitude of the persistent current while

$$\hat{V}=\frac{1}{2}(\sigma_z-\hat{S}\sigma_z\hat{S}^+)=\tau^2\sigma_z-\tau\sqrt{1-\tau^2}\sigma_y. \tag{15}$$

Under the same conditions $\mathrm{Tr}\,\hat{J}_1=I_0\tau^2$.

The unitary operator $\hat{T}$ (as it can be shown by direct calculation) possesses the properties:

$$\hat{R}_-\hat{T}\hat{R}_+=e^{-4i\pi a}\hat{T},\quad \sigma_y\hat{T}^*(-\hat{n})\sigma_y=\hat{T}(\hat{n}).$$

These properties result in the following relations between the eigenstates of the operator $\hat{T}$

$$\psi_\beta(n+m)=\psi_{\beta-4\pi am}(n),\quad m=0,\pm1,...,$$
$$\sigma_y\psi^*_\beta(-n)=\psi_{-\beta}(n). \tag{16}$$

At *irrational* values of a these relations allow one to generate a complete set of eigenstates provided ψ_{β_0} is known (see Appendix A). Hence, in this case the spectrum of $\hat{T}$ can be expressed in the form $\exp(i\beta_r^\pm)$, where

$$\beta_r^\pm=\pm\beta_0(a)-4\pi ar,\quad r=0,\pm1,\pm2,\ldots.$$

At the same time it is evident that at rational values $a=p/q$ the operator $\hat{T}$, according to (14), possesses the translational symmetry, $\hat{R}_\pm^q\hat{T}\hat{R}_\pm^{-q}=\hat{T}$. Consequently, the eigenstates of the operator $\hat{T}$ have the Bloch form while the spectrum of $\hat{T}$ can be represented by a band structure. In this case the relations (16) also generate *a complete set* of eigenstates provided structure of *one band* is known.

Using (10) and (12) one can express the average current in terms of eigenvalues and eigenfunctions of the operator $\hat{T}$

$$\frac{I}{I_0}=-\tau^2+\sum_{\beta,\beta',n}\frac{(\psi_\beta(n),\hat{V}\psi_{\beta'}(n))(\psi_{\beta'}(0),\hat{V}\psi_\beta(0))}{1-\exp[-2\tilde{\nu}+i(\beta'-\beta)]}, \tag{17}$$

where we denote (**a,b**) the scalar product in pseudo spin space.

Using the equality $\hat{V}^2=\tau^2$ originating from the definition (15) and the properties (16) of the eigenfunctions $\psi_\beta(n)$ we can express the constant τ^2 in the form

$$2\tau^2=\sum_{\beta,\beta'}|(\psi_\beta(n),\hat{V}\psi_{\beta'}(n'))|^2,$$

(for any n,n'). In the limit $\tilde{\nu}\ll1$ we get the following expression for the average current

$$\frac{I}{I_0}=\sum_\beta|\Omega_\beta|^2\frac{\tilde{\nu}}{\tilde{\nu}^2+\sin^2\Phi_\beta}, \tag{18}$$

where

$$\Omega_\beta=\sum_n(\psi_{\beta_0}(n),\hat{V}\psi_\beta(n)),\quad \Phi_\beta=\frac{1}{2}(\beta-\beta_0)$$

and $\psi_{\beta_0}(n)$ is any solution of the Eq. (12) (as follows from (16), the expression (18) does not depend on the choice of β_0).

To find the eigenstates and eigenvalues of the operator $\hat{T}$ explicitly it is convenient to introduce the operators

$$\hat{U}_\pm=\hat{I}+\frac{2e^{i\pi a/2}}{\tau}\sigma_\pm\otimes\sin\left(2\pi an-\frac{\beta\pm\pi a}{2}\right),$$
$$\hat{L}=\sigma_-\sigma_+\otimes e^{i\pi an}+\hat{S}\sigma_+\sigma_-\otimes e^{-i\pi an+i\beta/2}. \tag{19}$$

As follows from the definition (19)

$$\hat{U}_\pm^{-1}=\hat{I}-\frac{2e^{i\pi a/2}}{\tau}\sigma_\pm\otimes\sin\left(2\pi an-\frac{\beta\pm\pi a}{2}\right),$$

$$\hat{L}^{-1}=\frac{1}{\sqrt{1-\tau^2}}(\sigma_-\sigma_+\hat{S}^+\otimes e^{-i\pi an}+\sigma_+\sigma_-\otimes e^{i\pi an-i\beta/2}).$$

By direct calculations one can show that the operator $\hat{T}-e^{i\beta}$ can be rewritten in the form

$$\hat{T}=e^{i\beta}=\hat{Q}[\hat{R}_+\hat{U}_++\hat{U}_-]\hat{L}^{-1}, \tag{20}$$

where the operator $\hat{Q}$ is

$$\hat{Q}=(i\tau\hat{S}\sigma_-\otimes e^{2i\pi an}\hat{R}_-e^{2i\pi an})\hat{L}\hat{U}_-^{-1}$$
$$+(i\tau\hat{S}\sigma_+\otimes e^{2i\pi an}\hat{R}_+e^{2i\pi an})\hat{L}\hat{U}_+^{-1}\hat{R}_-.$$

From the definition (20) and Eq. (12) one obtains the equation for the auxiliary function $\mathbf{d}_\beta(n)=\hat{L}^{-1}\psi_\beta(n)$,

$$[\hat{R}_+\hat{U}_++\hat{U}_-]\mathbf{d}_\beta(n)=0,$$

which is equivalent to the set of equations for the components $d_{\pm,\beta}(n)\equiv(\mathbf{s}_\pm,\mathbf{d}_\beta(n))$. The set reads as

$$d_{\pm,\beta}(n)+d_{\pm,\beta}(n\mp1)+\frac{2e^{i\pi a/2}}{\tau}\sin\left[2\pi an-\frac{\beta\pm\pi a}{2}\right]d_{\mp,\beta}(n)=0. \quad (21)$$

Introducing the function

$$B(m)=\begin{cases} d_{+,\beta}\left(\dfrac{m}{2}\right) & \text{if } m \text{ is even} \\ d_{-,\beta}\left(\dfrac{m+1}{2}\right) & \text{if } m \text{ is odd}\end{cases} \quad (22)$$

one can reduce the set of difference equations (21) to a single equation for $B(m)$

$$B(m+1)+B(m-1)+\frac{2e^{i\pi a/2}}{\tau}\sin\left(\pi am+\frac{\beta-\pi a}{2}\right)B(m)=0. \quad (23)$$

Thus, the vector equation (12) is reduced to the scalar equation (23) for $B(m)$. Its solution allows one to determine both the eigenstates and eigenvalues of $\hat{T}$ (see Appendix B).

The results are different for the cases of rational and irrational a.

1. *Case of irrational a-values.* According to our analysis (see Appendix B)

$$\beta=\beta_r^\pm=\pm\pi a-4\pi ar, \quad r=0,\pm1,\pm2,\ldots. \quad (24)$$

At $\beta=\pi a$ the eigenstate has the form

$$\psi_{\pi a}=\frac{e^{\mp i\pi an(2n\pm1)}}{2\pi}\int_0^{2\pi}dk e^{-ik(2n-1)}\begin{pmatrix} e^{-ik+i\chi(k)} \\ e^{-i\chi(k-\pi a)}\end{pmatrix}, \quad (25)$$

where

$$\chi(k)=-\sum_{l=1}^{m1}\frac{\tau^l}{l}\frac{\cos l(k-\pi/2)}{\sin \pi al}. \quad (26)$$

The infinite series (26) converges for almost all irrational values of a, and $\chi(k)$ is an analytic function (see Appendix B). Consequently, all eigenfunctions are exponentially localized, the localization length $R_{\rm loc}$ in energy space being

$$R_{\rm loc}^2=\Delta^2[\langle\beta|\hat{n}^2|\beta\rangle-\langle\beta|\hat{n}|\beta\rangle^2]=\left(\frac{\Delta}{2}\right)^2\left[\sum_{l=1}^{\infty}\frac{\tau^{2l}}{\sin^2\pi al}+O(1)\right].$$

One can see that in the vicinity of rational values p/q of a the localization length $R_{\rm loc}$ diverges as $\Delta\tau^q/(2\pi q|a-p/q|)$ in agreement with the qualitative estimates given above.

2. *Rational values of* $a(=p/q)$. Since the problem is translationally invariant in n-space the eigenstates can be labeled by a quasi momentum $\mathscr{K}(0\leqslant\mathscr{K}<2\pi/q)$. The spectrum is now given by[18] $\beta\equiv\beta_r^\pm(\mathscr{K})$,

$$\beta_r^\pm(\mathscr{K})=2\pi a\left(r+\frac{1}{2}\right)\pm\frac{2}{q}\arcsin\left\{\tau^q\sin\frac{q}{2}(\mathscr{K}-2\pi ar+\pi)\right\}, \quad (27)$$

where $r=0,1,\ldots,q-1$.

An expression for the Bloch function $\psi_\beta(n)$ for the case of rational a-values is given in Appendix B.

D. Final results

In the *strong localization limit* $(\tilde{\nu}\to0)$ one obtains the following expression from Eq. (18) for the current (and dimensionless conductance) (see Appendix C)

$$I=I_0\tilde{\nu}\left(\frac{2}{\Delta}R_{\rm loc}\right)^2, \quad g=\pi h\nu\frac{\Delta}{(e\mathscr{E})^2}\left(\frac{2}{\Delta}R_{\rm loc}\right)^2. \quad (28)$$

Consequently, in the ''irrational'' case the average current tends to zero, when $\tilde{\nu}\to0$.

In the ''rational'' case the current can be expressed as

$$\frac{I}{I_0}=\frac{1-\sqrt{1-\tau^{2q}}}{\tilde{\nu}}+\sum_{\pm,r=0}^{q-1}d\mathscr{K}|\Omega_{r\mathscr{K}}^\pm|^2\frac{\tilde{\nu}}{\tilde{\nu}^2+\sin^2\Phi_r^\pm}, \quad (29)$$

$$\Phi_r^\pm=\frac{\beta_0^+(\mathscr{K})-\beta_r^\pm(\mathscr{K})}{2}, \quad \Omega_{r\mathscr{K}}^\pm=\sum_{n=0}^{q-1}(\phi_{\beta_0},\hat{V}\phi_{\beta_r^\pm})$$

with the help of (16) and (27). Here $\phi_{\beta_r^\pm}(n)$ is the Bloch amplitude corresponding to the eigenstate $\psi_{r\mathscr{K}}^\pm(n)$. The first term in Eq. (29) determines the contribution from the intraband transitions to the average current. Formally, it tends to infinity when $\tilde{\nu}\to0$. Consequently, *the intraband transitions determine the singular behavior of the current* in the rational case. These conclusions are in agreement with the results of numerical calculations in Ref. 13.

An exact expression for the eigenfunction $\phi_{\beta_r^\pm}(n)$ shows the limiting transition to the expression (25) as q, $p\to\infty$, $p/q=$const. The current calculated according to Eq. (29) also remains continuous. Thus, Eq. (29) (with large enough p and q) can be used as a good approximation for irrational a-values. The results of such a calculation are shown in Fig. 2.

3. DISCUSSION AND CONCLUSION

The following two assumptions have been implicitly made in our consideration: (i) the electron dynamics are governed by a linear dispersion law; (ii) the energy gaps as well as the scattering matrices $\hat{S}$ are the same for all the energy levels involved.

Assumption (i) is valid if the number of involved states (limited by the relaxation rate) is much smaller than N_F. This is the case if $(\hbar\nu/\Delta)^2(\Delta/e\mathscr{E})N_F\gg1$. The first factor in

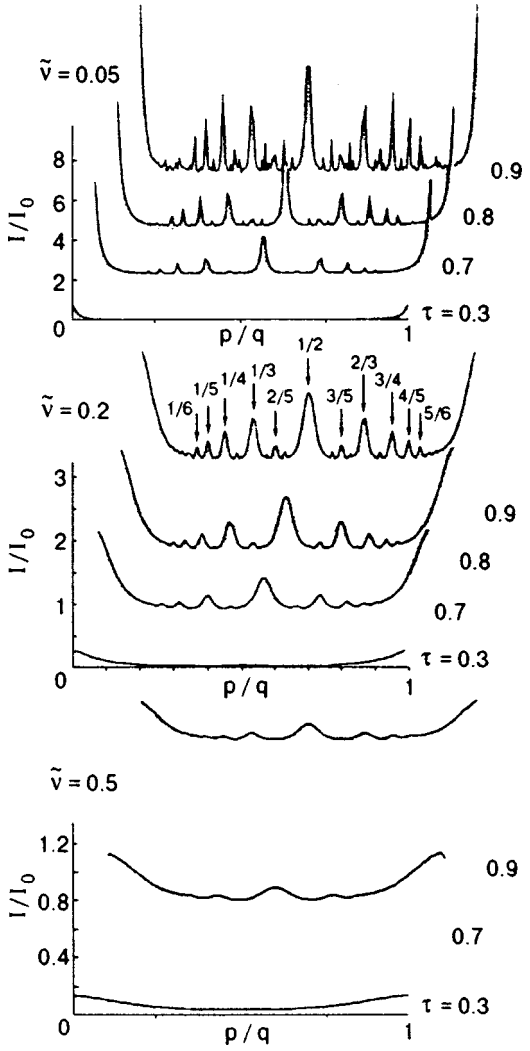

FIG. 2. The normalized current I/I_0 as a function of $a=p/q$ for different Landau–Zener tunneling amplitudes τ, $I_0=|e|\Delta/\hbar$. The values $\tilde{\nu}=0.05$ (upper panel), 0.2 (middle panel), 0.5 (lower panel) for the dimensionless relaxation rate was used. Arrows indicate the positions of maxima.

this product is small while the two others are large. However, it can be concluded that the criterion can still be met under realistic experimental conditions.

Assumption (ii) is valid if the Fourier component of the impurity (barrier) potential, $V_n \equiv \int V(\varphi) e^{2in\varphi} d\varphi$, is essentially n-independent for the relevant interval of n, $\delta n \leqslant 1/\nu t_0$. This is the case if the scattering potential is confined to a region of width $\delta\varphi \ll 2\pi\nu t_0$. Note that the inequality $\nu t_0 \ll 1$ is essential for maintaining a noticeable energy pumping.

If there are two point scatterers in the system the distance between them may be treated as the width of one barrier potential. So in the case of well separated impurities ($\delta\varphi \sim 1$) the interference from different point scatterers will generate a quasiperiodic dependence of the gaps $V_n \propto \cos(n\delta\varphi)$. This circumstance will generate an additional quasiperiodic disorder in scattering (nondiagonal disorder). The problem whether this type of disorder is enough for localizing electrons in energy space at any value of the flux rate needs further considerations. However, for an increasing number of scatterers the randomness in the energy gap distribution will increase tending to make the distribution truly random. This would strongly affect the ''fractional'' regime of energy pumping and presumably suppress the absorption peaks in Fig. 2. This crossover from the picture considered in this paper to a case of more than one scatterer is a way to introduce disorder into the problem.[6]

Another approximation is that we have allowed for relaxation in the simplest possible way by using a single relaxation time in the Eq. (4) for the density matrix. This assumption is adequate if the relaxation is caused by a transfer of the electrons in *real space* between the ring and a surrounding reservoir. If the electron energy spectrum in the reservoir is continuous, then the lifetime of an electron state in the ring with respect to this mechanism is almost independent of its quantum numbers. The mechanism discussed above allows us to describe electron states in the ring as pure quantum states, the relaxation rate being the decay through escape to the reservoir. The exact results obtained above are relevant for the case when such an «escape» mechanism dominates. Internal inelastic relaxation processes in the ring can in principle lead to a significant difference between phase- and energy relaxation rates. Such a situation requires a separate treatment. However, in the most interesting case of efficient Landau–Zener tunneling, the intrinsic inelastic processes must involve large momentum transfer and therefore they are strongly suppressed.[8]

In conclusion, the quantum electron dynamics problem in a single-channel ballistic ring with a barrier, subjected to a linearly time-dependent magnetic flux has been solved exactly. Exponential localization in energy space has been proven. Finally, we have shown that the dc-current exhibits a set of peaks with fractional structure when plotted as a function of the induced electromotive force. This structure is strongly sensitive to the barrier height, as well as to the relaxation rate.

This work was supported by the Swedish Royal Academy of Sciences (KVA), The Swedish Research Council for Engineering Sciences (TFR) and by the Research Council of Norway. We also acknowledge partial financial support from INTAS Grant No 94-3862.

APPENDIX A

To prove that the functions $\{\psi_\beta(n)\}$ form a complete set it is necessary to check the Parseval identity

$$\sum_{r,\pm} [\psi_r^{\pm}(n)]^* \otimes \psi_r^{\pm}(n') = \delta_{n,n'} \hat{I}. \tag{A1}$$

As it follows from Eq. (16),

$$\psi_r^{\pm}(n) = \psi_n^{\pm}(r), \quad \psi_{-r}^{+}(r) = \sigma_y [\psi_r^{-}(-n)]^*.$$

Therefore, one arrives at the set of equalities

$$\sum_r [\psi_r^-(n)]^* \otimes \psi_r^-(n') = \sigma_y \sum_r \psi_r^+(-n) \otimes [\psi_r^+(-n')]^* \sigma_y$$

$$= \sigma_y \sum_r \psi_r^+(n') \otimes [\psi_r^+(n)]^* \sigma_y$$

$$= \sigma_y \left\{ \sum_n [\psi_r^+(n)]^* \otimes \psi_r^+(n') \right\}^T \sigma_y .$$

Having in mind, that

$$\hat{X} + \sigma_y \hat{X}^T \sigma_y = \hat{I} \ \mathrm{Tr}\ \hat{X},$$

one finally obtains

$$\sum_{r,\pm} [\psi_r^{\pm}(n)]^* \otimes \psi_r^{\pm}(n') = \hat{I} \sum_r \ \mathrm{Tr}[\psi_r^+(n)]^* \otimes \psi_r^+(n')$$

$$= \hat{I} \sum_r (\psi_n^+(r), \psi_{n'}^+(r)) = \delta_{n,n'} \hat{I}.$$

In this way the Parseval identity (A1) is proved.

APPENDIX B

We search for a solution of (23) in the form

$$B_\beta(n) = \mathrm{e}^{-i\pi a n^2/2} \int_0^{2\pi} dk\, \mathrm{e}^{-ikn} u_\beta(k). \tag{B1}$$

Substituting (B1) into (23) one gets the following equation for the 2π-periodic function $u_\beta(k)$:

$$u_\beta(k+\pi a) = \mathrm{e}^{i\lambda + iG(k+\lambda/2)} u_\beta(k-\pi a), \tag{B2}$$

where

$$G(k) = -i \ln \frac{1 - i\tau \mathrm{e}^{-ik}}{1 + i\tau \mathrm{e}^{ik}}, \quad \lambda \equiv \beta - \pi a. \tag{B3}$$

The ways to solve (B2) are different for irrational or rational a.

a) Irrational a

In this case one can look for the solution of (B2) in the form

$$u_\beta(k) = \exp[ikr + i\chi_\beta(k)]$$

where $\chi_\beta(k)$ is 2π-periodic continuous function and r is the arbitrary while number. $\chi_\beta(k)$ is determined by the following difference equation with constant coefficients:

$$\chi_\beta(k+\pi a) - \chi_\beta(k-\pi a) = \lambda - 2\pi a r + G(k+\lambda/2). \tag{B4}$$

This equation has solutions if and only if the right part is orthogonal to all the solutions of uniform equation

$$f(k+\pi a) - f(k-\pi a) = 0. \tag{B5}$$

If a is an irrational number one can easily check that there is only one solution of Eq. (B5) within the class of integrable functions, namely $f(k) = \mathrm{const}$. Keeping this fact in mind we integrate both parts of (B4) over the variable k from $-\pi$ to π to find the value of λ at which the solution of (B4) exists. Substituting (B3) for $G(k)$ we get $\lambda = \lambda_r = 2\pi a r$ and, as a consequence, the expression (24) for the eigenvalues of operator $\hat{T}$.

Solving Eq. (B4) at $\lambda = \lambda_r$ by the Fourier method, one gets the following expression for the function $\chi(k) = \chi_r(k)$

$$\chi_r(k) = -\sum_{l=1}^{\infty} \frac{\tau^l}{l} \frac{\cos\, l(k - \pi a r - \pi/2)}{\sin\, \pi a l}. \tag{B6}$$

It is known (see, e.g., Ref. 19) that *for almost all* irrational numbers a (that means excluding a set of irrational numbers of zero measure) the inequality $|a - p/q| > C/q^2$ can be satisfied. Here p, q are integer numbers, while C depends only on a. One can show that this inequality leads to a convergence of the series (B6) *for almost all* a. As a result, the function $u_\beta(k)$ can be analytically continued into the region

$$\ln \tau < \mathrm{Im}\ k < -\ln \tau.$$

Because of that the function $B_\beta(n)$ given by (B1) decays as a $\tau^{-|n|}$ at $n \to \pm\infty$, and therefore the eigenstates of operator $\hat{T}$ are *exponentially localized*.

b) Rational $a = p/q$

In this case Eq. (23) is symmetric with respect to translation $n \to n + 2q$. Therefore its solution has the Bloch form, and as a consequence the function $u_\beta(k)$ defined by (B1) appears singular. Thus at rational $a = p/q$ one can look for the solution of (B2) in the form

$$u_\beta(k) = \exp[ikr + i\zeta(k)] \times \sum_{m=0}^{q-1} \delta\left(\sin\left[\frac{k}{2} + \frac{\mathscr{K}}{4} - \pi a m + \frac{\pi a}{2} \right] \right), \tag{B7}$$

$\delta(x)$ is a delta function. Substituting this anzatz into the (B2) and using the relationship

$$\sum_{m=0}^{q-1} \delta\left[\sin\left(\frac{x}{2} - \pi a m \right) \right] = \sum_{m=0}^{q-1} \delta\left[\sin \frac{x}{2} + \pi a - \pi a m \right],$$

we reconstruct it as

$$\mathscr{D}\{\zeta\} \sum_{m=0}^{q-1} \delta\left(\sin\left[\frac{k}{2} + \frac{\mathscr{K}}{4} - \pi a m \right] \right) = 0,$$

$$\mathscr{D}\{\zeta\} \equiv \exp\, i\zeta(k + \pi a) - \exp\, i\Big[\zeta(k - \pi a) + \lambda - 2\pi a r + G_0\left(k + \frac{\lambda}{2} \right) + \Lambda\left(\frac{\lambda - \mathscr{K}}{2} \right) \Big], \tag{B8}$$

where

$$G(k) = G_0(k) + \Lambda(k),$$

$$\Lambda(k) = \frac{1}{2\pi} \sum_m \int_0^{2\pi} dk'\, \mathrm{e}^{-imq(k-k')} G(k')$$

$$= \frac{2}{q} \arctan \frac{\tau^q \sin\, q(k - \pi/2)}{1 - \tau^q \cos\, q(k - \pi/2)}.$$

To obtain (B8) we used the fact, that

$$\left\{\exp i\Lambda\left(k+\frac{\lambda}{2}\right)-\exp i\Lambda\left(\frac{\lambda-\mathscr{K}}{2}\right)\right\} \times\sum_{m=0}^{q-1}\delta\left[\sin\left(\frac{k}{2}+\frac{\mathscr{K}}{4}-\pi am\right)\right]=0.$$

From Eq. (B8) one can see that it is enough to find $\zeta(k)$ to satisfy the equation $\mathscr{D}\{\zeta\}=0$ and therefore, similarly to the case of irrational a, the problem is reduced to a difference equation with constant coefficients,

$$\zeta(k+\pi a)-\zeta(k-\pi a) =\lambda-2\pi ar+G_0\left(k+\frac{\lambda}{2}\right)+\Lambda\left(\frac{\lambda-\mathscr{K}}{2}\right). \tag{B9}$$

At rational $a=p/q$ Eq. (B5) has the solution $f(k)=\exp ilqk$, $l=0,\pm1,\pm2,...$. Consequently, the r.h.s. part of Eq. (B9) must be orthogonal to this function rather than to a constant as in the case of irrational a. One can check that the integral of the r.h.s. part of (B9) times $f(k)=\exp(ilqk)$, $l\neq0$ vanishes for any λ. Integrating Eq. (B9) over k one gets the dispersion equation for $\lambda(\mathscr{K})$,

$$\lambda-2\pi ar+\Lambda\left(\frac{\lambda-\mathscr{K}}{2}\right)=0. \tag{B10}$$

If $\lambda(\mathscr{K})$ satisfies this equation, the solution of (B9) is

$$\zeta_r(k)=-{\sum_{l=1}^{\infty}}' \frac{\tau^l}{l}\frac{\cos\, l(k-\pi ar-\pi/2)}{\sin\,\pi al}. \tag{B11}$$

Here the prime indicates that the terms with $l=mq$, $m=1,2,...$ are omitted.

From (B10) one gets the following expression for $\lambda=\lambda_r(\mathscr{K})$:

$$\lambda_r(\mathscr{K})=2\pi ar+\frac{2}{q}\arcsin\left[\tau^q\,\sin\frac{q}{2}\,(\mathscr{K}-2\pi ar+\pi)\right], \tag{B12}$$

for $r=0,1,...,q-1$ and, as a consequence, the expression (27) for $\beta_r(\mathscr{K})$.

The expression for the Bloch function $\psi(n)$ corresponding to the eigenvalue $\lambda_{r=0}(\mathscr{K})\equiv\lambda(\mathscr{K})$, has the form

$$\psi(n)=e^{i\mathscr{K}n\mp i\pi an(2n\pm1)} \times\sum_{m=0}^{q-1} e^{-4i\pi amn+i\xi_m^-}\begin{pmatrix} f^+(\mathscr{K})e^{-i\xi_m^-+i\zeta(\xi_m^+)} \\ f^-(\mathscr{K})e^{-i\zeta(\xi_m^--\pi a)}\end{pmatrix}, \tag{B13}$$

where

$$\xi_m^{\pm}(\mathscr{K})=-\frac{\mathscr{K}}{2}+2\pi am\pm\frac{\lambda(\mathscr{K})}{2},$$

$$f^{\pm}(\mathscr{K})=\left[1\pm\tau^q\frac{\cos\, q(\mathscr{K}+\pi)/2}{\cos\, q\lambda(\mathscr{K})/2}\right]^{1/2}$$

and $\zeta(k)\equiv\zeta_{r=0}(k)$ is defined by Eq. (B11). In the limit p, $q\to\infty$ $p/q=$const one gets the expression (25) for the case of irrational a.

Thus, the expressions (B11), (B12), and (B13) together with (22) provide $2q$ eigenstates of the operator $\hat{T}$ for a given value of $\mathscr{K}$ which plays the role of quasimomentum. Consequently, one obtains the complete set of eigenfunctions of operator $\hat{T}$ while $\mathscr{K}$ scans the interval $0\leqslant\mathscr{K}<2\pi/q$.

APPENDIX C: LIMIT OF STRONG LOCALIZATION

To provide the strong localization limit ($\tilde{\nu}\to0$), one formulates the following statements.

Lemma 1: For unitary operator $\hat{P}$, defined according to

$$\hat{P}=\hat{S}\sigma_+\otimes e^{2i\pi a\hat{n}}+\hat{S}\sigma_-\otimes e^{i\pi a\hat{n}}\hat{R}_-e^{i\pi a\hat{n}},$$

there is the following operator equality

$$\hat{P}^+\hat{T}\hat{P}=e^{2i\pi a}\hat{T}.$$

Consequently, operator $\hat{P}$ translates one of the eigenstates of the operator $\hat{T}(|\beta\rangle)$ to another state, $|\beta+2\pi a\rangle$.

Lemma 2: The operators $\hat{T}$, $\hat{n}$, $\hat{P}$, $\hat{V}$ defined above, meet the operator equality

$$\hat{V}=\hat{P}^+\hat{n}\hat{P}-\hat{T}\hat{P}^+\hat{n}\hat{P}\hat{T}^+$$

(the proof can be obtained by direct substitution).

Basing on these statements one can express the matrix element Ω_β in Eq. (18) as

$$\Omega_\beta=\langle\beta_0,\hat{V}\beta\rangle=[1-e^{i(\beta_0-\beta)}]\langle\beta_0,\hat{P}^+\hat{n}\hat{P}\beta\rangle =[1-e^{i(\beta_0-\beta)}]\langle(\beta_0+2\pi a),\hat{n}(\beta+2\pi a)\rangle.$$

Consequently, we can rewrite the Eq. (18) for the average current in the form

$$\frac{I}{I_0}=4\sum_\beta|\tilde{\Omega}_\beta|^2\frac{\tilde{\nu}\,\sin^2\,\Phi_\beta}{\tilde{\nu}^2+\sin^2\,\Phi_\beta}, \tag{C1}$$

where

$$\tilde{\Omega}_\beta=\sum_n\,(\psi_{\beta_0}(n),\hat{n}\psi_\beta(n)).$$

Therefore, in the strong localization limit one has

$$\frac{I}{I_0}=4\tilde{\nu}\sum_{n,\beta\neq\beta_0}(\psi_{\beta_0}(n),\hat{n}\psi_\beta(n))(\psi_\beta(n),\hat{n}\psi_{\beta_0}(n)) =\tilde{\nu}\left(\frac{2}{\Delta}R_{\rm loc}\right)^2.$$

[1)]E-mail: gorelik@fy.chalmers.se
shekhter@fy.chalmers.se
jonson@fy.chalmers.se
[2)]E-mail: kulinich@ilt.kharkov.ua
[3)]E-mail: iouri.galperin@fys.uio.no

[1] Y. Imry, *Quantum Coherence in Mesoscopic Systems, Vol. 254 of NATO Advanced Study Institute, Series B: Physics*, Plenum, New York (1991).
[2] P. W. Anderson, Phys. Rev. **109**, 1492 (1958).
[3] B. L. Al'tshuler, JETP Lett. **41**, 648 (1985).
[4] M. Büttiker, Y. Imry, and R. Landauer, Phys. Lett. **A96**, 365 (1983).
[5] R. Landauer, Phys. Rev. B **33**, 6497 (1983).
[6] Y. Gefen and D. Thouless, Phys. Rev. Lett. **59**, 1752 (1987).
[7] Y. Gefen and D. J. Thouless, Philos. Mag. **56**, 1005 (1987).

[8] T. Swahn, E. N. Bogachek, Yu. M. Galperin, M. Jonson, and R. I. Shekhter, Phys. Rev. Lett. **73**, 162 (1994).
[9] E. Shimshoni and Y. Gefen, Annals of Physics **210**, 16 (1991).
[10] R. Hübner and R. Graham, Phys. Rev. B **53**, 4870 (1996).
[11] G. Casati, B. V. Chirikov, F. M. Izrailev, and J. Ford, in *Stochastic Behaviour in Classical and Quantum Hamiltonian Systems*, G. Casati and J. Ford (Eds.), Lecture in Physics, Vol. 93, Springer, Berlin (1979), p. 334.
[12] D. R. Grempel, S. Fishman, and R. E. Prange, Phys. Rev. A **29**, 1639 (1984).
[13] G. Blatter and D. A. Browne, Phys. Rev. B **37**, 3856 (1988).
[14] P. Ao, Phys. Rev. B **41**, 3998 (1990).
[15] A brief account of these ideas has been published: L. Y. Gorelik, S. Kulinich, Yu. Galperin, R. I. Shekhter, and M. Jonson, Phys. Rev. Lett. **78**, 2196 (1997).
[16] L. D. Landau, Phys. Z. **2**, 46 (1932); C. Zener, Proc. R. Soc. London **A137**, 696 (1932); K. Mullen, E. Ben-Jacob, Y. Gefen, and Z. Schuss, Phys. Rev. Lett. **62**, 2543 (1989).
[17] When integrating over time in (11) we exclude small time intervals of order $\sqrt{t_0\hbar/\Delta}$ near the points $-t_0/2$, 0, $t_0/2$, where the commutator $[\mathscr{H}(t),\mathscr{H}(t')]$ does not vanish.
[18] This expression was derived for $q=1$ in Ref. 13.
[19] See for example J. W. S. Cassels, *An Introduction to Diophantine Approximation*, Cambridge University Press (1957).

This article was published in English in the original Russian journal. It was edited by R. T. Beyer.

LATTICE DYNAMICS

Structure and microhardness of low pressure polymerized fullerite C_{60}

A. P. Isakina, S. V. Lubenets, V. D. Natsik, A. I. Prokhvatilov, M. A. Strzhemechny, L. S. Fomenko, and N. A. Aksenova

*B. I. Verkin Institute for Low Temperature Physics and Engineering, National Academy of Sciences of Ukraine, 47 Lenin Ave., 310164 Kharkov, Ukraine**)

A. V. Soldatov

*Department of Experimental Physics, Umea University, S-90187 Umea, Sweden***)

(Submitted June 29, 1998, revised July 27, 1998)
Fiz. Nizk. Temp. **24**, 1192–1201 (December 1998)

We have carried out low-temperature x-ray diffraction studies on C_{60} fullerite polymerized by low quasi-hydrostatic pressure of 1.1 GPa at $T=563$ K. It is established that at room temperature in freshly prepared samples three phases mainly coexist, viz. a compressed cubic phase with the lattice parameter $a=13.94$ Å, an orthorhombic O′ phase with the lattice parameters $a=9.12$ Å, $b=9.82$ Å, $c=14.60$ Å, and a rhombohedral phase of symmetry $R3m$ with the parameters $a=9.20$ Å and $c=24.27$ Å. Mechanical grinding or annealing at 573 K entails depolymerization of sintered samples and restoration of the fcc structure of pristine C_{60}. During annealing in air, intercalation of fullerite lattice by oxygen molecules occurs as well as a substantial amount of some new phase is formed, most probably with tetragonal symmetry, the chemical composition and structure of which have not been determined. The microhardness of polymerized C_{60} is higher than that of single crystal samples roughly four-fold at room temperature and by a factor of 2.6 at liquid nitrogen temperature. Analysis shows that polymerization and grain boundaries give contributions to the microhardness of sintered samples but we did not succeed in separating these two contributions. The temperature dependence of the microhardness of polymerized samples exhibits a jump in the vicinity of 260 K, where pristine C_{60} fullerite undergoes the fcc-sc phase transition. We think that this jump is due to a partial destruction of the polymerized state under indentor as a result of shear straining in inhomogeneous stress fields. Annealing of polymerized C_{60} at a temperature of 573 K, which restores the fcc phase, leads to a considerable decrease in microhardness, the hardness ''jump'' near the fcc-sc transition extends in temperature and shifts to lower temperatures. © *1998 American Institute of Physics.* [S1063-777X(98)00912-8]

1. INTRODUCTION

Pure fullerite C_{60}, the molecules of which are bound by weak van der Waals forces, is orientationally disordered at room temperature and normal pressure with a face-centered (fcc) lattice of space symmetry $Fm3m$. At $T=260$ K, a phase transition occurs to a partially ordered phase with a cubic lattice of lower symmetry, $Pa3$.[1]

Exposure of thin C_{60} films to visible or ultraviolet radiation[2,3] as well as to high pressures and temperatures of bulk samples of C_{60}[4–10] results in polymerization of C_{60}. In the polymerization process the nearest neighbor molecules of C_{60} connect into linear chains, four- or six-member rings by double bonds of the hexagonal faces through 2,2 cycloaddition reaction.[4,8–10] This gives rise to one-dimensional orthorhombic, two-dimensional tetragonal and two-dimensional rhombohedral phases, respectively. The samples can develop one or more phases depending on external factors. Qualitative analysis, which *per se* is not a simple problem, is quite often even more difficult because of a pronounced texturing of the separate phases.[10] The polymeric phases formed survive, when irradiation is turned off or external pressure is relieved. Also, a rather short annealing (2–3 hours) at comparatively low temperatures ($T=523$ K) leads, as a rule, to depolymerization and restoration of the fcc structure typical of pristine fullerite C_{60}.

Despite the great number of research works on the development of polymerization technology in bulk polycrystal specimens, the properties of each of the polymeric phases, and the $P-T$ diagram of fullerite, and many other important questions still remain to be answered. In particular, these are the influence of thermobaric conditions in the preparation of sintered samples on their final phase composition and phase structures, homogeneity of the polymeric state at different stages of its formation [especially, under low pressures (~1 GPa) and at moderate temperatures up to 573 K], mechanical and other physical properties.

In this paper we used powder x-ray diffraction and

 © 1998 American Institute of Physics

structure-sensitive microindentation to study C_{60} fullerite samples polymerized by low pressure and then depolymerized by mechanical destruction or thermal treatment (low-temperature annealing). The structure, the lattice parameters of separate phases, the surface morphology and microhardness are studied within the range from liquid-nitrogen to room temperature.

2. EXPERIMENTAL

The samples under consideration were prepared from 99.98% pure pristine fullerite C_{60} by sublimation. The sample powder was subjected to hydrostatic compression up to 1.1 GPa using the technique close to that of Ref. 11. After that it was kept at 563 K for five hours, then cooled down to room temperature and the pressure was removed. As it follows from the results in Ref. 11, such a treatment must lead to polymerization of fullerite. Indirect evidence that the polymerization of the samples was fairly complete was their insolubility in solvents (for example, in benzene), where pristine C_{60} dissolves.

The x-ray diffraction studies and the measurements of microhardness were carried out on fragments of the sintered materials. The flat surfaces of these samples of typical size 5×5 mm served as the reflecting surface in the x-ray studies. These were also used to measure microhardness at room temperature.

The initial macroscopic flat surface of a sample was actually somewhat rough. Therefore, for low temperature measurements, when there was no possibility of finding an area suitable for indenting and the pricks were to be made blindly, the sample surface was polished. The polishing was repeatedly conducted in a mechanochemical way with benzene-wetted suede. The layer removed from the sample in a single run of polishing was 5–15 μ thick, i.e., several times larger than the depths of indentation dips in the preceding experiment. The total number of microhardness measurements performed on a sample at different temperatures was approximately 200.

The next cycle of measurements was carried out on samples subjected to mechanical or thermal treatment which, as suggested in,[12] should produce destruction of the polymerized state. To measure the microhardness and to perform the preliminary x-ray diffraction studies, a sinter fragment was annealing in air at $T=573$ K for three hours. For another series of x-ray experiments some samples were powdered and measured without any annealing or after annealing at 573 K for two hours.

The x-ray diffraction experiments were made in CuK_α radiation. The polymerized samples of C_{60} were studied at temperatures ranging from 80 to 300 K, the stabilization at every temperature point being better than ±0.05 K. To obtain reliable data on phase composition, phase structure, and lattice parameters at separate reference points (80, 120, 175, 293 K), the x-ray diffraction patterns were recorded over a wide range of reflection angles ($2\Theta=8-150°$). At other temperatures the records were taken within a limited angle range covering the most intense x-ray reflections. In addition to the reflections from the samples, the x-ray patterns contain lines from the reference material (electrolytically pure copper). Use of the reference material made it possible to reduce the error in the lattice parameters of separate phases, which is particularly important when studying their temperature dependencies. However, because of the multiphase state of the samples studied the error in the lattice parameters of the phases observed was somewhat higher ($\pm0.05\%$) than that for pristine fullerite.

The microhardness was measured in the 80–300 K temperature range by the technique described in Ref. 13. The Vickers microhardness H_V was calculated from the expression:

$$H_V=1.854P/(2a)^2, \tag{1}$$

where $2a$ is the diagonal length of an indentation, P is the indentor load. At room temperature the indentor load was 0.01 and 0.2 N. The temperature dependence of H_V was studied at $P=0.1$ N. The results obtained were produced by standard statistical methods.

3. RESULTS AND DISCUSSION

3.1. X-ray diffraction studies

Phase composition and phase structure. The range of pressures 1 to 2 GPa and temperatures 500–650 K is an intermediate one as far as the polymerization conditions of fullerite C_{60} are concerned. Usually, several phases start to form here simultaneously (orthorhombic, tetragonal, rhombohedral, and other), which can be strongly disordered in polymer chain length and orientation. The extent of polymerization and the structure of the respective phases, in addition to temperature and pressure, are controlled by other factors, viz., hydrostaticity, the rates of heating and/or compression, exposure time at the extreme conditions, grain size, and so forth. The randomness of the forming phases are to a large measure determined[14] by the fact that the polymerization process takes place in the fcc phase where, due to the almost free molecular rotations, there are no preferable directions for establishing covalent bonds. Owing to the joint effect of all the above-enumerated factors, the orthorhombic phase that forms at relatively low pressures differs in structure and lattice parameters from that found at higher pressures (the low-pressure orthorhombic phase is now conventionally called O′[14]). We shall return to this intermediate phase when discussing our own results. According to Agafonov *et al.*,[15] the lattice parameters of the O′ phase are $a=9.1$ Å, $b=9.8$ Å, $c=14.7$ Å for polycrystal samples and, according to Moret *et al.*,[16] $a=9.14$ Å, $b=9.90$ Å, $c=14.66$ Å for single crystals.

Below we analyze our x-ray powder diffraction results taking into account the above facts. A general view of the most typical diffraction patterns obtained at room temperatures, is shown in Fig. 1. The sample contains several crystal phases and a minor amount of highly dispersed or amorphous phase ($\sim10\%$ of the total sample volume), as evidenced by the broad halo at reflection angles $2\Theta=14-26°$, (which corresponds to $\sin\Theta/\lambda=(7-13)\cdot10^{-2}$).

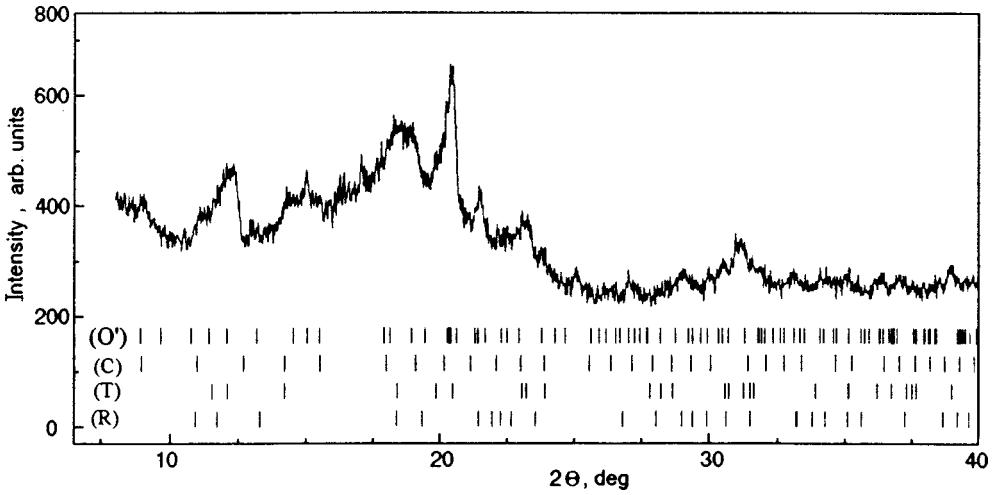

FIG. 1. Experimental powder x-ray diffraction pattern of polymerized C_{60} sample under study and calculated x-ray pattern (the peak positions) for the simple cubic (C), simple orthorhombic (O′), tetragonal (T) and rhombohedral (R) of space group symmetries *Immm* and $R3m$, respectively, phases. The lattice parameters for C, O′, R, T phases are taken from Refs. 4, 8, and 14.

No detailed analysis of the dispersed phase has been made. It should be noted that the amount of this phase remained almost unchanged in all the experiments.

The coherent reflections of the diffraction pattern is formed by the scattering from at least three phases, viz., orthorhombic (O′), rhombohedral (R), and cubic (C). At the same time we do not rule out the tetragonal (T) phase, whose reflections in angular positions coincide partially with those from the O′ and R phases. Such a composition of the samples polymerized as indicated above corresponds to a ''mix'' region in the (P,T) space where all the phases involved can coexist, as suggested by Sundqvist,[14] on the basis of all the currently available experimental data. It is rather difficult to separate and analyze reliably every individual phase, with the exception perhaps of the cubic one, in view of the fact that a very large number of broad reflections from these phases are superimposed one on another. Among the whole set of reflections, only a few weak ones can be readily assigned as pertaining to the cubic and no other phase. Estimation of lattice parameter of this phase yields a low value, $a=13.94$ Å, which corresponds to a lattice strongly compressed as compared to pristine fullerite. A possibility for such a phase was previously discussed in the literature for samples subjected to high-pressure treatment;[4,5,11,14] this phase is presumably a partially polymerization state with randomly distributed dimers, short chains, etc. Partial polymerization leads to enhanced interaction and smaller lattice parameters; we estimate the corresponding effective interval pressure to be about 0.1 MPa.

Separation of other phases was carried out by comparing the room-temperature patterns with the line-spectra calculated for all the phases known for polymerized fullerite. The relevant line spectra are given in Fig. 1. As the source data we took calculated lattice parameters for the R and T phases from,[8] for the O′ phase from,[14] and for the cubic phase from.[4] Then the lattice parameters were refined, using the whole set of experimental reflections. The calculated line diagrams for the R and T phases were constructed using the specific models[8] for the structures of space group symmetries $R3m$ and *Immm*, respectively, which are commonly accepted for the ''high-pressure'' polymeric phases. Since the space groups for both C and O′ phases have not been clearly established, the line diagrams for these phase in Fig. 1 are plotted without any absence rules. The line spectra in Fig. 1 correspond to the refined lattice parameter values, which at room temperature are: $a=9.12$ Å, $b=9.82$ Å, $c=14.60$ Å for the orthorhombic O′ phase, and $a=9.20$ Å, $c=24.27$ Å for the rhombohedral phase (in hexagonal setting). These values are in reasonable agreement with the available data known in the literature for partially or completely polymerized phases. An additional indication that the polymerization of the samples was sufficiently complete was the lack of any peculiar features in the temperature dependencies of the x-ray diffraction reflection angles or the interplane separations within the 80–293 K range that could be signatures of the phase transition observed in pristine C_{60}.

A major part of the structure results presented here has previously been reported at the 1997 Joint International Meeting in Paris.[17] When indexing the diffraction pattern there we used the assumption that, in addition to the rhombohedral phase, our samples contain a tetragonal component. One of the arguments for that conclusion was the fact that the formal statistic of the r.m.s. procedure for the T phase was noticeably better than for the orthorhombic (O) one. And moreover, according to accepted notions, the T phase is situated much ''closer'' to the sample preparation conditions than the complete O phase. However, we must admit that our samples correspond to a certain intermediate polymerized state with far from complete phases (or phase), which are clearly understood ''limit'' phases with complete polymerization within planes (111) or (100), or along directions (110). To all appearance, the ''path'' from the fcc phase to the tetragonal one inevitably ''passes'' the orthorhombic stage, the gradual crossover from the O to T phase being implied as the appearance of ''closing jumpers'' across the polymeric chains within plane (100).[1)] The polymeric ''jumpers'' will be randomly distributed so that the phase will remain orthorhombic on the average, approaching the tetragonal one as the number of crossing jumpers increases.

The relative content of the polymerized phases was evaluated from the intensity ratios and the angular positions of the observed set of reflections and under the assumption of no texture in the samples under study. To within 5% the relative amount of the O′ and R phases are 0.55:0.45.

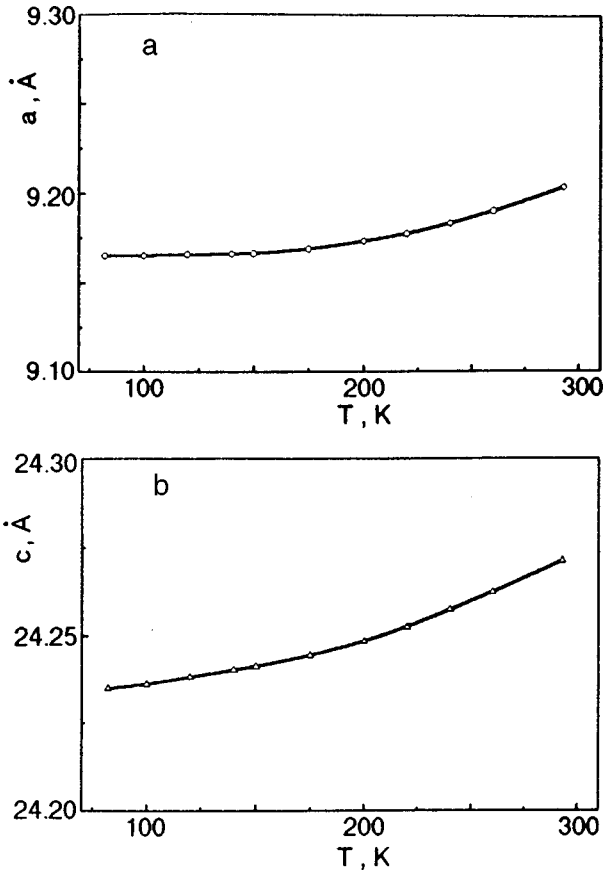

FIG. 2. Temperature dependence of the lattice parameters *a* and *c* (plots *a* and *b*, respectively) of the rhombohedral phase of polymerized C_{60}. The values of parameters are given in hexagonal setting.

Temperature effect. The lattice parameters of the O′ phase obtained at room temperature allow us to conclude that polymerization entails a considerable shrinking within the basal plane, the lattice parameter on the average diminishing by 8.9% as compared to the pristine fcc phase. Polymerization makes change the volume per molecule C_{60} approximately by the same quantity (8.6%). In such hard crystals with stronger intermolecular interactions, one could expect a rather weak temperature dependence of the lattice parameters. We do not give the lattice parameters of the O′ phase as a function of temperature since, as mentioned before, this phase is an intermediate one exhibiting instabilities upon thermocycling. Nevertheless, it is necessary to note that the smoothed lattice parameter *a* increases over the range 80–293 K as a monotonic very weak function, the net relative increment not exceeding 0.03%. The lattice parameters along axes *b* and *c* change by 0.1% and 0.09%, respectively. The elementary volume of the orthorhombic polymer O′ changes insignificantly with temperature: within the same temperature range the overall change is about 0.23%.

The temperature dependence of the lattice parameters of the rhombohedral phase is shown in Fig. 2. The effect of temperature on the lattice parameter *a* (and the thermal expansion in basal plane of the polymerized state) is vertually unobservable below $T \sim 150$ K and shows a very weak tendency of expansion at higher temperatures. The overall increment of the parameter *a* from 80 to 293 K does not exceed

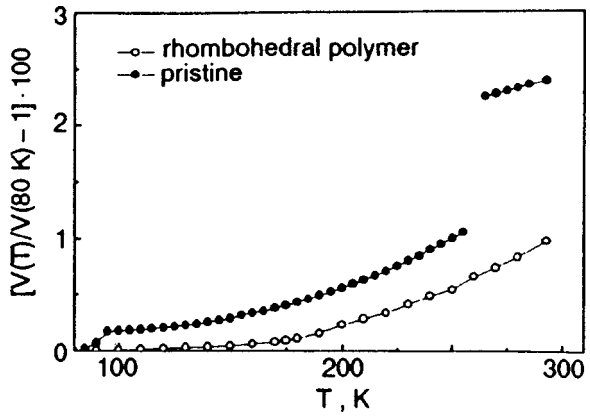

FIG. 3. Relative variation of the elementary cell volumes with temperature for the rhombohedral phase and pristine fullerite C_{60}, both normalized against their own values *V* at temperature 80 K. The data for pure C_{60} are taken from.[21]

0.2%. The lattice parameter *c* varies noticeably over the whole temperature range, especially near room temperature. Figure 3 shows relative variations of the elementary cell volumes with temperature for the rhombohedral and pristine fullerites, both normalized against the values at 80 K. The data for the latter phase are taken from our measurements.[20,21] As seen in Fig. 3, in contrast to pristine fullerite, for which distinct discontinuities are present at the phase transition point (260 K) and during the orientational glassification ($T < 100$ K), the volume of the R phase exhibits a weak uneventful increase with temperature. The overall R-phase volume change from 80 to 300 K, 0.98%, although being smaller then for pristine fullerite (5.75%[21]), nevertheless exceeds the volume increment for the O′ phase. This means that the thermal expansion of the R phase is noticeably larger than that of O′. As polymerization progresses, the anharmonisms of lattice vibrations and, hence, the thermal expansion are expected[12] to decrease. The ''inverse'' effect obtained here for the temperature-related variation of the volumes of the R and O′ phases might reflect the fact that our samples were not equilibrium states, possibly owing to the peculiarities of the polymerization procedure (pressure nonhydrostaticity and relatively low temperatures). Temperature can initiate relaxation processes in such samples that provide an extra contribution to the volume increase.

Depolymerization. Mechanical grinding of a part of the initial polymerized sintered sample led to recovery of the fcc structure of pristine C_{60}. This can be inferred from the diffraction patterns taken on powder samples. Of interest are the appreciable broadening and the low intensity of the reflections, which are typical of strongly strained samples. Subsequent annealing at $T \equiv 473$ K relieved the stresses caused by the grinding.

The structure studies on large-size sintered samples show that annealing at 573 K in air leads to depolymerization and formation of the equilibrium fcc phase. We present in Fig. 4 part of a diffraction pattern from an annealed sample. Note that the reflections of all the phases become appreciably narrower than in the source polymerized sample and the characteristic halo disappeared (cf. Fig. 1).

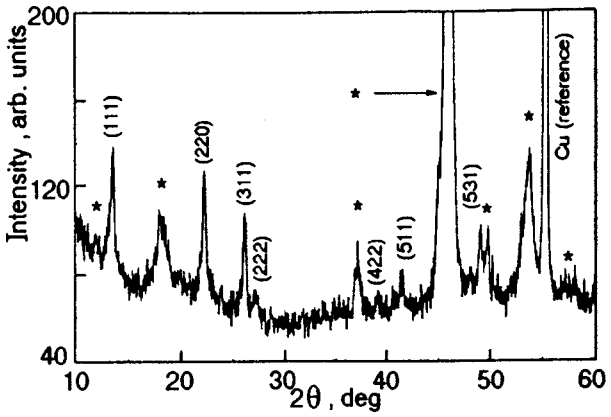

FIG. 4. X-ray diffraction pattern of depolymerized C_{60} after annealing at 573 K in air. The indices of the reflections (*hkl*) correspond to the fcc phase of the initial C_{60} sample. The asterisks indicate reflections from the new tetragonal phase.

We attribute these changes to the relieving of a part of interphase stresses and crystallization of the amorphous (or fine-grain) component. The indexing refers in Fig. 4 to the planes of the cubic (fcc) phase that re-emerges upon annealing. The respective lattice parameter, $a=14.21$ Å, turns out to be somewhat larger then in pristine fullerite. Such an expansion can be due to air components penetrated into the sample during annealing, which in turn must decrease the orientational phase transition (fcc-$Pa3$) temperature. Intercalating oxygen molecules O_2 are known[22] to occupy octahedral voids, whereas the transition point can vary within 3 to 20 K, depending on the O_2 concentration. As inferred from microhardness data, the orientational phase transition in annealed samples decreases by roughly 15 K.

However, under our annealing conditions, part of the sample can interact with the air components thereby helping a new phase to form (Fig. 4). The reflections of this phase (marked with asterisks) are seen in the diffraction pattern. The nature of this new phase or compound was not determined in these experiments. Attempts to index reflections of the new phase within cubic, hexagonal, or rhombohedral lattices were unsuccessful. The best fit was attained for a tetragonal lattice with parameters $a=9.08$ Å, $c=24.69$ Å, which however does not add much to our understanding of the nature of the new phase.

Examination of annealed fragments of sintered samples as well as the measured microhardness give evidence of phase inhomogeneity which develops during annealing.

3.2. Microhardness

Histograms. Since the studied polymerized C_{60} samples are multiphase ones, we might expect a polymodal distribution of impressions in size (and microhardness). The histograms of impressions of various diagonals and microhardness based on 57 measurements at $P=0.1$ N and $T=263-295$ K (where temperature variations of microhardness are typically very slight) are shown in Fig. 5. It is seen that the distribution is actually single-modal. This may be because the impressions produced by the indentor were larger in size than the single phase regions. It is also seen

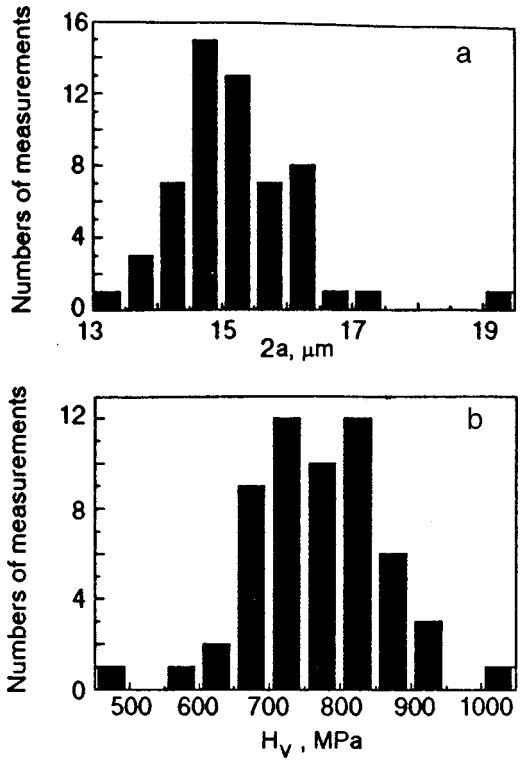

FIG. 5. Histograms for impression diagonal (a) and microhardness (b) on the basis of 57 impressions on the polymerized C_{60} surface under a load of $P=0.1$ N at 263–275 K (the temperature effect on H_V is negligible in this range).

that the relative scatter of the impression diagonal goes far beyond the measurement error (~ 0.15 μ). The scatter may be due to the inhomogeneous structure of the sample. The relative scatter (coefficient of variation), which is the ratio of the standard deviation *sd* to the average value, amounts to 6.3% for impression diagonals ($sd_{2a}\approx 0.96\mu$, $(2\overline{a})=15.2\mu$ and 11.8% for microhardness ($sd_{H_V}=90.2$ MPa, $\overline{H_V}=764.7$ MPa).

For single crystal C_{60}[20] the coefficient of microhardness variation is lower (9%), which suggests a higher degree of inhomogeneity of our polymerized samples.

The error can be reduced appreciably (which is very important to estimation of the temperature dependence of microhardness) if we used microhardness averaged over *n* impressions rather than its individual values. For the averaged microhardness the standard deviation decreases inversely with the number of measurements runs as $sd_{\overline{H_V}}=sd_{H_V}/n^{1/2}$. In Fig. 5b $sd_{\overline{H_V}}=11.9$ MPa and the relative error of the average value drops to 1.6%.

The temperature dependence of microhardness was studied on the surface with no fewer than 5 to 10 impressions at each temperature. The values averaged over these impressions were used to plot temperature dependencies of microhardness. At low temperatures the error of the average microhardness was two to three times higher, ~3–5% (because of the smaller number of measurement runs) than it is in Fig. 5b.

Loading effect. The typical correlation between the load applied to the indentor and the squared diagonal of the

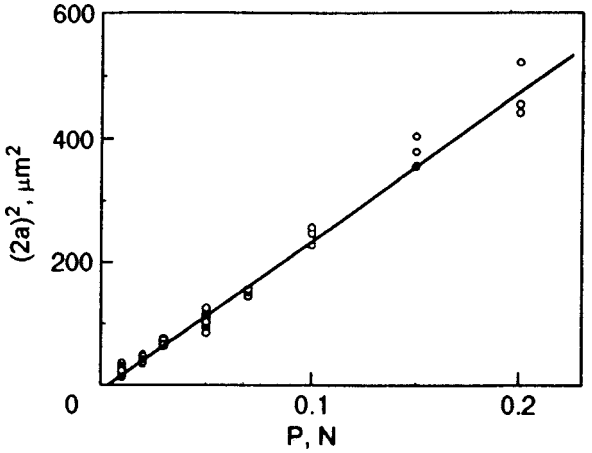

FIG. 6. Typical correlation between the squared impression diagonal and the load on indentor. The microhardness is inversely proportional to tan α (α is the angle between the straight line and the abscissa), $\overline{H_V}=766$ MPa (room temperature).

polymerized C_{60} is shown in Fig. 6. It is seen that in the range of load studied (0–0.2 N) microhardness was constant. Microhardness was independent of load both on the initial (non-polished) and on the polished surfaces. The average values of microhardness varied slightly after polishing the sample, i.e., the sample studied was quite homogeneous in its micromechanical properties over its depth. This helped us to derived the temperature dependence of microhardness on one sample.

Temperature effect. The temperature dependence of microhardness of polymerized C_{60} is shown in Fig. 7b For comparison, Fig. 7a shows the dependence $H_V(T)$ obtained earlier on single-crystalline fullerite C_{60}.[20,21] Both the dependencies are shown in the relative coordinates in Fig. 7c. Of interest are the following basic features.

(i). In the whole temperature range studied the microhardness of polycrystalline polymerized C_{60} was higher than that of nonpolymerized single crystals C_{60}: 3.8–4.5 times higher at room temperature and 2.6 times higher at liquid nitrogen temperature. A two-fold increase in microhardness at room temperature was observed by the authors[16] on C_{60} samples under high ($P=2$ GPa) pressure at $T=623$ K.

(ii). The temperature dependencies of microhardness taken on non-polymerized crystals and on polymerized samples of C_{60} display a sharp increase in microhardness at 240–260 K, i.e. in the temperature region of the fcc-sc phase transition in pure C_{60}. The fact seems to be surprising. According to x-ray diffraction data, there is no phase transition in polymerized samples at this temperatures. The studies of acoustic and dissipative properties of the polymeric C_{60} phase did not detect any visible anomalies at these temperatures either.[23] This behavior of microhardness may be attributed to destruction of the polymerized state in the region of the indentor impressions due to high stresses. This conforms with the above discussed depolymerization caused by grinding of polymerized fullerite. As shown in,[24] for Si crystals under high pressures phase transitions are possible in a narrow layer of the material beneath the indentor. In the case of

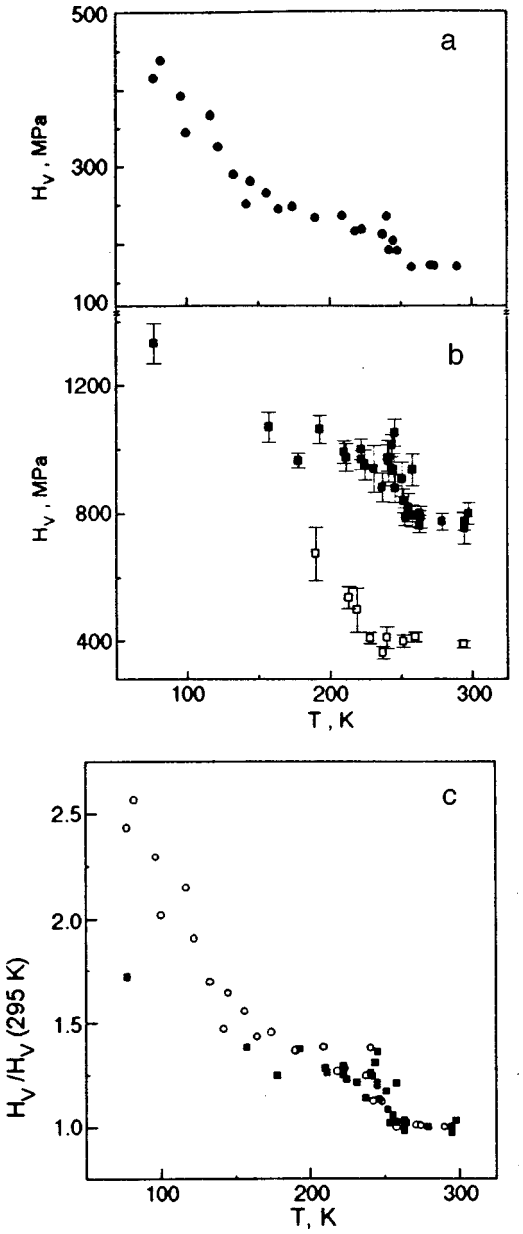

FIG. 7. Temperature dependence of the average microhardness for pure single crystal C_{60} (indentation in the (100) plane)[20,21] (a), and polymerized (■) and annealed (□) polycrystalline C_{60} (b). The error bars are r.m.s. deviations for $\overline{H_V}$. The results for polymerized C_{60} (■) and single crystal C_{60} (○) in relative units of $H_V(T)/H_V$ (295 K) is shown in figure (c).

fullerite, depolymerization beneath the indentor might be due to non-uniform shear strains.

The slope of the microhardness versus temperature curve for polymerized samples within the 77–175 K range was only one half of that observed for C_{60} single crystals (cf. Fig. 7c). This is in agreement with the data[23] on the temperature dependence of the elastic modulus of polymerized C_{60} and cubic fullerite in the low temperature region.

Annealing effect. Measurements at room temperature on a non-polished surface of annealed samples show that the average value of microhardness decreased from 765 to 440 MPa. When a thin surface layer was polished off, the value of microhardness was even lower, $H_V=337$ MPa.

Optic microscopic observation of a polished surface of

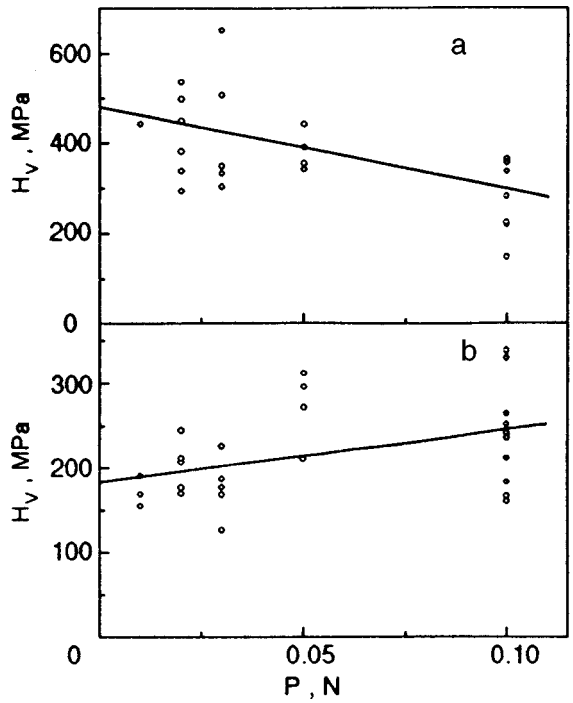

FIG. 8. The effect of load on the microhardness of two different phases formed after three hour annealing of a polymerized sample in air at 573 K: undentified phase (a), fcc phase of C_{60} (b).

an annealed sample revealed regions of different reflectivity—light and dark. This suggests phase inhomogeneity of the sample caused by annealing. The light and dark regions differ in microhardness and have opposite H_V—load dependencies (see Fig. 8). The latter is accounted for by the fact that under high loading onto the indentor, the impressions become comparable in size with the single-phase regions. In this case the formation of the impression is influenced by the neighboring phase.

One of the phases (the light regions) was close in microhardness to single crystalline C_{60}. According to x-ray diffraction data, this is the ordinary fcc phase. The other phase (the dark regions), still not identified, was harder. The temperature dependence of the average microhardness of sample also changed after annealing: the region of growing H_V shifted towards low temperatures (Fig. 7b). It should be noted that securing data for each of the two phases over all the temperature interval is very difficult.

The higher microhardness of polymerized polycrystalline C_{60} can be attributed to two factors—the fine-grained structure and polymerization. It is known that the correlation between the yield point σ_p of a polycrystal and the grain size d is well described by the Hall–Petch relation:[25]

$$\sigma_p = \sigma_0 + K_\sigma d^{-0.5}, \tag{2}$$

where σ_0 is the yield stress of a single crystal, and K_σ is the material constant. According to Friedel,[26] $K_\sigma \approx 0.2\mu b^{0.5}$ for brittle materials (μ is the shear modules, b is the Burgers vector). Friedel's estimate agrees well with experimental results taken on polycrystals of some fcc metals.[27] Hall assumes[28] that the dependence of microhardness on the grain size d can be described with a similar relation:

$$H_V = H_{V_0} + K_H d^{-0.5}, \tag{3}$$

where H_{V_0} is the microhardness of a single crystal, K_H is the material constant. The measurement shows[29] that the dependence (3) hold for Al, Cu and their alloys. The constant K_H is three to five times higher than K_σ.[29]

Using the above relations and the values of microhardness measured on poly- and single crystals of C_{60}, we can estimate the grain size ensuring the difference postulated in the assumption: the higher hardness of the polycrystal C_{60} is only due to the hardening effect of the grain structure. For C_{60} crystals only Young's modulus and the bulk modulus were found experimentally: $E = 20$ GPa,[30] $B = 12-14$ GPa.[31,32]

Hereafter, the estimation is based on the value $B = 12$ GPa. The shear modulus can be calculated from $\mu = E/(3 - E/3B) \approx 8.2$ GPa. Estimation from Friedel's results gives $K_\sigma \sim 0.5$ MPa·cm$^{0.5}$ and $K_H \approx 4K_\sigma \approx 2$ MPa·cm$^{0.5}$. To obtain the experimentally observed difference in microhardness ($\Delta H_V \approx 600$ MPa) of poly- and single crystals, the grain size should be $d = (K_H/\Delta H_V)^2 \approx 10^{-5}$ cm. This corresponds to the lower limit of grain sizes in x-ray diffraction studies on polycrystal samples.

Note that K_σ was calculated by the formula for brittle materials. For plastic C_{60} the K_σ value may prove overestimated. Then, the grains ensuring the above difference in microhardness of poly- and single crystals should be even smaller.

The above analysis shows that fine-grained structure and polymerization contribute to hardening of fullerite subjected to thermobaric treatment. So far, it is hardly possible to separate the effect of these two factors. It is pertinent to note that possible depolymerization beneath the indentor makes a noncontrollable contribution to hardness.

The authors are sincerely indebted to Prof. B. Sundqvist for kindly reading the manuscript and giving several important remarks that substantially improved this paper.

The authors, S.V.L., V.D.N., and L.S.F., wish to thank the Swiss National Science Foundation for the partial financial support of this work through a program CEEC/NIS, Project No 7UKPJ04864, A.V.S. acknowledges the financial support of the Swedish Natural Sciences Research Council (NFR).

*)E-mail: isakina@ilt.kharkov.ua
**)E-mail: alex.soldatov@physics.umu.se

1)This, in particular, can be inferred from optical measurements,[18,19] which give evidence that the average direction of these chains in those intermediate phases that could be termed as orthorhombic differs strongly from (110).

[1] J. D. Axe, S. C. Mooss, and D. A. Neumann, *Structure and Dynamics of Crystalline* C_{60}, in Solid State Physics, H. Ehrenreich and F. Spaepen (Eds.), Academic Press, New York (1994), **48**, p. 150.
[2] A. M. Rao, P. Zhou, K.-A. Wang, G. T. Hager, J. M. Holden, Y. Wang, W.-T. Lee, X.-X. Bi, P. C. Eklund, D. S. Cornett, M. A. Duncan, and I. J. Amster, Science **259**, 955 (1993).
[3] *Fullerenes and Fullerene Polymer Composites*, P. C. Eklund and A. M. Rao (Eds.), Springer Verlag, New York (1997).
[4] Y. Iwasa, T. Arima, R. M. Fleming, T. Siegrist, O. Zhou, R. C. Haddon, L. J. Rothberg, K. B. Lyons, H. L. Carter Jr., A. F. Hebard, R. Tycko,

G. Dabbagh, J. J. Krajewski, G. A. Thomas, and T. Yagi, Science **264**, 1570 (1994).
[5] I. O. Bashkin, V. I. Raschupkin, N. P. Kobelev, A. P. Moravsky, Ya. M. Soifer, and E. G. Poniatovsky [JETP Lett. **59**, 279 (1994)].
[6] I. O. Bashkin, V. I. Rashchupkin, A. F. Gurov, A. P. Moravsky, O. G. Rybchenko, N. P. Kobelev, Ya. M. Soifer, and E. G. Ponyatovsky, J. Phys.: Condens. Matter **6**, 7491 (1994).
[7] A. P. Moravsky, G. E. Abrosimova, I. O. Abrosimova, I. O. Bashkin, R. A. Dilanian, A. F. Gurov, N. P. Kobelev, V. I. Rashchupkin, O. G. Rybchenko, Ya. M. Soifer, V. Sh. Shekhtman, and E. G. Ponyatovsky, in *Recent Advances in the Chemistry and Physics of Fullerenes and Related Materials*, R. S. Ruoff and K. M. Kadish (Eds.), The Electrochemical Society, Inc., Pennington (1995), **95–10**, p. 952.
[8] M. Nunes-Regueiro, L. Marques, J.-L. Hodeau, O. Bethoux, and M. Perroux, Phys. Rev. Lett. **74**, 278 (1995).
[9] L. Marques, M. Nunez-Regueiro, and M. Perroux, Phys. Rev. B **54**, R12633 (1996).
[10] A. M. Rao, P. C. Eklund, U. D. Venkateswaran, J. Tucker, M. A. Duncan, G. Bendele, P. W. Stephens, J.-L. Hodeau, L. Marques, M. Nunez-Regueiro, I. O. Bashkin, E. G. Ponyatovsky, and A. P. Morovsky, Appl. Phys. A: Mater. Sci. Process. **A64**, 231 (1997).
[11] P.-A. Persson, U. Edlund, P. Jacobsson, D. Johnels, A. Soldatov, and B. Sundqvist, Chem. Phys. Lett. **258**, 540 (1996).
[12] B. Sundqvist, O. Anderson, U. Edlund, A. Fransson, A. Inaba, P. Jacobsson, D. Johnels, P. Launois, C. Meingast, R. Moret, T. Moritz, P. A. Persson, A. Soldatov, and T. Wagberg, in *Recent Advances in the Chemistry and Physics of Fullerenes and Related Materials*, R. S. Ruoff and K. M. Kadish (Eds.). The Electrochemical Society, Pennington, Inc. (1996), **96–10**, p. 1014.
[13] B. Ya Farber, N. S. Sidorov, V. I. Kulakov, Yu. A. Iunin, A. N. Izotov, G. A. Emel'chenko, V. S. Bobrov, L. S. Fomenko, V. D. Natsik, and S. V. Lubenets, Sverkhprovodimost: Fiz., Khim., Tekh. **4**, 2393 (1991) (in Russian).
[14] B. Sundqvist, *Fullerenes under High Pressures* (review), Adv. Phys. (1998), in press.
[15] V. Agafonov, V. A. Davydov, L.-S. Kashevarova, A. V. Rakhmanina, A. Kahn-Harari, P. Dubois, R. Ceolin, and H. Szwarc, Chem. Phys. Lett. **267**, 193 (1997).
[16] R. Moret, P. Launois, P.-A. Persson, and B. Sundqvist, Europhys. Lett. **40**, 55 (1997).
[17] N. A. Aksenova, A. P. Isakina, A. I. Prokhvatilov, M. A. Strzhemechny, A. V. Soldatov, and B. Sundqvist, in *Recent Advances in the Chemistry and Physics of Fullerenes and Related Materials*, R. S. Ruoff and K. M. Kadish (Eds.). The Electrochemical Society, Inc., Pennington (1997), **97–42**, p. 687.
[18] V. A. Davydov, L. S. Kashevarova, A. V. Rakhmanina, A. V. Dzyabchenko, V. Agafonov, P. Dubois, R. Ceolin, and H. Szwarc [JETP Lett. **66**, 120 (1997)].
[19] V. A. Davydov, L. S. Kashevarova, A. V. Rakhmanina, V. Agafonov, R. Ceolin, and H. Szwarc, Carbon **35**, 735 (1997).
[20] L. S. Fomenko, V. D. Natsik, S. V. Lubenets, V. G. Lirtsman, N. A. Aksenova, A. P. Isakina, A. I. Prokhvatilov, M. A. Strzhemechny, and R. S. Ruoff, Fiz. Nizk. Temp. **21**, 465 (1995) [Low Temp. Phys. **21**, 364 (1995)].
[21] S. V. Lubenets, V. D. Natsik, L. S. Fomenko, A. P. Isakina, A. I. Prokhvatilov, M. A. Strzhemechny, N. A. Aksenova, and R. S. Ruoff, Fiz. Nizk. Temp. **23**, 338 (1997) [Low Temp. Phys. **23**, 251 (1997)].
[22] S. A. Myers, R. A. Assink, J. E. Schirber, and D. A. Loy, Mater. Res. Soc. Symp. Proc. **359**, 505 (1995).
[23] N. P. Kobelev, Ya. M. Soifer, I. O. Bashkin, A. P. Moravsky, and E. G. Ponyatovsky, Mol. Mater. **7**, 261 (1996).
[24] A. Kailer, Y. G. Gogotsi, and K. G. Nickel, J. Appl. Phys. **81**, 3057 (1997).
[25] E. O. Hall, Proc. Phys. Soc. London, Sect. B **B64**, 747 (1951).
[26] J. Friedel, *Dislocations*, Pergamon Press, Oxford (1964).
[27] V. I. Trefilov, Yu. V. Mil'man, S. A. Firstov, *Fizicheskije Osnovy Prochnosti Tugoplavkikh Metallov*, Kiev, Naukova Dumka (1975).
[28] E. O. Hall, Nature (London) **173**, 948 (1954).
[29] A. S. Taha and F. H. Hammad, Phys. Status Solidi A **A119**, 455 (1990).
[30] S. Hoen, N. G. Chopra, X.-D. Xiang, R. Mostovoy, Xianguo Hou, W. A. Vareka, and A. Zettl, Phys. Rev. B **46**, 12737 (1992).
[31] J. E. Schirber, G. K. Kwei, J. D. Jorgensen, R. L. Hitterman, and B. Morosin, Phys. Rev. B **51**, RC12014 (1995).
[32] H. A. Ludwig, W. H. Fietz, F. W. Hornung, K. Grube, B. Wagner, and G. J. Burkhart, Z. Phys. B **96**, 179 (1994).

This article was published in English in the original Russian journal. It was edited by R. T. Beyer.

LOW-TEMPERATURE PHYSICS OF PLASTICITY AND STRENGTH

Internal friction peak in CsI single crystal at liquid helium temperatures

S. N. Smirnov, V. D. Natsik, and P. P. Pal'-Val'

*B. Verkin Institute for Low Temperature Physics and Engineering, National Academy of Sciences of the Ukraine, 310164 Kharkov, Ukraine**

(Submitted July 10, 1998)
Fiz. Nizk. Temp. **24**, 1202–1206 (December 1998)

Acoustic relaxation in undeformed and plastically deformed CsI single crystals is studied using the composite oscillator technique at frequencies $(1-7)\times 10^5$ Hz in the temperature range 2–15 K. Plastic deformation leads to the emergence of an internal friction peak localized in the temperature range 4–5 K. It is shown that the peak is shifted towards higher temperatures upon an increase of the vibrational frequency and corresponds to a thermally activated relaxation process with very low values of activation energy $U\approx 1.9\times 10^{-3}$ eV and the attack frequency $\nu_0\approx 6.7\times 10^8\ \mathrm{s}^{-1}$. The interaction of sound with dislocation kinks migrating in the second-order Peierls relief is considered as a possible mechanism of peak formation. © *1998 American Institute of Physics.* [S1063-777X(98)01012-3]

INTRODUCTION

The study of crystalline materials by acoustic spectroscopy methods at liquid helium temperatures and in the subkelvin temperature range makes it possible to detect local structure rearrangements limited by overcoming potential barriers of very small height of the order of $10^{-2}-10^{-3}$ eV. Relaxation peaks on temperature dependences of internal friction and smeared step-like changes of elastic moduli as functions of temperature are experimental evidences of these processes. Such peculiarities were detected in the investigation of a number of metallic crystals like Nb,[1–6] Mi,[7] and aluminum[8] at temperatures $T<10$ K. Another type of anomalies also associated with low-temperature rearrangements of atomic structure were observed in an analysis of the temperature dependences of elastic moduli of amorphous solids (glasses)[9] and crystals with a large number of defects.[10–14] We are speaking of a linear increase in elastic moduli upon cooling, a logarithmic run up to a peak at temperatures of the order of 0.1–1 K, and a logarithmic decrease in the subkelvin temperature range.

Atomic mechanisms of these rearrangements and acoustic anomalies associated with them are apparently different for different crystalline and amorphous materials. However, both type of anomalies can be successfully interpreted on the basis of the phenomenological model of double-well energy states and two-level tunneling systems. This model assumes that individual elements of the structure (groups of atoms) distributed densely over the volume of a solid have different configurations with close values of potential energy, which are separated by low energy barriers. Transitions between such configurations can occur through thermal activation or through quantum tunneling and are stimulated by elastic vibrations. An analysis of relaxation and resonant interaction of elastic vibrations with these rearrangements taking into account thermal fluctuations and quantum tunneling as well as the statistics of barriers (in the case of strongly disordered structures) makes it possible to obtain a unique and noncontradictory description of all the main peculiarities in acoustic properties of solids at very low temperatures.

Low-temperature singularities in thermal properties of crystalline and amorphous materials are also closely related to the acoustic anomalies under consideration. For this reason, the problem of low-energy structure rearrangements is interesting not only from the point of view of fundamental solid state physics, but also for many important applications, e.g., for the development of methods of precision low-temperature measurements and detectors of gravitational waves.[12]

In some cases, it was possible to impart a microscopic meaning to the phenomenological model of low-energy structure rearrangements applied for interpreting specific experimental observations by using the concepts and terms of dislocation physics.[5,6,8,10] In the physics of dislocation, we often encounter elementary structural processes limited by overcoming low energy barriers, e.g., the formation and displacement of kinks on dislocation lines. This facilitates the application of dislocation models for interpreting low-temperature acoustic and thermal anomalies. The authenticity and unambiguity of an interpretation in this case can be considerably improved by using a controllable change in the volume density and parameters of dislocation kinks, which is possible under special types of thermal[5] and acoustic[10] loading or preliminary plastic deformation.[8]

So far, acoustic anomalies of dislocation origin were detected in the regions of very low temperatures $T<10$ K only in metallic crystals. In this communication, we prove that the introduction of dislocations in alkali-halide crystal CsI also leads to the emergence of an internal friction peak at liquid helium temperatures. The peak is localized in the temperature range 4–5 K for vibrational frequencies $(3-7)$

 © 1998 American Institute of Physics

$\times 10^5$ Hz. A displacement of the peak on the temperature axis upon a change in vibrational frequency indicates that it is a result of resonant interaction of elastic vibrations with a thermally activated low-energy relaxation process with activation energy $U \approx 1.9 \times 10^{-3}$ eV.

1. EXPERIMENTAL TECHNIQUE

Low-temperature acoustic properties of a CsI crystal were studied using the method of a two-component composite piezoelectric vibrator. The samples were in the form of a right parallelepiped with cross section 2.2×2.2 mm and length 11–13 mm. The longitudinal axis of the samples had the crystallographic orientation ⟨110⟩ with a possible deviation not exceeding 2°. The samples were cut by the spark-erosion technique from a CsI single crystal grown in vacuum and were polished on a soft wet cloth to attain the required geometrical size. The end faces were polished by fine abrasive to make them plane-parallel and to attain good acoustic contact after gluing with the piezoelectric vibrator. Final finishing of the surface was carried out by chemical polishing in methanol. The orientation of single crystals was determined by using Laue diffraction patterns. After annealing for 8 hours at 500 °C and polishing, the samples were glued to quartz piezoelectric resonators.

Acoustic measurements were made in the frequency range $\omega/2\pi \approx (1-7) \times 10^5$ Hz. Longitudinal standing waves were excited in the samples at frequencies close to 1, 3, 5, and 7 harmonics of quartz. The resonance frequency of forced oscillations of the vibrator and the active electric resistance at resonance were measured. The results of measurements were processed by the method proposed by us earlier:[15] the logarithmic decrement δ of vibrations and Young's modulus E of the samples were measured at different harmonics of the vibrator after preliminary testing of the parameters of quartz resonators.

The temperature dependences of the decrement and resonance frequency were measured in the temperature range 2–15 K at a constant amplitude of ultrasonic deformation of the order of 10^{-6} in the region of amplitude-independent absorption of ultrasound. The measurements were made in a helium cryostat with evacuation of ^{4}He vapor to a pressure of 290 Pa. The sample with the quartz transducer was mounted in the heater of the working chamber immersed in liquid helium at a temperature approximately equal to 1.4 K. Heat transfer between the walls of the chamber and the sample was ensured by gaseous helium under a pressure of 2×10^3 Pa. Temperature was measured by a gallium-arsenide resistance thermometer TSAD-2. Such experimental conditions made it possible to cool the samples to 2 K. Intermediate temperatures in the interval $2\,\mathrm{K} < T < 15\,\mathrm{K}$ were attained with the help of an electric heater and were stabilized by a semi-automatic temperature control system.

The measurements were first made on an undeformed sample, which was subsequently subjected (without detachment from quartz) to plastic strain of the order of 3% by compression along its longitudinal axis at a rate of $10^{-4}\,\mathrm{s}^{-1}$ at room temperature in a specially designed microdeformation machine. Plastic deformation was carried out along the easy slip systems ⟨100⟩{110} typical of CsI. Undeformed samples had the initial dislocation density of the order of $10^4\,\mathrm{cm}^{-2}$, the average density of dislocations after deformation being of the order of $10^6\,\mathrm{cm}^{-2}$.

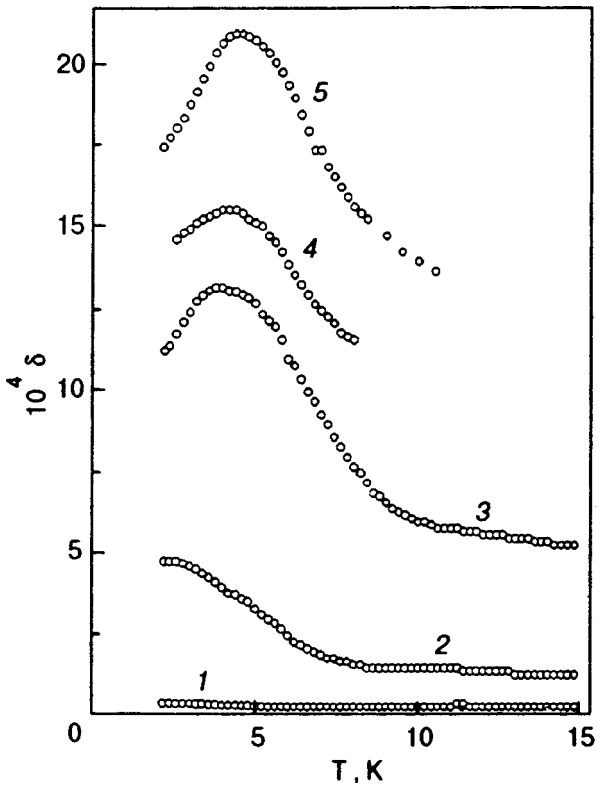

FIG. 1. Peaks on temperature dependences of decrement δ of vibrations of a CsI monocrystalline sample initiated by plastic deformation and their displacement upon a change in the vibrational frequency: undeformed sample (curve *1*) and deformed sample (curves *2*–*5*). The values of resonant frequency $\omega/2\pi$ and temperature T_m of the peak: 1×10^5 Hz (curve *1*), 1×10^5 Hz, T_m=? (curve *2*), 3×10^5 Hz, T_m=3.9 K (curve *3*), 5×10^5 Hz, T_m=4.2 K (curve *4*), and 7×10^5 Hz, T_m=4.5 K (curve *5*).

2. DISCUSSION OF EXPERIMENTAL RESULTS

Figure 1 shows temperature dependences of the decrement δ for one of the samples, obtained at different frequencies. The decrement of the undeformed sample (curve *1* in Fig. 1) had a very small magnitude of the order of 2×10^{-5}, indicating a perfect initial structure of the samples. In this case, a weak monotonic increase in δ is observed upon cooling.

After deformation, ultrasound absorption increases considerably and acquires a strong temperature dependence. The decrement increases monotonically upon cooling at the fundamental harmonic ($\omega/2\pi \approx 10^5$ Hz), displaying a tendency to saturation below 3.2 K, after which absorption becomes almost temperature independent in the temperature range 2.2–2.6 K (curve *2*). The absolute value of δ at $T \approx 2.2$ K attains the value 5×10^{-4}, indicating a considerable inelastic deformation in the sample. As the frequency of vibrations increases, the $\delta(T)$ dependences for a deformed sample acquire clearly manifested peaks whose positions on the temperature axis depends on frequency: with increasing fre-

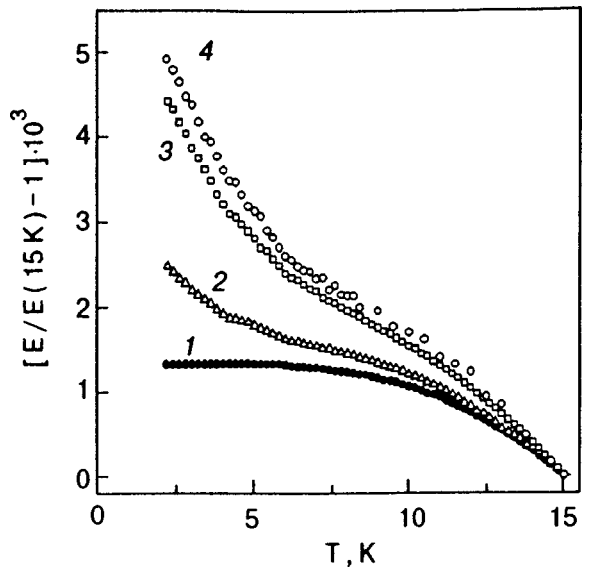

FIG. 2. Effect of plastic deformation on the temperature and frequency dependences of the Young modulus E of a monocrystalline CsI sample: undeformed sample (curve *1*) and deformed sample (curves *2–4*). The values of resonant frequency $\omega/2\pi$: 1×10^5 Hz (curves *1* and *2*), 3×10^5 Hz (curve *3*) and 7×10^5 Hz (curve *4*). For the sake of visualization, the measured values of the Young's modulus are reduced to the temperature 15 K corresponding to the upper limit of the temperature interval under investigation.

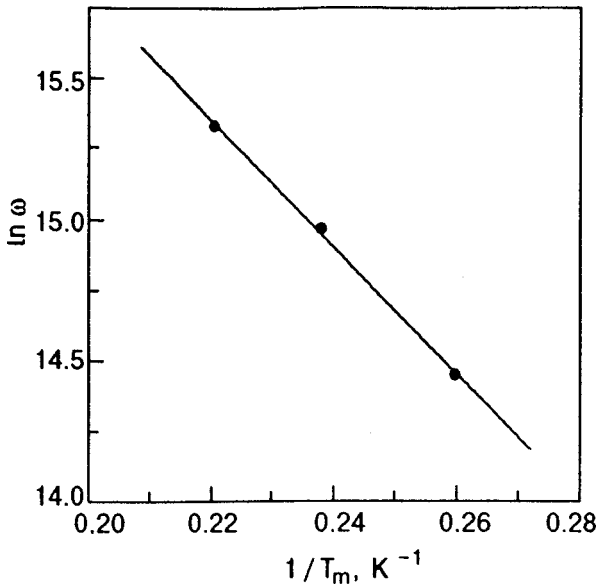

FIG. 3. Frequency dependence $T_m(\omega)$ of the temperature corresponding to the acoustic absorption peak: points correspond to experimental data presented in Fig. 1, and the straight line is the plot of the function (2) corresponding to the values of the parameter $U\approx1.9\times10^{-3}$ eV and $\nu_0\approx6.7\times10^8\ \mathrm{s}^{-1}$.

quency, the temperature T_m corresponding to the peak is shifted regularly towards higher temperatures. (curves *3–5*).

It should be noted that the presence of a peak on curve *2* (Fig. 1) remains disputable since technical potentialities of the experiment did not allow us to study the temperature interval $T<2$ K.

Figure 2 illustrates the effect of deformation on the temperature and frequency dependences of the dynamic Young's modulus $E(T,\omega)$. As a result of deformation in the vicinity of temperatures T_m corresponding to absorption peaks, temperature dependences of the Young's modulus acquire regions in which the modulus increases sharply upon cooling. These anomalies can be interpreted as fragments of smeared step-like changes corresponding to relaxation absorption peaks.

Thus, a significant increase in dislocation density in a CsI single crystal as a result of plastic deformation leads to the emergence of an acoustic relaxation peak at liquid helium temperatures. Going over to the interpretation of the peak, we assume that it is a consequence of resonant interaction of sound with a system of uniform thermally activated relaxators for which the temperature dependence $\tau(T)$ of relaxation time is described by the standard Arrhenius formula

$$\tau(T)=\nu_0^{-1}\exp(U/kT), \tag{1}$$

where U is the activation energy and ν_0 is the effective attack frequency. In this case, the frequency dependence $T_m(\omega)$ of the temperature corresponding to the peak is determined by the condition $\omega\tau(T_m)=1$ which leads to the relation

$$\ln\omega=\ln\nu_0-U/kT_m. \tag{2}$$

Figure 3 shows that the values of T_m recorded at three highest harmonics of the piezoelectric vibrator are correctly described by relation (2). For the parameters of relaxation process, we obtain from Fig. 3 the following empirical estimates:

$$U\approx1.9\times10^{-3}\ \text{eV},\quad \nu_0\approx6.7\times10^8\ \mathrm{s}^{-1}. \tag{3}$$

A low-temperature relaxation process with parameters (3) appears in a CsI crystal as a result of plastic deformation, and hence it is connected with fresh dislocations in a certain way. Such low values of activation parameters of the process reduce considerably the range of possible dislocation mechanisms which can be used for interpreting the observed acoustic absorption peak. In our opinion, the most probable reason behind the observed anomaly in acoustic properties of CsI is resonant interaction of sound with a chain of dislocation kinks participating in thermally activated diffusion in the second-order Peierls relief. With such an interpretation, the energy U has the meaning of the height of the lattice potential relief for dislocation kinks. The operation of this mechanism is described in detail in Refs. 5 and 6, where it was used for interpreting the low-temperature peak of acoustic relaxation in niobium.

It should be noted in conclusion that an unambiguous physical interpretation of the low-temperature anomaly in the acoustic properties of a CsI crystal observed by us here requires additional acoustic experiments in the temperature range $T<2$ K extended towards low temperatures as well as the detection and analysis of dislocation structures emerging in the crystal as a result of plastic deformation. Such experiments are planned for nearest future.

This research was carried out under partial support by the Ukrainian Fund for Fundamental Research (Project No.

2.4/156 ''Bion'') and by the International Science Foundation (grant No. U9T000).

*E-mail: smirnov@ilt.kharkov.ua

[1] E. J. Kramer and C. L. Bauer, Phys. Rev. **163**, 407 (1967).
[2] K. F. Huang, A. V. Granato, and H. K. Birnbaum, Phys. Rev. B **32**, 2178 (1985).
[3] E. Drescher-Krasicka and A. V. Granato, J. Phys. (Paris) **46**, 1073 (1985).
[4] G. Cannelli, R. Cantelli, and F. Cordero, Phys. Rev. B **34**, 7721 (1986).
[5] P. P. Pal'-Val', V. D. Natsik, and L. N. Pal'-Val', Fiz. Nizk. Temp. **21**, 647 (1995) [Low Temp. Phys. **21**, 505 (1995)].
[6] V. D. Natsik and P. P. Pal'-Val', Fiz. Nizk. Temp. **23**, 1229 (1997) [Low Temp. Phys. **23**, 922 (1997)].
[7] W. Duffy, Jr., J. Appl. Phys. **72**, 5628 (1992).
[8] T. Kosugi and T. Kino, Mater. Sci. Eng., A **164**, 368 (1993).
[9] H. v. Lösneysen, Phys. Reports (Rev. Sect. of Phys. Lett.) **79**, 161 (1981).
[10] A. Hikata and C. Elbaum, Phys. Rev. Lett. **54**, 2418 (1985).
[11] A. Hikata, M. J. McKenna, and C. Elbaum, Phys. Rev. B **40**, 5247 (1989).
[12] R. N. Kleiman, G. Agnolet, and D. J. Bishop, Phys. Rev. Lett. **59**, 2079 (1987).
[13] P. Esquinazi, R. Koenig, and F. Pobell, Europhys. News **24**, 105 (1993).
[14] E. Gaganidze, P. Esquinazi, and R. Koenig, Europhys. Lett. **31**, 13 (1995).
[15] V. D. Natsik, P. P. Pal'-Val', and S. N. Smirnov, Akust. Zh. **44**, 696 (1998).

Translated by R. S. Wadhwa

BRIEF COMMUNICATIONS

Mössbauer detection of photoinduced effects in HTSC $YBa_2(Cu_{1-x}{}^{57}Fe_x)_3O_{6+\delta}$

V. V. Eremenko, D. V. Lukashev, and V. L. Ponomarchuk

*B. Verkin Institute for Low Temperature Physics and Engineering, National Academy of Sciences of the Ukraine, 310164 Kharkov, Ukraine**

(Submitted July 27, 1998)
Fiz. Nizk. Temp. **24**, 1207–1210 (December 1998)

Photoinduced changes of the effective magnetic field on ^{57}Fe nuclei at the Cu(2) site are detected by the Mössbauer technique in $YBa_2(Cu_{0.92}{}^{57}Fe_{0.08})_3O_{6.3}$. The effect is found to be reversible for several hours in the temperature range 100–300 K. © *1998 American Institute of Physics.* [S1063-777X(98)01112-8]

In recent years, a large number of papers have been devoted to investigations of the effect of light on HTSC samples. To study this effect, various optical techniques were used and measurements of conductivity, magnetization, etc., were made (see the review by Yu and Heeger.[1] Mössbauer spectroscopy is used extensively for studying the properties of HTSC (see reviews in Refs. 2 and 3). However, this technique has not been used, to our knowledge, for studying photoinduced effects in HTSC. In this communication, we present the results of investigation of the Mössbauer spectra of the $YBa_2(Cu_{0.92}{}^{57}Fe_{0.08})_3O_{6.3}$ samples exposed to light in the temperature range 100–300 K.

The $YBa_2(Cu_{0.92}{}^{57}Fe_{0.08})_3O_{6+\delta}$ sample, which was prepared by the standard ceramic technology and annealed in vacuum, was found to be in the semiconducting tetra-phase ($O_{6+\delta} \simeq 6.3$). We assume that the sample contains oxygen-defective regions that are characteristic of nonstoichiometric compositions. The initial sample (pellet) was crushed into a powder of grain size ~ 10 μm to increase the area of the material being exposed to light. In order to improve the heat removal, the powder was wetted with paraffin and placed between a mica film and an aluminum foil reflecting light. The effective ^{57}Fe thickness was less than 0.2 mg/cm^2.

We measured the Mössbauer spectra of samples before illumination, during illumination with a flux density 13 and 40 mW/cm^2, as well as after illumination. Samples were exposed to radiation from a He–Ne laser with radiation wavelength 632.8 nm in the CW mode. The thermal stabilization of the sample was carried out in a cryostat. Storage of the spectra ''after illumination'' was carried out at the temperature of illumination (without warming). Before storing the spectrum, the sample was warmed to room temperature prior to illumination and kept at this temperature for more than two days. As a result of illumination, the sample temperature (measured by a differential thermocouple) did not rise by more than 1.1 K at $T = 290$ K for an optical flux density 13 mW/cm^2.

The Mössbauer spectrum of $YBa_2(Cu_{0.92}{}^{57}Fe_{0.08})_3O_{6.3}$ samples (Fig. 1) is a superposition of a Zeeman sextet and three quadrupole doublets. The sextet is characteristic of the tetra phase and is observed in the spectra of oxygen-deficient samples of $YBa_2(Cu_{1-x}{}^{57}Fe_x)_3O_{6+\delta}$.[4,5] The three quadrupole doublets correspond to three nonequivalent Cu(1) sites occupied by iron, and are analogous to the doublets in the spectra of samples with $6+\delta > 6.5$.[6]

In order to identify the sextet, we made Mössbauer measurements on samples aligned in a magnetic field. It is well known[6] that finely disperse $YBa_2(Cu_{1-x}{}^{57}Fe_x)_3O_{6+\delta}$ powder in a viscous filling acquires a cylindrical texture in a magnetic field, so that the **c**-axis of the crystallites is oriented along the applied magnetic field. If the effective magnetic (we shall use the terms effective or hyperfine in the following) field at the nucleus has the same probability of being oriented relative to the direction of γ-quanta (nonaligned sample), the ratios of areas of the sextet components are 3:2:1:1:2:3 (Fig. 1b).[7] If the effective field at the nucleus is at right angles to the direction of γ-quanta, the sextet component areas are in the ratio 3:4:1:1:1:4:3.[7] The areas of sextet components in an aligned sample (Fig. 1a) are nearly in the same ratio if the **c**-axis in the experiment is parallel to the direction of the γ-quanta so that the magnetic moments of the antiferromagnetically ordered iron atoms lie in the (**ab**)-plane.

The results of measurements at temperatures 260–300 K were analyzed according to the technique described in Ref. 8 (the quadrupole splitting at these temperatures practically does not change in comparison with the magnetic splitting). It was found that for a given site, the electric field gradient (EFG) tensor component V_{ZZ} is positive and parallel to **c**. The asymmetry parameter η of the EFG tensor is ~ 0.2. Hence this position corresponds to ^{57}Fe which occupies the Cu(2) site. This result is in accord with those obtained in Refs. 4 and 5.

The electric quadrupole interaction energy is an order of magnitude lower than the magnetic dipole interaction energy, the EFG asymmetry parameter is small, and hence the energy-level diagram can be described correctly by a formula for the axially symmetric EFG with its symmetry axis at right angles to the magnetic axis:[7]

 © 1998 American Institute of Physics

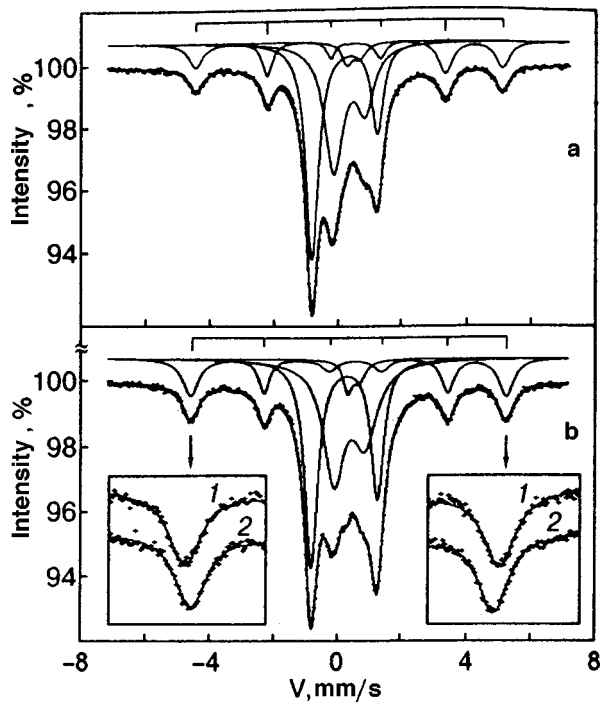

FIG. 1. Mössbauer spectra of $YBa_2(Cu_{0.92}{}^{57}Fe_{0.08})_3O_{6.3}$: powder aligned in a magnetic field at 295 K (a) and nonaligned powder at 290 K (b). The insets show the first and sixth lines of the sextet in the dark (curve *1*) and under illumination (curve *2*). Spectral decomposition is shown in the model of three quadrupole doublets and a magnetic sextet.

$$E_{mQ} = -g_I \mu_n H_n m_I - (-1)^{|m_I|+1/2} \frac{eQV_{ZZ}}{8},$$

where g_I is the nuclear gyromagnetic ratio for the given nuclear level, μ_n the nuclear magneton, H_n the effective field at the nucleus, $m_I = I,(I-1),\ldots,-I$ (I is the nuclear spin, $I_g = 1/2$ for the ground state, and $I_e = 3/2$ for the excited state), Q is the nuclear quadrupole moment, and V_{ZZ} the EFG tensor component. The separation between the lines in the sextet can be used to calculate the effective field at the nucleus and the value of the quadrupole splitting.

It was found that the illumination of a $YBa_2(Cu_{0.92}{}^{57}Fe_{0.08})_3O_{6.3}$ sample leads to a decrease in the sextet splitting, and hence a decrease in the effective field at ^{57}Fe nuclei occupying the Cu(2) site. The insets to Fig. 1b show the displacement of the first and sixth sextet lines under illumination. Figure 2 shows the temperature dependence of the effective field at the nucleus in the temperature range 100–300 K. The values of the field are for samples in the dark and upon illumination in the optical flux of density 13 mW/cm^2. The splitting of a sextet does not change during continuous illumination for three days. It is found that an increase in the flux density of the optical radiation incident on the sample causes a further decrease in the effective field at the nucleus (see inset to Fig. 2).

The variation of the effective field, determined from the line shift, occurs over an hour. This is indicated by the absence of broadening of the lines during storage of the spectrum in the first few hours after beginning of the exposure. Moreover, a decrease in the magnetic splitting as a result of exposure is accompanied by a decrease in the width of the

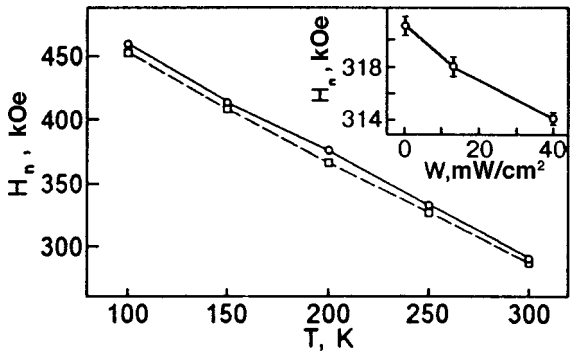

FIG. 2. Temperature dependence of effective field at ^{57}Fe nuclei at the Cu(2) site for a $YBa_2(Cu_{0.92}{}^{57}Fe_{0.08})_3O_{6.3}$ sample in the dark (○, solid line) and under He–Ne laser irradiation (□, dashed line). The inset shows the dependence of effective field at 273 K on the density of luminous flux incident on the sample.

sextet lines. Thus, the mean values of the line width depend upon the optical flux density as follows: 0.50 mm/s for unexposed samples, 0.48 mm/s for a flux density 13 mW/cm^2, and 0.47 mm/s for 40 mW/cm^2. Hence the effective field at the iron nuclei decreases at this site over the entire volume of the crystallite, while the light penetration depth is of the order of the wavelength. This points towards the migration of photoinduced excitations over the volume of the crystallite.

Measurements made after the termination of the illumination show that the effect is reversible. Unlike persistent photoconductivity,[9] where the effect is preserved at low temperatures for several days, the hyperfine field at Fe nuclei at the Cu(2) site is restored in less than an hour.

We assume that the mechanism of decrease in the effective field at ^{57}Fe nuclei occurring as a result of illumination is identical to the mechanism proposed for explaining persistent photoconductivity. It is believed[1,9,10] that electron-hole pairs are created in the CuO_2 plane upon illumination. Electrons are transported and localized in CuO_x chains, while hole charge carriers in the CuO_2 plane enhance the conductivity of the material. The localization of electrons at the traps in CuO_x chains is responsible for the emergence of long-lived ordering of oxygen in chains, stretching of chains,[11–13] photoinduced separation of the sample into tetra- and ortho-phase regions,[14] and an increase in T_c associated with the formation of a secondary potential relief in the CuO_2 plane by charges in CuO_x chains.[13] We believe that the electrons participating in indirect exchange interaction which leads to the antiferromagnetic ordering of atomic moments at Cu(2) sites are excited upon illumination. Hence a decrease in the number of these electrons leads to a decrease in the exchange interaction parameter resulting in a lowering of the magnetization of sublattices and Neel temperature, and is manifested in a decrease in the hyperfine field at the nucleus. Thus, it can be assumed that the change in the hyperfine field at the nucleus is proportional to the change in hole concentration.

Attributing the small decrease in isomeric shift of the sextet upon illumination to the second-order Doppler effect, we obtain the value of heating (1.3 K). The quadrupole

splitting of the sextet in the investigated temperature range remains practically unchanged in the dark and under illumination ($eQV_{ZZ}/2=(0.50\pm0.04)$ mm/s). The relative area of the sextet remains unchanged during illumination. Hence optical radiation does not create long-lived local distortions of the crystal structure in the nearest coordination spheres of these iron nuclei since new lines in the spectrum would emerge otherwise. This leads to the conclusion that photoinduced holes are distributed uniformly over the crystal volume and the time of their localization at ^{57}Fe nuclei at Cu(2) sites is less than 10^{-7} s (lifetime of the ^{57}Fe nucleus in the excited state). Hence the effect of illumination on ^{57}Fe at Cu(2) sites is manifested only in a decrease in the effective field at the nucleus. Note that the observed decrease in the magnetic splitting upon illumination is equivalent to heating by 8.5–11 K, i.e., much larger than the real heating which amounts to just 1.1 K.

The width of the sextet lines decreases upon exposure to light. The higher the irradiation intensity, the narrower the lines. Since the photoelectric effect occurs only in a thin surface layer, it must be admitted that electron–hole pairs migrate over the bulk of the crystallite to a depth of the order of 5 μm. Otherwise, the Mössbauer spectrum would show the superposition of sextets with different magnitudes of splitting, resulting in a broadening of lines. The mean width of sextet lines (0.50 mm/s) is larger than the typical values (for example, it is equal to 0.21 mm/s for metallic iron. The most likely reason for such a broadening of lines for Cu(2) sites is the spread of local fields due to nonuniform distribution of oxygen vacancies in CuO_x chains. Hence it is appropriate to associate the decrease in the line width under illumination to redistribution of oxygen in chains, which decreases the number of nonequivalent positions.

A nearly linear dependence of hyperfine field on the radiation flux density (see inset to Fig. 2) indicates the presence of a large number of free electron traps, which leads to linear dependence of hole concentration on the number of photons incident per unit time. This dependence must become sublinear upon an increase in illumination, when the hole concentration exceeds considerably the number of traps.[15]

It can be seen from Fig. 2 that the decrease in hyperfine field caused by illumination in the temperature interval 100–300 K is constant to within experimental error. Consequently, the relative variation ($\Delta H_n/H_n$) in the field at the nucleus induced by irradiation decreases with temperature. Hence it can be concluded that the thermally activated process of liberation of localized electrons slows down upon a decrease in temperature. On the other hand, the field at the nucleus at 100 K is restored to its initial value in about an hour (characteristic storage time for the Mössbauer spectrum) after the termination of irradiation. According to our earlier results on a considerable departure of the temperature dependence of the spectral area from the Debye–Waller curve below 100 K,[6] the energy of coupling of an electron to a trap can be assumed to be of the order of 100 K.

Thus, we conclude that the photoinduced variation of hole concentration is a reversible phenomenon. Hence if persistent photoconductivity exists in samples of a given composition, it is apparently due to an increase in the mean free path of carriers caused by an ordering of oxygen in the chains.

Hence the Mössbauer studies of the effect of photoirradiation on HTSC samples show that the effective hyperfine interaction field at Cu(2) sites decreases in proportion to illumination, which is associated with a decrease in exchange interaction caused by an increase in the hole concentration. The effect is reversible in the temperature interval 100–300 K, and the hole concentration is restored within an hour after the termination of illumination. The width of the Mössbauer spectral lines decreases as a result of irradiation due to an ordering of oxygen vacancies and an elongation of CuO_x chains. Apparently, the ordering of oxygen distribution leads to an increase in the mean free path of the carriers and may be responsible for persistent photoconductivity.

*E-mail: lukashov@ilt.kharkov.ua

[1] G. Yu and A. J. Heeger, Int. J. Mod. Phys. B **7**, 3751 (1993).
[2] P. Boolchand and D. McDaniel, Hyperfine Interact. **72**, 125 (1992).
[3] I. Felner and I. Nowic, Supercond. Sci. Technol. **8**, 121 (1995).
[4] I. S. Lyubutin, T. V. Dmitrieva, and V. G. Terziev, Zh. Éksp. Teor. Fiz. **102**, 1615 (1992) [Sov. Phys. JETP **75**, 873 (1992)].
[5] S. Nasu, H. Kitagawa, M. Yoshida *et al.*, Hyperfine Interact. **55**, 1355 (1990).
[6] V. V. Eremenko, D. V. Lukashev, K. M. Matsievskiĭ, and V. L. Ponomarchuk, Fiz. Nizk. Temp. **22**, 1383 (1996) [Low Temp. Phys. **22**, 1048 (1996)].
[7] G. Wertheim, *Mössbauer Effect Principles and Applications*, New York (1964).
[8] W. Kundig, Nucl. Instrum. Methods **48**, 219 (1967).
[9] V. I. Kudinov, A. I. Kirilyuk, N. M. Kreines *et al.*, Phys. Lett. A **151**, 358 (1990).
[10] G. Yu, H. Lee, A. J. Heeger *et al.*, Phys. Rev. B **45**, 4964 (1992).
[11] E. Osquiguil, M. Maenhoudt, B. Wuyts *et al.*, Phys. Rev. B **49**, 3675 (1994).
[12] D. Lederman, J. Hasen, I. K. Shuller *et al.*, Appl. Phys. Lett. **64**, 652 (1994).
[13] V. V. Eremenko, I. S. Kachur, V. G. Piryatinskaya *et al.*, Physica C **262**, 54 (1996).
[14] T. A. Tyson, J. F. Federici, D. Chew *et al.*, Physica C **292**, 163 (1997).
[15] C. Kittel, *Introduction to Solid State Physics* [Russian transl.], Nauka, Moscow (1978).

Translated by R. S. Wadhwa

LETTERS TO THE EDITOR

On the mechanism of critical temperature enhancement in cuprate high-T_c superconductors under pressure

E. A. Pashitskiĭ

*Institute of Physics, National Academy of Sciences of the Ukraine, 252650 Kiev, Ukraine**
(Submitted August 10, 1998)
Fiz. Nizk. Temp. **24**, 1211–1214 (December 1998)

The results of experiments [C. Y. Han *et al.*, Low Temp. Phys. **24**, 305 (1998)] on the influence of quasi-hydrostatic pressure P on the superconducting transition temperature T_c in polycrystalline samples of cuprate compounds $Tl_2Ba_2Ca_2Cu_3O_x$ (Tl-2223) with the initial value of $T_c=129$ K and the maximum value $T_c=255.4$ K at $P=4.3$ GPa are considered. A hypothesis on the existence of two mechanisms of the effect of pressure on T_c is proposed on the basis of an analysis of the nonmonotonic dependence of T_c on P. The first mechanism operating in the pressure range $P<3$ GPa is connected with the anisotropic deformation of the crystal lattice of individual grains (crystallites) in the plane of cuprate layers CuO_2 and with a change in the oxygen doping of layers. The second mechanism operating in the pressure range $P>3$ GPa is due to hydrostatic compression of the ionic lattice and an increase in the bulk concentration of charge carriers (holes) in view of the electroneutrality condition.
© *1998 American Institute of Physics.* [S1063-777X(98)01212-2]

1. Han *et al.*[1] reported recently on a nearly two-fold increase in the superconducting transition temperature in a high-T_c superconductor (HTSC) $Tl_{1.8}Ba_2Ca_{2.6}Cu_3O_{10+\delta}$ (Tl-2223) under pressure from the initial value $T_c=129$ K under zero applied pressure ($P=0$) to $T_c^{\max}=255.4$ K at $P=4.3$ GPa ($\approx$400 kbar). This sensational result naturally requires an additional independent verification and confirmation (or denial) in other laboratories. It is reasonable, however, to carry out a preliminary analysis of the experimental data obtained in Ref. 1 and to compare them with the available numerous results on the dependence of T_c on P for various cuprate metaloxide compounds (MOC).

It is well known that the dependence of T_c on hydrostatic (isotropic) pressure for cuprate MOC such as $La_{2-x}(Ba, Sr)_xCuO_4$, $YBa_2Cu_3O_{6+x}$, $Bi_2Sr_2Ca_{n-1}Cu_nO_x$, is very weak,[2–5] while for the ceramics $HgBa_2Ca_{n-1}Cu_nO_x$ with the maximum value of $T_c=135$ K (for $n=3$), the derivative $dT_c/dP=1$ K/GPa. As a result, it has become possible to attain for Hg-1223 the values of $T_c\approx(150-155)$ K in the pressure range $P\approx(5-10)$ GPa,[6,7] and later the record-high value of $T_c=164$ K at $P=31$ GPa.[8]

The pressure dependence of T_c in Tl–Ba–Ca–Cu–O compounds was also investigated intensely,[9–12] but the value of T_c for Tl-2223 could be elevated only by 5 K from $T_c=128$ K to $T_c=133$ K at $P=13$ GPa. Nevertheless, an anomalously high value of the derivative $dT_c/dP\approx2.5$ K/GPa was observed for polycrystalline samples of Tl-2223 in the pressure range $P\lesssim2$ GPa.[9,10]

At the same time, experiments on anisotropic uniaxial compression (or extension) of single crystals of $YBa_2Cu_3O_{7-\delta}$[4] and $Bi_2Sr_2CaCu_2O_x$[5] demonstrated anomalously strong anisotropy in the dependence of T_c on P_i in the direction of different crystallographic axes. For example, the derivatives $\partial T_c/\partial P_i$ for an optimally doped layer-chain single crystal of $YBa_2Cu_3O_{7-\delta}$ (Y-123) along different axes have different signs: $\partial T/_c/\partial P_a=-(1.9-2.0)$ K/GPa, $\partial T_c/\partial P_b=+(1.9-2.2)$ K/GPa, and $\partial T_c/\partial P_c/\partial P_c=-(0.1-0.3)$ K/GPa. Anisotropy in the plane ab of the layers is associated with the presence of ordered $1D$ CuO chains along the b-axis, which serve as an oxygen reservoir for doping $2D$ cuprate layers of CuO_2 with free holes.[4]

On the other hand, according to experimental data,[5] $\partial T_c/\partial P_a\approx1.6$ K/GPa, $\partial T_c/\partial P_b\approx2.0$ K/GPa, and $\partial T_c/\partial P_c\approx-2.8$ K/GPa. for layered crystals $Bi_2Sr_2CaCu_2O_{8+\delta}$ (Bi-2212). This is due to nearly isotropic properties of these crystals in the ab plane of the layers and a change in the conditions of doping of cuprate layers CuO_2 with holes from the side of intermediate oxide layers BiO and SrO under pressure. The same type of anisotropy is apparently observed for $\partial T_c/\partial P_i$ of layered crystals Tl–Ba–Ca–Cu–O and Hg–Ba–Ca–Cu–O. The application of an isotropic hydrostatic pressure must lead to almost complete compensation of the effect $dT_c/dP=\Sigma_i\partial T_c/\partial P_i\approx0$, for single crystals of these cuprate MOC.

However, polycrystalline samples (pressed powders and ceramics) with arbitrarily oriented crystallographic axes in different grains (granules) can exhibit anisotropic properties in individual crystallites (i.e., contributions of different components of $\partial T_c/\partial P_i$) under certain conditions of compression and stacking even under the action of quasi-hydrostatic pressure. This follows from a quite large value of dT_c/dP in

 © 1998 American Institute of Physics

$HgBa_2Ca_2Cu_3O_x$ ceramics up to $P=31$ GPa[8] and in $Tl_2Ba_2Ca_2Cu_3O_x$ up to $P=2$ GPa.[9]

2. The dependence of T_c on P presented by Han *et al.*[1] indicates the existence of *two different mechanisms of increase in T_c under pressure*. The first mechanism leads to a monotonic increase in T_c from $T_{c0}=129$ K at $P=0$ to $T_c\approx 175$ K at $P=3$ GPa, the increase in T_c in the pressure range $1.6\ \text{GPa}\leqslant P\leqslant 3$ GPa being nonlinear. The second mechanism comes into play under high pressures $P>3$ GPa and leads to a nonmonotonic (bell-shaped) dependence of T_c on P with a peak $T_c^{\max}\approx 255$ K at $P\approx 4$ GPa (taking into account the spread of experimental points).

Since the slope $dT_c/dP=1.7$ K/GPa for low P virtually coincides[1] with the derivatives $\partial T_c/\partial P_a$ and $\partial T_c/\partial P_b$ in the plane of the layers of a Bi(2212) crystal,[5] we can assume that the *linear increase in T_c* for $P\leqslant 1.6$ GPa *occurs due to elastic deformation by compression in the ab planes* of the grains (crystallites) oriented in a definite way relative to the direction of the maximum value $P_{\max}$ of incompletely isotropic (quasi-hydrostatic) external pressure. The finite residual resistance below T_c can be due to the fact that optimally oriented crystallites are separated by fragments with a nonoptimal orientation of crystallites with lower values of T_c or with normal metal-type conductivity.

Nonlinearity in the pressure dependence of T_c in the region $1.6\ \text{GPa}<P<3$ GPa *can be due to lattice anharmonism* in crystallites compressed to the maximum possible extent. Thus, the $T_c(P)$ dependence at $P<3$ GPa can be presented in the form

$$T_c(P)=T_c(0)+\frac{dT_c}{dP}P+\frac{1}{2}\frac{d^2T_c}{dP^2}P^2. \tag{1}$$

The corresponding dependence of T_c on elastic strain (dilatation) $\varepsilon=\varepsilon_{xx}+\varepsilon_{yy}$ of the lattice (where ε_{xx} and ε_{yy} are the strain tensor components in the xy plane of the layers) for $\varepsilon\propto P$ has the form

$$T_c(\varepsilon)=T_c(0)+C\varepsilon+q(C\varepsilon)^2, \tag{2}$$

where the coefficient C is close to the absolute values of $C_a=-\partial T_c/\partial\varepsilon_{xx}$ and $C_b=-\partial T_c/\partial\varepsilon_{yy}$ in a Y-123 crystal or to $C_a\approx C_b\approx 300$ K in a Bi-2212 crystal, where $dT_c/dP\approx 1.7$ K/GPa and $C\varepsilon=(dT_c/dP)P\approx 5$ K at $P=3$ GPa. The value of the coefficient q in (2) corresponding to the value of $T_c\approx 178$ K at $P=3$ GPa and matching to the results of experiments,[1] is equal to 1.7, and the maximum strain is small ($\varepsilon=0.016$), which corresponds to the applicability condition for the theory of elasticity.[14]

In the pressure range $P>3$ GPa, *the deformation mechanism of increasing T_c attains saturation* at $T_c\approx(175-180)$ K *due to complete isotropization of external pressure* (for extremely close packing of grains of the cuprate Tl–Ba–Ca–Cu–O and the working substance) and due to almost complete compensation of anisotropic positive and negative contributions from $\partial T_c/\partial P_i$ along different crystallographic axes to the average (total) derivative dT_c/dP. (A similar saturation of T_c at $P>2$ GPa was observed by Lin *et al.*[9] at the level $T_c=133$ K.)

3. *The bell-shaped dependence $T_c(P)$ in the pressure range (3–5) GPa*[1] *is similar to the concentration dependence of T_c in cuprate MOC of the hole type*, which can be approximated by a parabolic function of the number of holes x_h per copper atom, which is universal for all MOC:[15,16]

$$T_c(x_h)=T_{cm}[1-A(x_h-x_m)^2], \tag{3}$$

where $x_m=0.16$, and the coefficient A is chosen from the condition of vanishing of $T_c(x_h)$ for $x_h=0.05$ and $x_h=0.27$, i.e., $A\approx 82.6$.

It was proposed earlier[17] that *the concentration of free charge carriers* (including doped holes) in the ionic crystal lattice of cuprate MOC *is redistributed by virtue of the electroneutrality condition in fields of elastic deformation* with a nonuniform dilatation $\varepsilon(\mathbf{r})$ near macroscopic defects. Spatial inhomogeneity of the hole concentration $n_h(\mathbf{r})=n_0[1-\varepsilon(\mathbf{r})]$ leads, in accordance with (3), to inhomogeneity of the local critical temperature $T_c(\mathbf{r})$ if the characteristic size of defects (dislocation walls and piles, noncoherent grain boundaries, microcracks, etc.) is much larger than the screening length l_D and the coherence length $\xi_0(l_D\approx\xi_0\approx 15-20\ \text{Å})$. In this case, the dependence of T_c on the strain tensor ε_{ik} in an anisotropic crystal is also quadratic and can be presented in the isotropic approximation in the form[17]

$$T_c(\varepsilon)=T_{c0}+C\varepsilon-(C\varepsilon)^2/4\Delta T_m, \tag{4}$$

where $\Delta T_m=\tilde{T}_{cm}-T_{c0}$, and the maximum value of $\tilde{T}_{cm}$ is attained for the dilatation $\varepsilon_m=2\Delta T_m/C$.

In Ref. 17, we assumed that T_{c0} corresponds to the value of T_c in an undeformed crystal, and T_{c0} and the parameter C (see Ref. 18) noticeably depend on the doping level, and the value of $\tilde{T}_{cm}$ does not necessarily coincide with the value of T_{cm} in formula (3) for T_c at $\varepsilon=0$ in the general case, being an unknown free parameter for each type of cuprate MOC. We used for the parameter C the empirical values C_i in the low pressure limit $(P\to 0)$, which correspond to the deformation mechanism of the effect of anisotropic P_i on T_c considered above.[13]

We assume that a quadratic dependence of T_c on ε and P similar to formula (4) is also valid under higher pressures (but within the limits of elastic deformation $\varepsilon\propto P$) *in the case of hydrostatic compression*, when *the average bulk concentration of charge carriers (holes) increases by virtue of the electroneutrality condition*. Taking into account the parabolic concentration dependence (3), which can be due to the nonmonotonic dependence of T_c on the position of the Fermi level relative to extended saddle-type singularities with a giant Van Hove (root) singularity in the density of states on the one hand,[19,20] and on the other hand, due to effects of strong coupling leading to renormalization of the electron-electron interaction constant,[21,22] we present the dependence of T_c on P in the region of $P=(3-5)$ GPa in the form

$$T_c(P)=\tilde{T}_{c0}+(\tilde{T}_{cm}-\tilde{T}_{c0})[1-B(P-P_m)^2], \tag{5}$$

where $P_m=4$ GPa, $\tilde{T}_{cm}=255$ K, and $\tilde{T}_{c0}$ is the value of $T_c(P)$ at $P=3$ GPa and $P=5$ GPa, which is equal to 178 K, i.e., the coefficient $B=1\ \text{GPa}^{-1}$. Figure 1 shows the combined dependence of T_c on P composed from (1) or (2) for

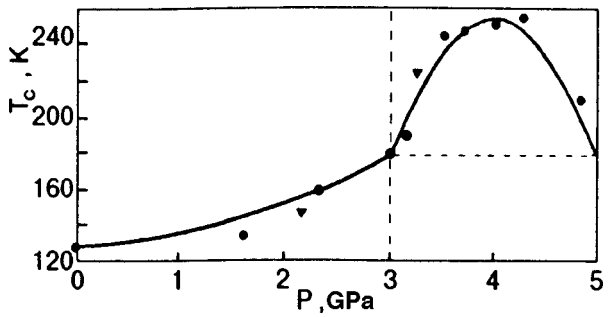

FIG. 1. Semi-empirical combined dependence of T_c on P corresponding to the anisotropic deformation mechanism (taking into account lattice anharmonism) described by formulas (1) and (2) in the pressure range $P<3$ GPa and the hydrostatic compression mechanism (following the saturation of the first mechanism) described by formula (5) for $P>3$ GPa. Dark circles and triangles correspond to experimental results obtained in Ref. 1.

$P<3$ GPa and (5) for $P>3$ GPa. This curve provides a qualitatively correct description of the experimental dependence $T_c(P)$ obtained in Ref. 1 and requiring additional verification.

4. Thus, according to the theoretical concept proposed by us here, the anomalously high maximum value of $T_c \approx 255$ K observed by Han *et al.*[1] in Tl-2223 under pressure can be the result of joint action of two different mechanisms of increasing T_c in cuprate MOC of the hole type: *anisotropic deformation mechanism* in the pressure range $P<3$ GPa, which is associated with a change in the nature of doping of cuprate layers upon an increase in P, and *universal pressure mechanism of bulk compression* of the crystal, in which the bulk concentration of holes and the nonmonotonic variation of T_c associated with it increase according to the parabolic law (3). The latter is confirmed not only by a quasi-parabolic dependence of T_c on P in the range of $P=(3-5)$ GPa, but also by the absolute increase in T_c in this region, which is equal to $\tilde{T}_{cm}-\tilde{T}_{c0}\approx 77$ K and is typical of HTSC materials under doping. It should be noted in conclusion that in all previous measurements of the dependence $T_c(P)$, the experimenters apparently ''missed'' a comparatively narrow interval of intermediate pressures (3–5) GPa. For this reason, new ''surprises'' can be expected in this pressure range for other types of HTSC materials (including the compound $HgBa_2Ca_2Cu_3O_x$ characterized by the highest superconducting transition temperature).

*E-mail: pashitsk@iop.kiev.ua

[1] C. Y. Han, W. Lin, Y. S. Wu *et al.*, Fiz. Nizk. Temp. **24**, 305 (1998) [Low Temp. Phys. **24**, 230 (1998)].
[2] M. Barden, O. Hoffels, W. Schnelle *et al.*, Phys. Rev. B **47**, 12 288 (1993).
[3] F. Gugenberger, C. Meingast, G. Roth *et al.*, Phys. Rev. B **49**, 13 137 (1994).
[4] U. Welp, M. Grimsditch, S. Fleshler *et al.*, J. Supercond. **7**, 159 (1994).
[5] C. Meingast, A. Junod, and E. Walker, Physica C **272**, 106 (1996).
[6] C. W. Chu, L. Gao, F. Chen *et al.*, Nature (London) **365**, 323 (1993).
[7] M. Nunez-Requiro, J.-L. Thelence, E. V. Antipov *et al.*, Science **262**, 97 (1993).
[8] L. Gao, Y. Y. Xue, F. Chen *et al.*, Phys. Rev. B **50**, 4260 (1994).
[9] J. G. Lin, K. Matsuishi, Y. Q. Wang *et al.*, Physica C **175**, 627 (1991).
[10] D. Tristan, R. J. Wijngaarden, R. S. Liu *et al.*, Physica C **218**, 24 (1993).
[11] D. T. Jover, R. J. Wijngaarden, R. Griessen *et al.*, Phys. Rev. B **54**, 10 175 (1996).
[12] D. T. Jover, R. J. Wijngaarden, H. Wilhelm *et al.*, Phys. Rev. B **54**, 4265 (1996).
[13] C. Meingast, O. Kraut, T. Wolf *et al.*, Phys. Rev. Lett. **67**, 1634 (1991).
[14] L. D. Landau and E. M. Lifshitz, *The Theory of Elasticity* [in Russian], Nauka, Moscow (1987).
[15] M. H. Whangbo and C. C. Torardi, Science **249**, 1143 (1990).
[16] R. P. Gupta and M. Gupta, Phys. Rev. B **51**, 11 760 (1995).
[17] A. Gurevich and E. A. Pashitskiĭ, Phys. Rev. B **56**, 6213 (1997).
[18] C. C. Almasan, S. H. Han, B. W. Lee *et al.*, Phys. Rev. Lett. **69**, 680 (1992).
[19] A. A. Abrikosov, J. C. Campuzano, and K. Gofron, Physica C **214**, 73 (1993).
[20] K. Gofron, J. C. Campuzano, A. A. Abrikosov *et al.*, Phys. Rev. Lett. **73**, 3302 (1994).
[21] G. M. Eliashberg, Sov. Phys. JETP **38**, 966 (1960); **39**, 1437 (1960) [Sov. Phys. JETP **11**, 696 (1960); **12**, 1000 (1960)].
[22] E. A. Pashitskiĭ, V. I. Pentegov, and E. Abragam, JETP Lett. **67**, 495 (1998).

Translated by R. S. Wadhwa